Hard interactions of quarks and gluons: a primer for LHC physics

J M Campbell[1]**, J W Huston**[2] **and W J Stirling**[3]

[1] Department of Physics and Astronomy, University of Glasgow, Glasgow G12 8QQ, UK
[2] Department of Physics and Astronomy, Michigan State University, East Lansing,
MI 48840, USA
[3] Institute for Particle Physics Phenomenology, University of Durham,
Durham DH1 3LE, UK

E-mail: j.campbell@physics.gla.ac.uk, huston@msu.edu and w.j.stirling@durham.ac.uk

Abstract

In this paper, we will develop the perturbative framework for the calculation of hard-scattering processes. We will undertake to provide both a reasonably rigorous development of the formalism of hard-scattering of quarks and gluons as well as an intuitive understanding of the physics behind the scattering. We will emphasize the role of logarithmic corrections as well as power counting in α_S in order to understand the behaviour of hard-scattering processes. We will include 'rules of thumb' as well as 'official recommendations', and where possible will seek to dispel some myths. We will also discuss the impact of soft processes on the measurements of hard-scattering processes. Experiences that have been gained at the Fermilab Tevatron will be recounted and, where appropriate, extrapolated to the LHC.

(Some figures in this article are in colour only in the electronic version)

Contents

1. Introduction

Scattering processes at high-energy hadron colliders can be classified as either hard or soft. Quantum Chromodynamics (QCD) is the underlying theory for all such processes, but the approach and level of understanding is very different for the two cases. For hard processes, e.g. Higgs boson or high p_T jet production, the rates and event properties can be predicted with good precision using perturbation theory. For soft processes, e.g. the total cross section, the underlying event etc, the rates and properties are dominated by non-perturbative QCD effects, which are less well understood. For many hard processes, soft interactions occur along with the hard interactions and their effects must be understood for comparisons to be made to perturbative predictions. An understanding of the rates and characteristics of predictions for hard processes, both signals and backgrounds, using perturbative QCD (pQCD) is crucial for both the Tevatron and LHC.

In this paper, we will develop the perturbative framework for the calculation of hard-scattering processes. We will undertake to provide both a reasonably rigorous development of the formalism of hard-scattering of quarks and gluons as well as an intuitive understanding of the physics behind the scattering. We will emphasize the role of logarithmic corrections as well as power counting in α_S in order to understand the behaviour of hard-scattering processes. We will include 'rules of thumb' as well as 'official recommendations', and where possible will seek to dispel some myths. We will also discuss the impact of soft processes on the measurements of hard-scattering processes. Given the limitations of space, we will concentrate on a few processes, mostly inclusive jet, W/Z production and W/Z+jets, but the lessons should be useful for other processes at the Tevatron and LHC as well. As a bonus feature, this paper is accompanied by a 'benchmark website'[4], where updates and more detailed discussions than are possible in this limited space will be available. We will refer to this website on several occasions in the course of this paper.

In section 2, we introduce the hard-scattering formalism and the QCD factorization theorem. In section 3, we apply this formalism to some basic processes at leading order, next-to-leading order and next-to-next-to-leading order. Section 4 provides a detailed discussion of parton distribution functions (pdfs) and global pdf fits and in section 5 we compare the predictions of pQCD with the measurements at the Tevatron. Lastly, in section 6, we provide some benchmarks and predictions for measurements to be performed at the LHC.

2. Hard-scattering formalism and the QCD factorization theorem

2.1. Introduction

In this section, we will discuss in more detail on how the QCD factorization theorem can be used to calculate a wide variety of hard-scattering cross sections in hadron–hadron collisions. For simplicity we will restrict our attention to leading-order processes and calculations; the extension of the formalism to more complicated processes and to include higher-order perturbative contributions will be discussed in sections 3 and 6.

We begin with a brief review of the factorization theorem. It was first pointed out by Drell and Yan [1] more than 30 years ago that parton-model ideas developed for deep-inelastic scattering could be extended to certain processes in hadron–hadron collisions. The paradigm process was the production of a massive lepton pair by quark–antiquark annihilation—the Drell–Yan process—and it was postulated that the hadronic cross section $\sigma(AB \to \mu^+\mu^- + X)$
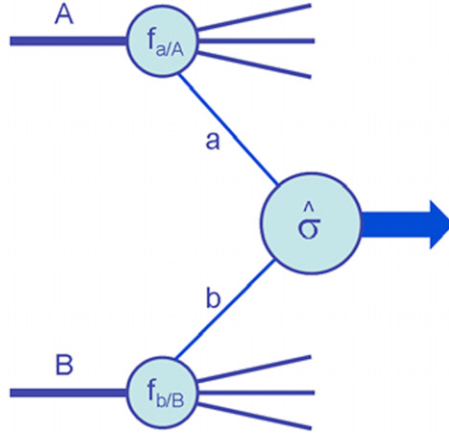
Figure 1. Diagrammatic structure of a generic hard-scattering process.

could be obtained by weighting the subprocess cross section $\hat{\sigma}$ for $q\bar{q} \to \mu^+\mu^-$ with the parton distribution functions (pdfs) $f_{q/A}(x)$ extracted from deep-inelastic scattering:

$$\sigma_{AB} = \int dx_a dx_b \; f_{a/A}(x_a) f_{b/B}(x_b) \; \hat{\sigma}_{ab \to X} \;, \tag{1}$$

where for the Drell–Yan process, $X = l^+l^-$ and $ab = q\bar{q}, \; \bar{q}q$. The domain of validity is the asymptotic 'scaling' limit (the analogue of the Bjorken scaling limit in deep-inelastic scattering) $M_X \equiv M_{l^+l^-}^2, s \to \infty, \tau = M_{l^+l^-}^2/s$ fixed. The good agreement between theoretical predictions and the measured cross sections provided confirmation of the parton-model formalism, and allowed for the first time a rigorous, quantitative treatment of certain hadronic cross sections. Studies were extended to other 'hard-scattering' processes, for example the production of hadrons and photons with large transverse momentum, with equally successful results. Problems, however, appeared to arise when perturbative corrections from real and virtual gluon emission were calculated. Large logarithms from gluons emitted collinear with the incoming quarks appeared to spoil the convergence of the perturbative expansion. It was subsequently realized that these logarithms were the same as those that arise in deep-inelastic scattering structure function calculations, and could therefore be absorbed, via the DGLAP equations, in the definition of the parton distributions, giving rise to logarithmic violations of scaling. The key point was that *all* logarithms appearing in the Drell–Yan corrections could be factored into renormalized parton distributions in this way, and *factorization theorems* which showed that this was a general feature of hard-scattering processes were derived [2]. Taking into account the leading logarithm corrections, (1) simply becomes

$$\sigma_{AB} = \int dx_a dx_b \; f_{a/A}(x_a, Q^2) f_{b/B}(x_b, Q^2) \; \hat{\sigma}_{ab \to X}, \tag{2}$$

corresponding to the structure depicted in figure 1. The Q^2 that appears in the parton distribution functions (pdfs) is a large momentum scale that characterizes the hard-scattering, e.g. $M_{l^+l^-}^2, p_T^2, \ldots$. Changes to the Q^2 scale of $\mathcal{O}(1)$, e.g. $Q^2 = 2M_{l^+l^-}^2, \; M_{l^+l^-}^2/2$ are equivalent in this leading logarithm approximation.

The final step in the theoretical development was the recognition that the *finite* corrections left behind after the logarithms had been factored were not universal and had to be calculated separately for each process, giving rise to perturbative $\mathcal{O}(\alpha_s^n)$ corrections to the leading

logarithm cross section of (2). Schematically

$$\sigma_{AB} = \int dx_a dx_b \, f_{a/A}(x_a, \mu_F^2) \, f_{b/B}(x_b, \mu_F^2) \, \times \, [\, \hat{\sigma}_0 \, + \, \alpha_S(\mu_R^2) \, \hat{\sigma}_1 \, + \, \cdots]_{ab \to X}. \tag{3}$$

Here μ_F is the *factorization scale*, which can be thought of as the scale that separates the long- and short-distance physics, and μ_R is the *renormalization scale* for the QCD running coupling. Formally, the cross section calculated to all orders in perturbation theory is invariant under changes in these parameters, the μ_F^2 and μ_R^2 dependence of the coefficients, e.g. $\hat{\sigma}_1$, exactly compensating the explicit scale dependence of the parton distributions and the coupling constant. This compensation becomes more exact as more terms are included in the perturbation series, as will be discussed in more detail in section 3.3.2. In the absence of a complete set of higher-order corrections, it is necessary to make a specific choice for the two scales in order to make cross section predictions. Different choices will yield different (numerical) results, a reflection of the uncertainty in the prediction due to unknown higher order corrections, see section 3. To avoid unnaturally large logarithms reappearing in the perturbation series it is sensible to choose μ_F and μ_R values of the order of the typical momentum scales of the hard-scattering process, and $\mu_F = \mu_R$ is also often assumed. For the Drell–Yan process, for example, the standard choice is $\mu_F = \mu_R = M$, the mass of the lepton pair.

The recipe for using the above leading-order formalism to calculate a cross section for a given (inclusive) final-state X+anything is very simple: (i) identify the leading-order partonic process that contributes to X, (ii) calculate the corresponding $\hat{\sigma}_0$, (iii) combine with an appropriate combination (or combinations) of pdfs for the initial-state partons a and b, (iv) make a specific choice for the scales μ_F and μ_R and (v) perform a numerical integration over the variables x_a, x_b and any other phase-space variables associated with the final-state X. Some simple examples are

Z-production	$q\bar{q} \to Z$
top quark production	$q\bar{q} \to t\bar{t}, \; gg \to t\bar{t}$
large E_T jet production	$gg \to gg, \; qg \to qg, \; qq \to qq$ etc

where appropriate scale choices are M_Z, m_t, E_T, respectively [3–7]. Expressions for the corresponding subprocess cross sections $\hat{\sigma}_0$ are widely available in the literature, see for example [8].

The parton distributions used in these hard-scattering calculations are solutions of the DGLAP equations [9][5]

$$\frac{\partial q_i(x, \mu^2)}{\partial \log \mu^2} = \frac{\alpha_S}{2\pi} \int_x^1 \frac{dz}{z} \left\{ P_{q_i q_j}(z, \alpha_S) q_j\left(\frac{x}{z}, \mu^2\right) + P_{q_i g}(z, \alpha_S) \, g\left(\frac{x}{z}, \mu^2\right) \right\},$$

$$\frac{\partial g(x, \mu^2)}{\partial \log \mu^2} = \frac{\alpha_S}{2\pi} \int_x^1 \frac{dz}{z} \left\{ P_{g q_j}(z, \alpha_S) q_j\left(\frac{x}{z}, \mu^2\right) + P_{gg}(z, \alpha_S) g\left(\frac{x}{z}, \mu^2\right) \right\}, \tag{4}$$

where the splitting functions have perturbative expansions:

$$P_{ab}(x, \alpha_S) = P_{ab}^{(0)}(x) + \frac{\alpha_S}{2\pi} P_{ab}^{(1)}(x) + \cdots. \tag{5}$$

Expressions for the leading order (LO) and next-to-leading order (NLO) splitting functions can be found in [8]. The DGLAP equations determine the Q^2 dependence of the pdfs.

---

[5] The DGLAP equations effectively sum the leading powers of $[\alpha_S \log \mu^2]^n$ generated by multiple gluon emission in a region of phase space where the gluons are strongly ordered in transverse momentum. These are the dominant contributions when $\log(\mu) \gg \log(1/x)$.
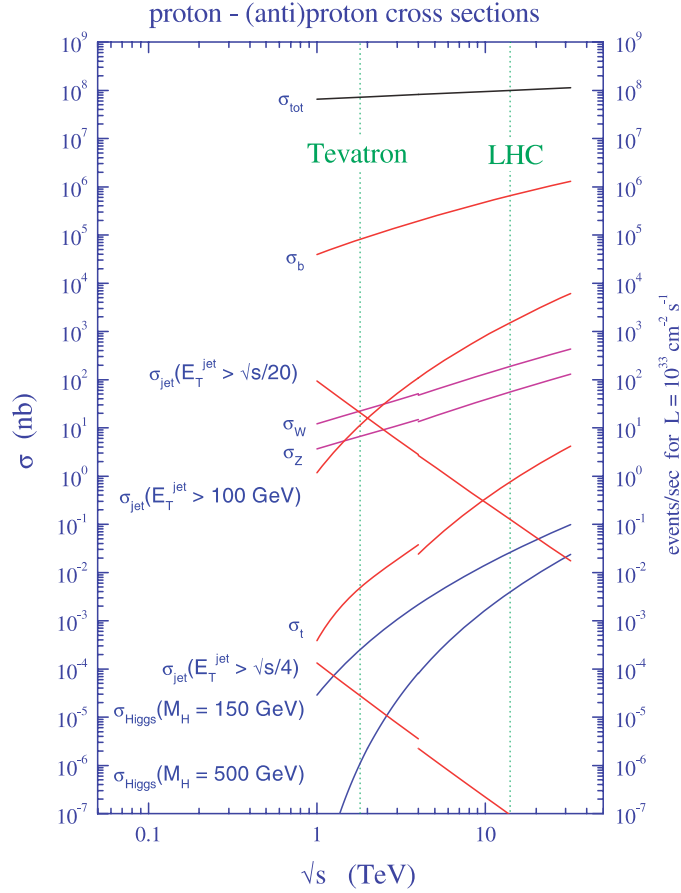
proton - (anti)proton cross sections

σ_{tot}

Tevatron LHC

σ_b

$\sigma_{jet}(E_T^{jet} > \sqrt{s}/20)$

σ_W
σ_Z

$\sigma_{jet}(E_T^{jet} > 100\ \text{GeV})$

σ_t

$\sigma_{jet}(E_T^{jet} > \sqrt{s}/4)$

$\sigma_{Higgs}(M_H = 150\ \text{GeV})$

$\sigma_{Higgs}(M_H = 500\ \text{GeV})$

σ (nb)

events/sec for L = 10^{33} cm^{-2} s^{-1}

$\sqrt{s}$ (TeV)

Figure 2. Standard model cross sections at the Tevatron and LHC colliders.

The x dependence, on the other hand, has to be obtained from fitting deep-inelastic and other hard-scattering data. This will be discussed in more detail in section 4. Note that for consistency, the order of the expansion of the splitting functions should be the same as that of the subprocess cross section, see (3). Thus, for example, a full NLO calculation will include both the $\hat{\sigma}_1$ term in (3) and the $P_{ab}^{(1)}$ terms in the determination of the pdfs via (4) and (5).

Figure 2 shows the predictions for some important Standard Model cross sections at $p\bar{p}$ and pp colliders, calculated using the above formalism (at next-to-leading order in perturbation theory, i.e. including also the $\hat{\sigma}_1$ term in (3)).

We have already mentioned that the Drell–Yan process is the paradigm hadron–collider hard-scattering process, and so we will discuss this in some detail in what follows. Many of the remarks apply also to other processes, in particular those shown in figure 2, although of course the higher-order corrections and the initial-state parton combinations are process dependent.

2.2. The Drell–Yan process

The Drell–Yan process is the production of a lepton pair (e^+e^- or $\mu^+\mu^-$ in practice) of large invariant mass M in hadron–hadron collisions by the mechanism of quark–antiquark

annihilation [1]. In the basic Drell–Yan mechanism, a quark and antiquark annihilate to produce a virtual photon, $q\bar{q} \to \gamma^* \to l^+l^-$. At high-energy colliders, such as the Tevatron and LHC, there is of course sufficient centre-of-mass energy for the production of on-shell W and Z bosons as well. The cross section for quark–antiquark annihilation to a lepton pair via an intermediate massive photon is easily obtained from the fundamental QED $e^+e^- \to \mu^+\mu^-$ cross section, with the addition of the appropriate colour and charge factors.

$$\hat{\sigma}(q\bar{q} \to e^+e^-) = \frac{4\pi\alpha^2}{3\hat{s}} \frac{1}{N} Q_q^2, \tag{6}$$

where Q_q is the quark charge: $Q_u = +2/3$, $Q_d = -1/3$, etc. The overall colour factor of $1/N = 1/3$ is due to the fact that only when the colour of the quark matches with the colour of the antiquark can annihilation into a colour-singlet final state take place.

In general, the incoming quark and antiquark will have a spectrum of centre-of-mass energies $\sqrt{\hat{s}}$, and so it is more appropriate to consider the differential mass distribution:

$$\frac{d\hat{\sigma}}{dM^2} = \frac{\hat{\sigma}_0}{N} Q_q^2 \delta(\hat{s} - M^2), \qquad \hat{\sigma}_0 = \frac{4\pi\alpha^2}{3M^2}, \tag{7}$$

where M is the mass of the lepton pair. In the centre-of-mass frame of the two hadrons, the components of momenta of the incoming partons may be written as

$$p_1^\mu = \frac{\sqrt{s}}{2}(x_1, 0, 0, x_1),$$

$$p_2^\mu = \frac{\sqrt{s}}{2}(x_2, 0, 0, -x_2). \tag{8}$$

The square of the parton centre-of-mass energy $\hat{s}$ is related to the corresponding hadronic quantity by $\hat{s} = x_1 x_2 s$. Folding in the pdfs for the initial-state quarks and antiquarks in the colliding beams gives the hadronic cross section:

$$\frac{d\sigma}{dM^2} = \frac{\hat{\sigma}_0}{N} \int_0^1 dx_1 dx_2 \delta(x_1 x_2 s - M^2)$$

$$\times \left[\sum_k Q_k^2 \left(q_k(x_1, M^2)\bar{q}_k(x_2, M^2) + [1 \leftrightarrow 2] \right) \right]. \tag{9}$$

From (8), the rapidity of the produced lepton pair is found to be $y = 1/2 \log(x_1/x_2)$, and hence

$$x_1 = \frac{M}{\sqrt{s}} e^y, \qquad x_2 = \frac{M}{\sqrt{s}} e^{-y}. \tag{10}$$

The double-differential cross section is therefore

$$\frac{d\sigma}{dM^2 dy} = \frac{\hat{\sigma}_0}{Ns} \left[\sum_k Q_k^2 \left(q_k(x_1, M^2)\bar{q}_k(x_2, M^2) + [1 \leftrightarrow 2] \right) \right] \tag{11}$$

with x_1 and x_2 given by (10). Thus different values of M and y probe different values of the parton x of the colliding beams. The formulae relating x_1 and x_2 to M and y of course also apply to the production of *any* final state with this mass and rapidity. Assuming the factorization scale (Q) is equal to M, the mass of the final state, the relationship between the parton (x, Q^2) values and the kinematic variables M and y is illustrated pictorially in figure 3, for the LHC collision energy $\sqrt{s} = 14$ TeV. For a given rapidity y there are two (dashed) lines, corresponding to the values of x_1 and x_2. For $y = 0$, $x_1 = x_2 = M/\sqrt{s}$.
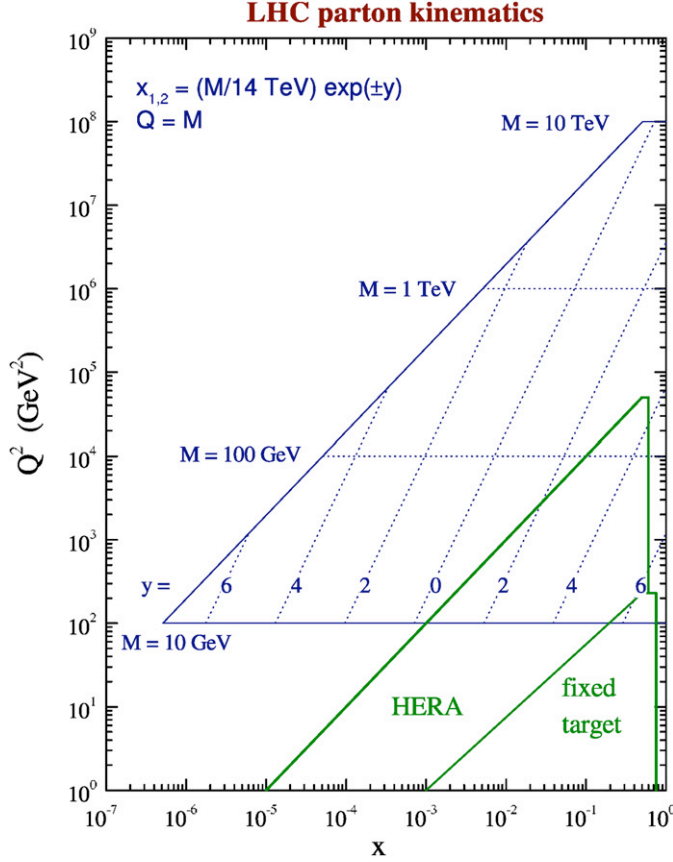
**Figure 3.** Graphical representation of the relationship between parton (x, Q^2) variables and the kinematic variables corresponding to a final state of mass M produced with rapidity y at the LHC collider with $\sqrt{s} = 14$ TeV.

In analogy with the Drell–Yan cross section derived above, the subprocess cross sections for (on-shell) W and Z production are readily calculated to be

$$\hat{\sigma}^{q\bar{q}' \to W} = \frac{\pi}{3} \sqrt{2} G_F M_W^2 |V_{qq'}|^2 \delta(\hat{s} - M_W^2),$$

$$\hat{\sigma}^{q\bar{q} \to Z} = \frac{\pi}{3} \sqrt{2} G_F M_Z^2 (v_q^2 + a_q^2) \delta(\hat{s} - M_Z^2), \tag{12}$$

where $V_{qq'}$ is the appropriate Cabibbo–Kobayashi–Maskawa matrix element, and v_q (a_q) is the vector (axial vector) coupling of the Z to the quarks. These formulae are valid in the *narrow width production* in which the decay width of the gauge boson is neglected. The resulting cross sections can then be multiplied by the branching ratio for any particular hadronic or leptonic final state of interest.

High-precision measurements of W and Z production cross sections from the Fermilab Tevatron $p\bar{p}$ collider are available and allow the above formalism to be tested quantitatively. Thus figure 4 shows the cross sections for $W^{\pm}$ and Z^0 production and decay into various leptonic final states from the CDF [12] and D0 [13] collaborations at the Tevatron. The theoretical predictions are calculated at LO (i.e. using (12)), NLO and NNLO (next-to-next-to-leading order) in perturbation theory using the $\overline{\text{MS}}$ scheme MRST parton distributions
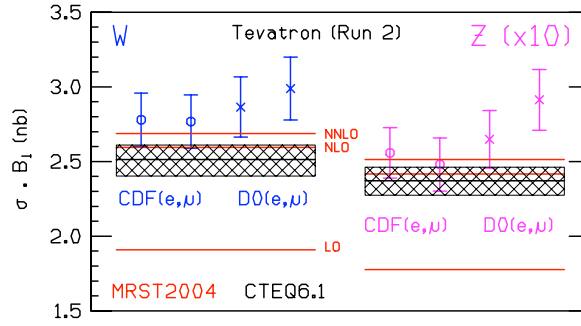
Figure 4. Predictions for the W and Z total cross sections at the Tevatron and LHC, using MRST2004 [10] and CTEQ6.1 pdfs [11], compared with recent data from CDF and D0. The MRST predictions are shown at LO, NLO and NNLO. The CTEQ6.1 NLO predictions and the accompanying pdf error bands are also shown.

of [10], with renormalization and factorization scales $\mu_F = \mu_R = M_W, M_Z$. The net effect of the NLO and NNLO corrections, which will be discussed in more detail in sections 3.3 and 3.4, is to increase the lowest-order cross section by about 25% and 5%, respectively.

Perhaps the most important point to note from figure 4 is that, aside from unknown (and presumably small) $O(\alpha_S{}^3)$ corrections, there is virtually no theoretical uncertainty associated with the predictions—the parton distributions are being probed in a range of $x \sim M_W/\sqrt{s}$ where they are constrained from deep-inelastic scattering, see figure 3, and the scale dependence is weak [10]. This overall agreement with experiment, therefore, provides a powerful test of the whole theoretical edifice that goes into the calculation. Figure 4 also illustrates the importance of higher-order perturbative corrections when making detailed comparisons of data and theory.
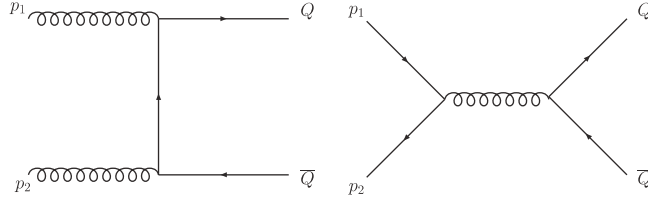
2.3. Heavy quark production

The production of heavy quarks at hadron colliders proceeds via Feynman diagrams such as the ones shown in figure 5. Therefore, unlike the Drell–Yan process that we have just discussed, in this case the cross section is sensitive to the gluon content of the incoming hadrons as well as the valence and sea quark distributions. The pdfs are probed at values of x_1 and x_2 given by (cf equation (10)),

$$x_1 = \frac{m_T}{\sqrt{s}} \left(e^{y_Q} + e^{y_{\bar{Q}}} \right) \qquad \text{and} \qquad x_2 = \frac{m_T}{\sqrt{s}} \left(e^{-y_Q} + e^{-y_{\bar{Q}}} \right), \qquad (13)$$

where m_T is the transverse mass given by $m_T = \sqrt{m_Q^2 + p_T^2}$, p_T is the transverse momentum of the quarks and y_Q, $y_{\bar{Q}}$ are the quark and antiquark rapidities. Although more complicated than in the Drell–Yan case, these relations may be simply derived using the same frame and notation as in (8) and writing, for instance, the 4-momentum of the outgoing heavy quark as,

$$p_Q^\mu = (m_T \cosh y_Q, \vec{p}_T, m_T \sinh y_Q), \qquad (14)$$

where $\vec{p}_T$ is the 2-component transverse momentum. From examining (13) it is clear that the dependence on the quark and gluon pdfs can vary considerably at different colliders ($\sqrt{s}$) and when producing different flavours of heavy quark (for instance, $m_c \approx 1.5\,\text{GeV}$ compared with $m_t \approx 175\,\text{GeV}$).

Figure 5. Representative Feynman diagrams for the production of a pair of heavy quarks at hadron colliders, via gg (left) and $q\bar{q}$ (right) initial states.

In this frame the heavy quark propagator that appears in the left-hand diagram of figure 5 can easily be evaluated. It is given by,

$$(p_Q - p_1)^2 - m_Q^2 = -2p_Q \cdot p_1 = -\sqrt{s}\, x_1 m_T (\cosh y_Q - \sinh y_Q) \,, \qquad (15)$$

which, when inserting the expression for x_1 in (13) reduces to the simple relation,

$$(p_Q - p_1)^2 - m_Q^2 = -m_T^2 \left(1 + \mathrm{e}^{(y_Q - y_{\bar{Q}})}\right) \,. \qquad (16)$$

Thus the propagator always remains off-shell, since $m_T^2 \geqslant m_Q^2$. This is in fact true for all the propagators that appear in the diagrams for heavy quark production. The addition of the mass scale m_Q sets a lower bound for the propagators—which would not occur if we considered the production of massless (or light) quarks, where the appropriate cutoff would be the scale Λ_{QCD}. Since the calculation would then enter the non-perturbative domain, such processes cannot be calculated in the same way as for heavy quarks; instead one must introduce a separate hard scale to render the calculation perturbative, as we shall discuss at more length in section 3.2. In contrast, as long as the quark is sufficiently heavy, $m_Q \gg \Lambda_{\mathrm{QCD}}$ (as is certainly the case for top and bottom quarks), the mass sets a scale at which perturbation theory is expected to hold.

Although we shall not concentrate on the many aspects of heavy quark processes in this paper, we will examine the success of perturbation theory for the case of top production at the Tevatron in section 5.5.
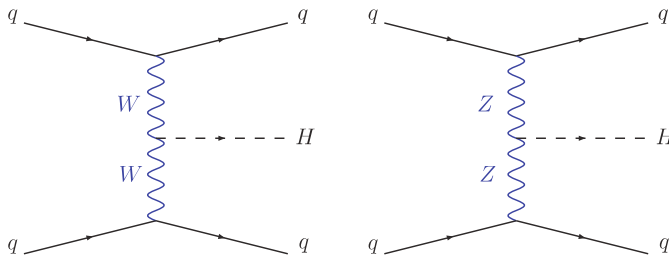
2.4. Higgs boson production

The search for the elusive Higgs boson has been the focus of much analysis at both the Tevatron and the LHC. As such, many different channels have been proposed in which to observe events containing Higgs bosons, including the production of a Higgs boson in association with a W or a Z as well as Higgs production with a pair of heavy quarks. However, the largest rate for a putative Higgs boson at both the Tevatron and the LHC results from the gluon-fusion process depicted in figure 6. Since the Higgs boson is responsible for giving mass to the particles in the Standard Model, it couples to fermions with a strength proportional to the fermion mass. Therefore, although any quark may circulate in the loop, the largest contribution by far results from the top quark. Since the LO diagram already contains a loop, the production of a Higgs boson in this way is considerably harder to calculate than the tree-level processes mentioned thus far—particularly when one starts to consider higher orders in perturbation theory or the radiation of additional hard jets.

For this reason it is convenient to formulate the diagram in figure 6 as an effective coupling of the Higgs boson to two gluons in the limit that the top quark is infinitely massive. Although formally one would expect that this approximation is valid only when all other scales in the problem are much smaller than m_t, in fact one finds that only $m_H < m_t$ (and p_T (jet) $< m_t$, when additional jets are present) is necessary for an accurate approximation [3]. Using this
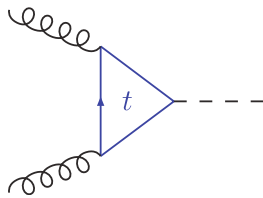
Figure 6. The 1-loop diagram representing Higgs production via gluon fusion at hadron colliders. The dominant contribution is from a top quark circulating in the loop, as illustrated.

Figure 7. Diagrams representing the production of a Higgs boson via the weak boson fusion mechanism.

approach the Higgs boson cross section via gluon fusion has been calculated to NNLO [4, 5], as we shall discuss further in section 3.4.

The second-largest Higgs boson cross section at the LHC is provided by the weak-boson fusion (WBF) mechanism, which proceeds via the exchange of W or Z bosons from incoming quarks, as shown in figure 7. Although this process is an electroweak one and therefore proceeds at a slower rate (about an order of magnitude lower than gluon fusion) it has a very clear experimental signature. The incoming quarks only receive a very small kick in their direction when radiating the W or Z bosons, so they can in principle be detected as jets very forward and backward at large absolute rapidities. At the same time, since no coloured particles are exchanged between the quark lines, very little hadronic radiation is expected in the central region of the detector. Therefore the type of event that is expected from this mechanism is often characterized by a 'rapidity gap' in the hadronic calorimeters of the experiment. As well as forming part of the search strategy for the Higgs boson, this channel opens up the possibility of measuring the nature of the Higgs coupling to vector bosons [6].

Although the scope of this review does not allow a lengthy discussion of the many facets of Higgs physics, including all its production mechanisms, decay modes, search strategies and properties, we will touch on a few important aspects of Higgs boson phenomenology, particularly in section 2.4. For a recent and more complete review of Higgs physics we refer the reader to [7].

2.5. W and Z transverse momentum distributions

Like Drell–Yan lepton pairs, most W and Z bosons (here collectively denoted by V) are produced with relatively little transverse momentum, i.e. $p_T \ll M_V$. In the leading-order model discussed in section 2.2, in which the colliding partons are assumed to be exactly collinear with the colliding beam particles, the gauge bosons are produced with zero transverse momentum. This approach does not take account of the intrinsic (non-perturbative) transverse motion of the quarks and gluons inside the colliding hadrons, nor of the possibility of generating large transverse momentum by recoil against additional energetic partons produced in the hard-scattering.

At very small p_T, the intrinsic transverse motion of the quarks and gluons inside the colliding hadrons, $k_T \sim \Lambda_{\mathrm{QCD}}$, cannot be neglected. Indeed the measured p_T distribution of Drell–Yan lepton pairs produced in fixed-target pN collisions is well parametrized by assuming a Gaussian distribution for the intrinsic transverse momentum with $\langle k_T \rangle \sim 700\,\mathrm{MeV}$, see for example [8]. However the data on the p_T distribution also show clear evidence of a hard, power-law tail, and it is natural to attribute this to the (perturbative) emission of one or more hard partons, i.e. $q\bar{q} \to Vg$, $qg \to Vq$, etc. The Feynman diagrams for these processes are identical to those for large p_T direct photon production, and the corresponding annihilation and Compton matrix elements are, for W production,

$$\sum |\mathcal{M}^{q\bar{q}' \to Wg}|^2 = \pi \alpha_S \sqrt{2} G_F M_W^2 |V_{qq'}|^2 \frac{8}{9} \frac{\hat{t}^2 + \hat{u}^2 + 2M_W^2 \hat{s}}{\hat{t}\hat{u}} \ ,$$

$$\sum |\mathcal{M}^{gq \to Wq'}|^2 = \pi \alpha_S \sqrt{2} G_F M_W^2 |V_{qq'}|^2 \frac{1}{3} \frac{\hat{s}^2 + \hat{u}^2 + 2\hat{t} M_W^2}{-\hat{s}\hat{u}} \ , \tag{17}$$

with similar results for the Z boson and for Drell–Yan lepton pairs. The sum is over colours and spins in the final and initial states, with appropriate averaging factors for the latter. The transverse momentum distribution $d\sigma/dp_T^2$ is then obtained by convoluting these matrix elements with parton distributions in the usual way. In principle, one can combine the hard (perturbative) and intrinsic (non-perturbative) contributions, for example using a convolution integral in transverse momentum space, to give a theoretical prediction valid for all p_T. A more refined prediction would then include next-to-leading-order ($O(\alpha_S^2)$) perturbative corrections, for example from processes like $q\bar{q} \to Vgg$, to the high p_T tail. Some fraction of the $O(\alpha_S)$ and $O(\alpha_S^2)$ contributions could be expected to correspond to distinct $V + 1$ jet and $V + 2$ jet final states, respectively.

However, a major problem in carrying out the above procedure is that the $2 \to 2$ matrix elements are singular when the final-state partons become soft and/or are emitted collinear with the initial-state partons. These singularities are related to the poles at $\hat{t} = 0$ and $\hat{u} = 0$ in the above matrix elements. In addition, processes like $q\bar{q} \to Vgg$ are singular when the two final-state gluons become collinear. This means in practice that the lowest-order perturbative contribution to the p_T distribution is singular as $p_T \to 0$ and that higher-order contributions from processes like $q\bar{q} \to Vgg$ are singular for any p_T.

The fact that the predictions of perturbative QCD *are* in fact finite for physical processes is due to a number of deep and powerful theorems (applicable to any quantum field theory) that guarantee that for suitably defined cross sections and distributions, the singularities arising from real and virtual parton emissions at intermediate stages of the calculation cancel when all contributions are included. We have already seen an example of this in the discussion above. The $O(\alpha_S)$ contribution to the total W cross section from the process $q\bar{q} \to Wg$ is singular when $p_T(W) = 0$ but, after due account is taken of the collinear singularity associated with DGLAP evolution of the quark distribution, this singularity is exactly cancelled by a $O(\alpha_S)$ contribution to the virtual gluon loop correction to $q\bar{q} \to W$. The net result is the finite NLO contribution to the cross section displayed in figure 4. The details of how and under what circumstances these cancellations take place will be discussed in the following section.

3. Partonic cross sections

3.1. Introduction

At the heart of the prediction of any hadron collider observable lies the calculation of the relevant hard-scattering process. In this section we will outline the perturbative approaches that are
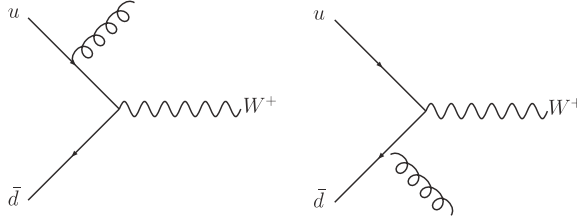
Figure 8. Lowest-order diagrams for the production of a W and one jet at hadron colliders.

employed to calculate these processes and describe some of their features and limitations. In addition, we will describe how the partonic calculations can be used to make predictions for an exclusive hadronic final state.

3.2. Lowest-order calculations

The simplest predictions can be obtained by calculating the lowest order in the perturbative expansion of the observable, as discussed in the previous section. This is performed by calculating the squared matrix element represented by tree-level Feynman diagrams and integrating this over the appropriate phase-space. For the simplest cases and for certain observables only, the phase-space integration can be performed analytically. For example, in section 2, we calculated the lowest-order cross section for Drell–Yan production. However, to obtain fully differential predictions in general, the integration must be carried out numerically. For most calculations, it is necessary to impose restrictions on the phase space in order that divergences in the matrix elements are avoided. This can best be understood by consideration of one of the simplest such cases, $W + 1$ jet production at a hadron collider.

3.2.1. $W + 1$ jet production. In figure 8, we have extended the LO diagrams for Drell–Yan production (for the specific initial-state $u\bar{d}$) by adding a final-state gluon to each of the initial-state quark legs. This is one of the subprocesses responsible for $W + 1$ jet production, with the other crossed process being $gq \to Wq$. After application of the Feynman rules, the squared matrix elements obtained from the sum of the diagrams take the form

$$|\mathcal{M}^{u\bar{d} \to W+g}|^2 \sim \left(\frac{\hat{t}^2 + \hat{u}^2 + 2Q^2\,\hat{s}}{\hat{t}\hat{u}} \right), \tag{18}$$

where Q^2 is the virtuality of the W boson, $\hat{s} = s_{u\bar{d}}$, $\hat{t} = s_{ug}$ and $\hat{u} = s_{\bar{d}g}$, cf (17) of section 2. This expression diverges in the limit where the gluon is unresolved—either it is collinear to one of the quarks ($\hat{t} \to 0$ or $\hat{u} \to 0$) or it is soft (both invariants vanish, so $E_g \to 0$). Let us consider the impact of these divergences on the calculation of this cross section. In order to turn the matrix elements into a cross section, one must convolute with pdfs and perform the integration over the appropriate phase space,

$$\sigma = \int dx_1 dx_2 \, f_u(x_1, Q^2) f_{\bar{d}}(x_2, Q^2) \frac{|\mathcal{M}|^2}{32\pi^2\hat{s}} \frac{d^3 p_W}{E_W} \frac{d^3 p_g}{E_g} \delta(p_u + p_{\bar{d}} - p_g - p_W), \tag{19}$$

where x_1, x_2 are the momentum fractions of the u and $\bar{d}$ quarks. These momentum fractions are of course related to the centre-of-mass energy squared of the collider s by the relation, $\hat{s} = x_1 x_2 s$.
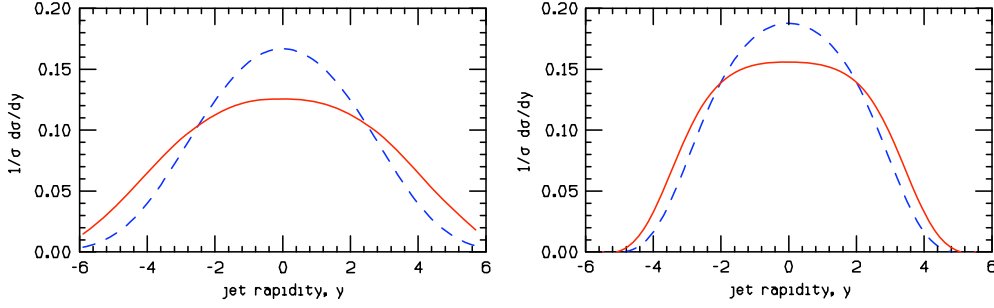
Figure 9. The rapidity distribution of the final-state parton found in a lowest-order calculation of the $W + 1$ jet cross section at the LHC. The parton is required to have a p_T larger than 2 GeV (left) or 50 GeV(right). Contributions from $q\bar{q}$ annihilation (solid red line) and the qg process (dashed blue line) are shown separately.

After suitable manipulations, this can be transformed into a cross section that is differential in Q^2 and the transverse momentum (p_T) and rapidity (y) of the W boson [39],

$$\frac{d\sigma}{dQ^2 dy dp_T^2} \sim \frac{1}{s} \int dy_g \, f_u(x_1, Q^2) f_{\bar{d}}(x_2, Q^2) \frac{|\mathcal{M}|^2}{\hat{s}}. \tag{20}$$

The remaining integral to be done is over the rapidity of the gluon, y_g. Note that the p_T of the gluon is related to the invariants of the process by $p_T^2 = \hat{t}\hat{u}/\hat{s}$. Thus the leading divergence represented by the third term of (18), where $\hat{t}$ and $\hat{u}$ both approach zero and the gluon is soft, can be written as $1/p_T^2$. Furthermore, in this limit $\hat{s} \to Q^2$, so that the behaviour of the cross section becomes

$$\frac{d\sigma}{dQ^2 dy dp_T^2} \sim \frac{2}{s} \frac{1}{p_T^2} \int dy_g \, f_u(x_1, Q^2) f_{\bar{d}}(x_2, Q^2) + (\text{sub-leading in } p_T^2). \tag{21}$$

As the p_T of the W boson becomes small, the limits on the y_g integration are given by $\pm \log(\sqrt{s}/p_T)$. Under the assumption that the rest of the integrand is approximately constant, the integral can be simply performed. This yields

$$\frac{d\sigma}{dQ^2 dy dp_T^2} \sim \frac{\log(s/p_T^2)}{p_T^2}, \tag{22}$$

so that the differential cross section contains a logarithmic dependence on p_T. If no cut is applied on the gluon p_T then the integral over p_T diverges—only after applying a minimum value of the p_T do we obtain a finite result. Once we apply a cutoff at $p_T = p_{T,\min}$ and then perform the integration, we find a result proportional to $\log^2(s/p_{T,\min}^2)$. This is typical of a fixed-order expansion—it is not merely an expansion in α_S, but in $\alpha_S \log(\ldots)$, where the argument of the logarithm depends upon the process and cuts under consideration. As we shall discuss later, these logarithms may be systematically accounted for in various all-orders treatments.

In figure 9 we show the rapidity distribution of the jet, calculated using this lowest-order process. In the calculation, a sum over all species of quarks has been performed and the contribution from the quark-gluon process included. The rapidity distribution is shown for two different choices of minimum jet transverse momentum, which is the cutoff used to regulate the collinear divergences discussed above. For very small values of p_T, we can view the radiated gluon as being emitted from the quark line at an early time, typically termed 'initial-state radiation'. From the left-hand plot, this radiation is indeed produced quite often
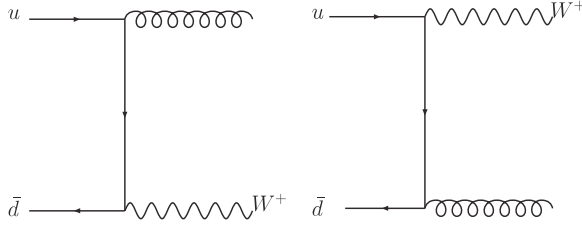
Figure 10. An alternative way of drawing the diagrams of figure 8.

at large rapidities, although it is also emitted centrally with a large probability. The canonical 'wisdom' is that initial-state radiation is primarily found in the forward region. There is indeed a collinear pole in the matrix element so that a fixed energy gluon tends to be emitted close to the original parton direction. However, we are interested not in fixed energy but rather in fixed transverse momentum. When using a higher p_T cutoff the gluon is emitted less often at large rapidities and is more central, as shown by the plot on the right-hand side. In this case, one can instead think of the diagrams as a $2 \rightarrow 2$ scattering as depicted in figure 10. Of course, the manner in which such Feynman diagrams are drawn is purely a matter of convention. The diagrams are exactly the same as in figure 8, but re-drawing them in this way is suggestive of the different kinematic region that is probed with a gluon at high p_T.

There is also a collinear pole involved for the emission of gluons from final-state partons. Thus, the gluons will be emitted preferentially near the direction of the emitting parton. In fact, it is just such emissions that give rise to the finite size of the jet arising from a single final-state parton originating from the hard-scatter. Much of the jet structure is determined by the hardest gluon emission; thus NLO theory, in which a jet consists of at most 2 partons, provides a good description of the jet shape observed in data [14].

3.2.2. W + 2 jet production. By adding a further parton, one can simulate the production of a $W + 2$ jet final state. Many different partonic processes contribute in general, so for the sake of illustration we just consider the production of a W boson in association with two gluons.

First, we shall study the singularity structure of the matrix elements in more detail. In the limit that one of the gluons, p_1, is soft the singularities in the matrix elements occur in 4 diagrams only. These diagrams, in which gluon p_1 is radiated from an external line, are depicted in figure 11. The remaining diagrams, in which gluon p_1 is attached to an internal line, do not give rise to singularities because the adjacent propagator does not vanish in this limit.

This is the first of our examples in which the matrix elements contain non-trivial colour structure. Denoting the colour labels of gluons p_1 and p_2 by t^A and t^B, respectively, diagram (1) is proportional to $t^B t^A$, whilst (2) is proportional to $t^A t^B$. The final two diagrams, (3a) and (3b), are each proportional to $f^{ABC} t^C$, which can of course be written as $(t^A t^B - t^B t^A)$. Using this identity, the amplitude (in the limit that p_1 is soft) can be written in a form in which the dependence on the colour matrices is factored out:

$$\mathcal{M}^{q\bar{q} \rightarrow Wgg} = t^A t^B (D_2 + D_3) + t^B t^A (D_1 - D_3), \tag{23}$$

so that the kinematic structures obtained from the Feynman rules are collected in the functions D_1, D_2 (for diagrams (1) and (2)) and D_3 (the sum of diagrams (3a) and (3b)). The combinations of these that appear in (23) are often referred to as colour-ordered amplitudes.
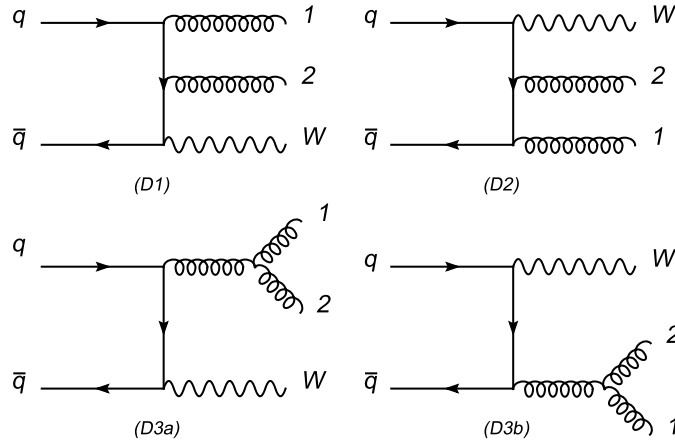
Figure 11. The 4 diagrams that contribute to the matrix elements for the production of $W+2$ gluons when gluon 1 is soft.

With the colour factors stripped out, it is straightforward to square the amplitude in (23) using the identities $\mathrm{tr}(t^A t^B t^B t^A) = N C_F^2$ and $\mathrm{tr}(t^A t^B t^A t^B) = -C_F/2$,

$$
\begin{aligned}
|\mathcal{M}^{q\bar{q} \to Wgg}|^2 &= N C_F^2 \left[|D_2 + D_3|^2 + |D_1 - D_3|^2 \right] - C_F \, \mathrm{Re} \left[(D_2 + D_3)(D_1 - D_3)^\star \right] \\
&= \frac{C_F N^2}{2} \left[|D_2 + D_3|^2 + |D_1 - D_3|^2 - \frac{1}{N^2} |D_1 + D_2|^2 \right].
\end{aligned}
\tag{24}
$$

Moreover, these colour-ordered amplitudes possess special factorization properties in the limit that gluon p_1 is soft. They can be written as the product of an eikonal term and the matrix elements containing only one gluon:

$$
\begin{aligned}
D_2 + D_3 &\longrightarrow \epsilon_\mu \left(\frac{q^\mu}{p_1 \cdot q} - \frac{p_2^\mu}{p_1 \cdot p_2} \right) \mathcal{M}_{q\bar{q} \to Wg}, \\
D_1 - D_3 &\longrightarrow \epsilon_\mu \left(\frac{p_2^\mu}{p_1 \cdot p_2} - \frac{\bar{q}^\mu}{p_1 \cdot \bar{q}} \right) \mathcal{M}_{q\bar{q} \to Wg},
\end{aligned}
\tag{25}
$$

where ϵ_μ is the polarization vector for gluon p_1. The squares of these eikonal terms are easily computed using the replacement $\epsilon_\mu \epsilon_\nu^\star \to -g_{\mu\nu}$ to sum over the gluon polarizations. This yields terms of the form

$$
\frac{a.b}{p_1.a \; p_1.b} \equiv [a \; b],
\tag{26}
$$

so that the final result is

$$
|\mathcal{M}^{q\bar{q} \to Wgg}|^2 \xrightarrow{\text{soft}} \frac{C_F N^2}{2} \left[[q \; p_2] + [p_2 \, \bar{q}] - \frac{1}{N^2} [q \, \bar{q}] \right] \mathcal{M}^{q\bar{q} \to Wg}.
\tag{27}
$$

Inspecting this equation, one can see that the leading term (in the number of colours) contains singularities along two lines of colour flow—one connecting the gluon p_2 to the quark, the other connecting it to the antiquark. On the other hand, the sub-leading term has singularities along the line connecting the quark and the antiquark. It is these lines of colour flow that indicate the preferred directions for the emission of additional gluons. In the sub-leading term the colour flow does not relate the gluon colour to the parent quarks at all. The matrix elements are in fact the same as those for the emission of two photons from a quark line (apart from overall coupling factors) with no unique assignment to either diagram 1 or diagram 2, unlike
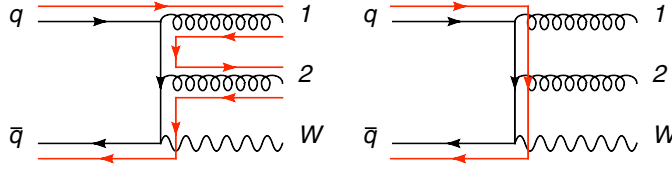
Figure 12. Two examples of colour flow in a $W + 2$ jet event, shown in red. In the left-hand diagram, a leading colour flow is shown. The right-hand diagram depicts the sub-leading colour flow resulting from interference.

the leading term. For this reason only the information about the leading colour flow is used by parton shower Monte Carlos such as HERWIG [15] and PYTHIA [16]. These lines of colour flow generalize in an obvious manner to higher multiplicity final states. As an example, the lines of colour flow in a $W + 2$ jet event are shown in figure 12.

Since all the partons are massless, it is trivial to re-write the eikonal factor of (26) in terms of the energy of the radiated gluon, E, and the angle it makes with the hard partons, θ_a, θ_b. It can then be combined with the phase space for the emitted gluon to yield a contribution such as,

$$[a\,b]\,\mathrm{d}PS_{\text{gluon}} = \frac{1}{E^2}\frac{1}{1-\cos\theta_a}\,E\mathrm{d}E\,\mathrm{d}\cos\theta_a\ . \tag{28}$$

In this form, it is clear that the cross section diverges as either $\cos\theta_a \to 1$ (the gluon is emitted collinear to parton a) or $E \to 0$ (for any angle of radiation). Moreover, each divergence is logarithmic and regulating the divergence, by providing a fixed cutoff (either in angle or energy), will produce a single logarithm from collinear configurations and another from soft ones—just as we found when considering the specific case of $W + 1$ jet production in the previous subsection.

This argument can be applied at successively higher orders of perturbation theory. Each gluon that is added yields an additional power of α_S and, via the eikonal factorization outlined above, can produce an additional two logarithms. This means that we can write the $W + 1$ jet cross section schematically as a sum of contributions:

$$\begin{aligned}\mathrm{d}\sigma = \sigma_0(W+1\text{ jet})\,&\big[1 + \alpha_S(c_{12}L^2 + c_{11}L + c_{10})\\&+\alpha_S{}^2(c_{24}L^4 + c_{23}L^3 + c_{22}L^2 + c_{21}L + c_{20}) + \cdots\big],\end{aligned} \tag{29}$$

where L represents the logarithm controlling the divergence, either soft or collinear. The size of L depends upon the criteria used to define the jets—the minimum transverse energy of a jet and the jet cone size. The coefficients c_{ij} in front of the logarithms depend upon colour factors. Note that the addition of each gluon results not just in an additional factor of α_S but in a factor of α_S times logarithms. For many important kinematic configurations, the logs can be large, leading to an enhanced probability for additional gluon emissions to occur. For inclusive quantities, where the same cuts are applied to every jet, the logs tend to be small, and counting powers of α_S become a valid estimator for the rate of production of additional jets.

Noticing that the factor $(\alpha_S L)$ appears throughout (29), it is useful to re-write the expansion in brackets as

$$\begin{aligned}\big[\cdots\big] &= 1 + \alpha_S L^2 c_{12} + (\alpha_S L^2)^2 c_{24} + \alpha_S L c_{11}(1 + \alpha_S L^2 c_{23}/c_{11} + \cdots) + \cdots\\&= \exp\big[c_{12}\alpha_S L^2 + c_{11}\alpha_S L\big],\end{aligned} \tag{30}$$
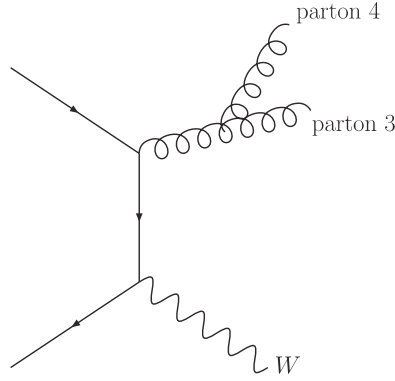
Figure 13. A final-state configuration containing a W and 2 partons. After the jet definition has been applied, either zero, one or two jets may be reconstructed.

where the infinite series have been resummed into an exponential form[6]. The first term in the exponent is commonly referred to as the leading logarithmic term, with the second being required in order to reproduce next-to-leading logarithms. This reorganization of the perturbative expansion is especially useful when the product $\alpha_S L$ is large, for instance when the logarithm is a ratio of two physical scales that are very different such as $\log(m_H/m_b)$. This exponential form is the basis of all-orders predictions and can be interpreted in terms of Sudakov probabilities, both subjects that we will return to in later discussions.

It is instructive to recast the discussion of the total W cross section in these terms, where the calculation is decomposed into components that each contain a given number of jets:

$$\sigma_W = \sigma_{W+0j} + \sigma_{W+1j} + \sigma_{W+2j} + \sigma_{W+3j} + \cdots. \tag{31}$$

Now, as in (29), we can further write out each contribution as an expansion in powers of α_S and logarithms:

$$\begin{aligned}
\sigma_{W+0j} &= a_0 + \alpha_S(a_{12}L^2 + a_{11}L + a_{10}) \\
&\quad + \alpha_S{}^2(a_{24}L^4 + a_{23}L^3 + a_{22}L^2 + a_{21}L + a_{20}) + \cdots, \\
\sigma_{W+1j} &= \alpha_S(b_{12}L^2 + b_{11}L + b_{10}) \\
&\quad + \alpha_S{}^2(b_{24}L^4 + b_{23}L^3 + b_{22}L^2 + b_{21}L + b_{20}) + \cdots, \\
\sigma_{W+2j} &= \cdots. \tag{32}
\end{aligned}$$

As the jet definitions change, the size of the logarithms shuffle the contributions from one jet cross section to another, whilst keeping the sum over all jet contributions the same. For example, as the jet cone size is decreased the logarithm L increases. As a result, the average jet multiplicity goes up and terms in (31) that represent relatively higher multiplicities will become more important.

This is illustrated in figure 13. Such a configuration may be reconstructed as an event containing up to two jets, depending upon the jet definition and the momenta of the partons. The matrix elements for this process contain terms proportional to $\alpha_S \log(p_{T,3}/p_{T,4})$ and $\alpha_S \log(1/\Delta R_{34})$ which is the reason that minimum values for the transverse energy and separation must be imposed. We shall see later that this is not the case in a full next-to-leading order calculation where these soft and collinear divergences are cancelled.

---

[6] Unfortunately, systematically collecting the terms in this way is far from trivial and only possible when considering certain observables and under specific choices of jet definition (such as when using the k_T-clustering algorithm).

Finally, we note that although the decomposition in (31) introduces quantities which are dependent upon the jet definition, we can recover results that are independent of these parameters by simply summing up the terms in the expansion that enter at the same order of perturbation theory, i.e. the a_{ij} and b_{ij} in equation (32) are not independent. As we will discuss shortly, in section 3.3, at a given order of perturbation theory the sum of the logarithms vanishes and we just recover the perturbative expansion of the total cross section:

$$\sigma_W^{LO} = a_0,$$
$$\sigma_W^{NLO} = \alpha_S \left(a_{10} + b_{10} \right).$$

3.2.3. Leading-order tools. Once suitable cuts have been applied, as we have discussed extensively above, leading-order cross sections can be calculated using a number of computer programs.

There is a wide range of programs available, most notably ALPGEN [17, 18], the COMPHEP package [19, 20] and MADGRAPH [21, 22]. All of these programs implement the calculation of the diagrams numerically and provide a suitable phase space over which they can be integrated. ALPGEN uses an approach which is not based on a traditional Feynman diagram evaluation [23], whereas the other two programs rely on more conventional methods such as the helicity amplitudes evaluation of HELAS [24] in MADGRAPH.

Although in principle these programs can be used to calculate any tree-level prediction, in practice the complexity of the process that may be studied is limited by the number of particles that is produced in the final state. This is largely due to the factorial growth in the number of Feynman diagrams that must be calculated. Even in approaches which do not rely directly on the Feynman diagrams, the growth is still as a power of the number of particles. For processes which involve a large number of quarks and gluons, as is the case when attempting to describe a multijet final state at a hadron collider such as the Tevatron or the LHC, an additional concern is the calculation of colour matrices which appear as coefficients in the amplitudes [25].

In many cases, such as in the calculation of amplitudes representing multiple gluon scattering, the final result is remarkably simple. Motivated by such results, the last couple of years has seen remarkable progress in the development of new approaches to QCD tree-level calculations. Some of the structure behind the amplitudes can be understood by transforming to 'twistor space' [26], in which amplitudes are represented by intersecting lines. This idea can be taken further with the introduction of 'MHV' rules [27], which use the simplest (maximally helicity-violating or MHV) amplitudes as the building blocks of more complicated ones. Although these rules at first only applied to amplitudes containing gluons, they were soon extended to cases of more general interest at hadron colliders [28–33]. Even more recently, further simplification of amplitudes has been obtained by using 'on-shell recursion relations' [34, 35]. As well as providing very compact expressions, this approach has the advantage of being both easily proven and readily extendable to processes involving fermions and vector bosons.

3.3. Next-to-leading order calculations

Although lowest-order calculations can in general describe broad features of a particular process and provide the first estimate of its cross section, in many cases this approximation is insufficient. The inherent uncertainty in a lowest-order calculation derives from its dependence on the unphysical renormalization and factorization scales, which is often large. In addition, some processes may contain large logarithms that need to be resummed or extra partonic processes may contribute only when going beyond the first approximation. Thus, in order
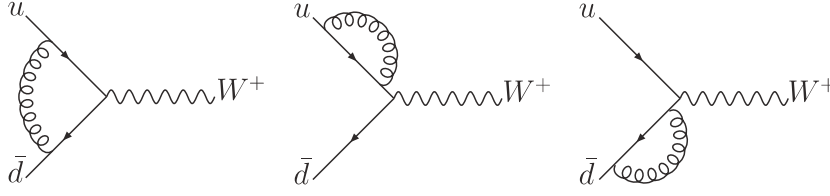
Figure 14. Virtual diagrams included in the next-to-leading order corrections to the Drell–Yan production of a W at hadron colliders.

to compare with predictions that have smaller theoretical uncertainties, next-to-leading order calculations are imperative for experimental analyses in Run II of the Tevatron and at the LHC.

3.3.1. Virtual and real radiation. A next-to-leading order QCD calculation requires the consideration of all diagrams that contribute an additional strong coupling factor, α_S. These diagrams are obtained from the lowest-order ones by adding additional quarks and gluons and they can be divided into two categories, virtual (or loop) contributions and the real radiation component. We shall illustrate this by considering the next-to-leading order corrections to the Drell–Yan production at a hadron collider. The virtual diagrams for this process are shown in figure 14 whilst the real diagrams are exactly the ones that enter the $W + 1$ jet calculation (in figure 8).

Let us first consider the virtual contributions. In order to evaluate the diagrams in figure 14, it is necessary to introduce an additional loop momentum ℓ which circulates around the loop in each diagram and is unconstrained. To complete the evaluation of these diagrams, one must therefore integrate over the momentum ℓ. However, the resulting contribution is not finite but contains infrared divergences—in the same way that the diagrams of figure 8 contain infrared (soft and collinear) singularities. By isolating the singularities appropriately, one can see that the divergences that appear in each contribution are equal but of opposite sign. The fact that the sum is finite is a demonstration of the theorems of Bloch and Nordsieck [36] and Kinoshita *et al* [37, 38], which guarantee that this is the case at all orders in perturbation theory and for any number of final-state particles.

The real contribution consists of the diagrams in figure 8, together with a quark–gluon scattering piece that can be obtained from these diagrams by interchanging the gluon in the final state with a quark (or antiquark) in the initial-state. As discussed in section 3.2.1, the quark–antiquark matrix elements contain a singularity as the gluon transverse momentum vanishes.

In our NLO calculation we want to carefully regulate and then isolate these singularities in order to extend the treatment down to zero transverse momentum. The most common method to regulate the singularities is dimensional regularization. In this approach the number of dimensions is continued to $D = 4 - 2\epsilon$, where $\epsilon < 0$, so that in intermediate stages the singularities appear as single and double poles in ϵ. After they have cancelled, the limit $D \to 4$ can be safely taken. Within this scheme, the cancellation of divergences between real and virtual terms can be seen schematically by consideration of a toy calculation [40]:

$$\mathcal{I} = \lim_{\epsilon \to 0} \left(\int_0^1 \frac{\mathrm{d}x}{x} x^{-\epsilon} \mathcal{M}(x) + \frac{1}{\epsilon} \mathcal{M}(0) \right). \tag{33}$$

Here, $\mathcal{M}(x)$ represents the real radiation matrix elements which are integrated over the extra phase space of the gluon emission, which contains a regulating factor $x^{-\epsilon}$. x represents a kinematic invariant which vanishes as the gluon becomes unresolved. The second term is
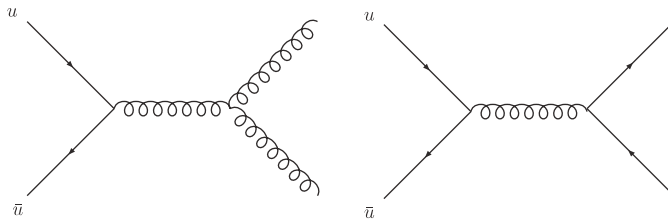
Figure 15. The leading-order diagrams representing inclusive jet production from a quark–antiquark initial-state.

representative of the virtual contribution, which contains an explicit pole, $1/\epsilon$, multiplying the lowest-order matrix elements, $\mathcal{M}(0)$.

Two main techniques have been developed for isolating the singularities, which are commonly referred to as the subtraction method [41–44] and phase-space slicing [45, 46]. For the sake of illustration, we shall consider only the subtraction method. In this approach, one explicitly adds and subtracts a divergent term such that the new real radiation integral is manifestly finite. In the toy integral this corresponds to

$$\mathcal{I} = \lim_{\epsilon \to 0} \left(\int_0^1 \frac{\mathrm{d}x}{x} x^{-\epsilon} \left[\mathcal{M}(x) - \mathcal{M}(0) \right] + \mathcal{M}(0) \int_0^1 \frac{\mathrm{d}x}{x} x^{-\epsilon} + \frac{1}{\epsilon} \mathcal{M}(0) \right)$$
$$= \int_0^1 \frac{\mathrm{d}x}{x} \left[\mathcal{M}(x) - \mathcal{M}(0) \right]. \tag{34}$$

This idea can be generalized in order to render finite the real radiation contribution to any process, with a separate counter-term for each singular region of phase space. Processes with a complicated phase space, such as $W + 2$ jet production, can end up with a large number of counterterms. NLO calculations are often set up to generate cross sections by histogramming 'events' generated with the relevant matrix elements. Such events cannot be directly interfaced to parton shower programs, which we will discuss later in section 3.5, as the presence of virtual corrections means that many of the events will have (often large) negative weights. Only the total sum of events over all relevant subprocesses will lead to a physically meaningful cross section.

The inclusion of real radiation diagrams in a NLO calculation extends the range of predictions that may be described by a lowest-order calculation. For instance, in the example above the W boson is produced with zero transverse momentum at lowest-order and only acquires a finite p_T at NLO. Even then, the W transverse momentum is exactly balanced by that of a single parton. In a real event, the W p_T is typically balanced by the sum of several jet transverse momenta. In a fixed-order calculation, these contributions would be included by moving to even higher orders so that, for instance, configurations where the W transverse momentum is balanced by two jets enter at NNLO. Although this feature is clear for the p_T distribution of the W, the same argument applies for other distributions and for more complex processes.

3.3.2. Scale dependence. One of the benefits of performing a calculation to higher order in perturbation theory is the reduction of the dependence of related predictions on the unphysical renormalization (μ_R) and factorization scales (μ_F). This can be demonstrated by considering inclusive jet production from a quark–antiquark initial-state [11], which is represented by the lowest-order diagrams shown in figure 15. This is a simplification of the full calculation but is the dominant contribution when the typical jet transverse momentum is large.

For this process, we can write the lowest-order prediction for the single jet inclusive distribution as

$$\frac{d\sigma}{dE_T} = \alpha_S^2(\mu_R)\,\sigma_0\,\otimes f_q(\mu_F) \otimes f_{\bar{q}}(\mu_F), \tag{35}$$

where σ_0 represents the lowest-order partonic cross section calculated from the diagrams of figure 15 and $f_i(\mu_F)$ is the parton distribution function for a parton i. Similarly, after including the next-to-leading order corrections, the prediction can be written as

$$\frac{d\sigma}{dE_T} = \left[\alpha_S^2(\mu_R)\sigma_0 + \alpha_S^3(\mu_R)\big(\sigma_1 + 2b_0 \log(\mu_R/E_T)\sigma_0 - 2P_{qq} \log(\mu_F/E_T)\sigma_0\big)\right]$$
$$\otimes f_q(\mu_F) \otimes f_{\bar{q}}(\mu_F). \tag{36}$$

In this expression the logarithms that explicitly involve the renormalization and factorization scales have been exposed. The remainder of the $\mathcal{O}(\alpha_S^3)$ corrections lies in the function σ_1.

From this expression, the sensitivity of the distribution to the renormalization scale is easily calculated using

$$\mu_R \frac{\partial \alpha_S(\mu_R)}{\partial \mu_R} = -b_0 \alpha_S^2(\mu_R) - b_1 \alpha_S^3(\mu_R) + \mathcal{O}(\alpha_S^4), \tag{37}$$

where the two leading coefficients in the beta-function, b_0 and b_1, are given by $b_0 = (33 - 2n_f)/6\pi$, $b_1 = (102 - 38n_f/3)/8\pi^2$. The contributions from the first and third terms in (36) cancel and the result vanishes, up to $\mathcal{O}(\alpha_S^4)$.

In a similar fashion, the factorization scale dependence can be calculated using the non-singlet DGLAP equation:

$$\mu_F \frac{\partial f_i(\mu_F)}{\partial \mu_F} = \alpha_S(\mu_F) P_{qq} \otimes f_i(\mu_F). \tag{38}$$

This time, the partial derivative of each parton distribution function, multiplied by the first term in (36), cancels with the final term. Thus, once again, the only remaining terms are of order α_S^4.

This is a generic feature of a next-to-leading order calculation. An observable that is predicted to order α_S^n is independent of the choice of either renormalization or factorization scale, up to the next higher order in α_S.

This discussion can be made more concrete by inserting numerical results into the formulae indicated above. For simplicity, we will consider only the renormalization scale dependence, with the factorization scale held fixed at $\mu_F = E_T$. In this case it is simple to extend (36) one higher order in α_S [51]:

$$\frac{d\sigma}{dE_T} = \left[\alpha_S^2(\mu_R)\,\sigma_0 + \alpha_S^3(\mu_R)\big(\sigma_1 + 2b_0 L\,\sigma_0\big)\right.$$
$$\left. + \alpha_S^4(\mu_R)\big(\sigma_2 + 3b_0 L\,\sigma_1 + (3b_0^2 L^2 + 2b_1 L)\,\sigma_0\big)\right] \otimes f_q(\mu_F) \otimes f_{\bar{q}}(\mu_F), \tag{39}$$

where the logarithm is abbreviated as $L \equiv \log(\mu_R/E_T)$. For a realistic example at the Tevatron Run I, $\sigma_0 = 24.4$ and $\sigma_1 = 101.5$. With these values the LO and NLO scale dependence can be calculated; the result is shown in figure 16, adapted from [51]. At the moment the value of σ_2 is unknown (see section 3.4). However, a range of predictions based on plausible values that it could take are also shown in the figure, $\sigma_2 = 0$ (solid) and $\sigma_2 = \pm\sigma_1^2/\sigma_0$ (dashed). It is clear that the renormalization scale dependence is reduced when going from LO and NLO and will become smaller still at NNLO.

Although figure 16 is representative of the situation found at NLO, the exact details depend upon the kinematics of the process under study and on choices such as the running of α_S and the pdfs used. Of particular interest are the positions on the NLO curve which correspond to
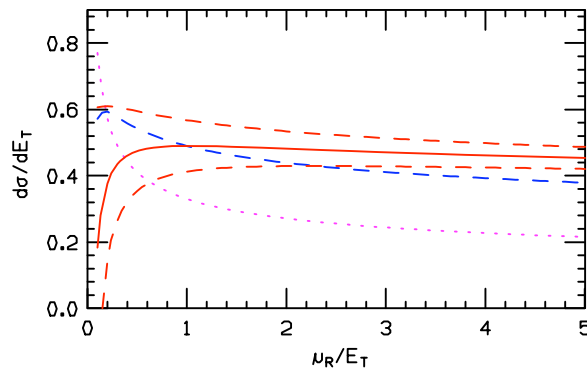
Figure 16. The single jet inclusive distribution at $E_T = 100$ GeV, appropriate for Run I of the Tevatron. Theoretical predictions are shown at LO (dotted magenta), NLO (dashed blue) and NNLO (red). Since the full NNLO calculation is not complete, three plausible possibilities are shown.

often-used scale choices. Due to the structure of (36) there will normally be a peak in the NLO curve, around which the scale dependence is minimized. The scale at which this peak occurs is often favoured as a choice. For example, for inclusive jet production at the Tevatron, a scale of $E_T^{\text{jet}}/2$ is usually chosen. This is near the peak of the NLO cross section for many kinematic regions. It is also usually near the scale at which the LO and NLO curves cross, i.e. when the NLO corrections do not change the LO cross section. Finally, a rather different motivation comes from the consideration of a 'physical' scale for the process. For instance, in the case of W production, one might think that a natural scale is the W mass. Clearly, these three typical methods for choosing the scale at which cross sections should be calculated do not in general agree. If they do, one may view it as a sign that the perturbative expansion is well behaved. If they do not agree then the range of predictions provided by the different choices can be ascribed to the 'theoretical error' on the calculation.

3.3.3. The NLO K-factor. The K-factor for a given process is a useful shorthand which encapsulates the strength of the NLO corrections to the lowest-order cross section. It is calculated by simply taking the ratio of the NLO to the LO cross section. In principle, the K-factor may be very different for various kinematic regions of the same process. In practice, the K-factor often varies slowly and may be approximated as one number.

However, when referring to a given K-factor one must take care to consider the cross section predictions that entered its calculation. For instance, the ratio can depend quite strongly on the pdfs that were used in both the LO and NLO evaluations. It is by now standard practice to use a NLO pdf (for instance, the CTEQ6M set) in evaluating the NLO cross section and a LO pdf (such as CTEQ6L) in the lowest-order calculation. Sometimes this is not the case; instead the same pdf set may be used for both predictions. Of course, if one wants to estimate the NLO effects on a lowest-order cross section, one should take care to match the appropriate K-factor.

A further complication is caused by the fact that the K-factor can depend quite strongly on the region of phase space that is being studied. The K-factor which is appropriate for the total cross section of a given process may be quite different from the one when stringent analysis cuts are applied. For processes in which basic cuts must be applied in order to obtain a finite cross section, the K-factor again depends upon the values of those cuts. Lastly, of course, as

Table 1. K-factors for various processes at the Tevatron and the LHC calculated using a selection of input parameters. In all cases, the CTEQ6M pdf set is used at NLO. $\mathcal{K}$ uses the CTEQ6L1 set at leading order, whilst $\mathcal{K}'$ uses the same set, CTEQ6M, as at NLO. Jets satisfy the requirements $p_T > 15\,\text{GeV}$ and $|\eta| < 2.5\,(5.0)$ at the Tevatron (LHC). In the $W + 2$ jet process the jets are separated by $\Delta R > 0.52$, whilst the weak boson fusion (WBF) calculations are performed for a Higgs boson of mass 120 GeV. Both renormalization and factorization scales are equal to the scale indicated.

| Process	Typical scales		Tevatron K-factor			LHC K-factor		
	μ_0	μ_1	$\mathcal{K}(\mu_0)$	$\mathcal{K}(\mu_1)$	$\mathcal{K}'(\mu_0)$	$\mathcal{K}(\mu_0)$	$\mathcal{K}(\mu_1)$	$\mathcal{K}'(\mu_0)$
W	m_W	$2m_W$	1.33	1.31	1.21	1.15	1.05	1.15
$W + 1$ jet	m_W	$\langle p_T^{\text{jet}} \rangle$	1.42	1.20	1.43	1.21	1.32	1.42
$W + 2$ jets	m_W	$\langle p_T^{\text{jet}} \rangle$	1.16	0.91	1.29	0.89	0.88	1.10
$t\bar{t}$	m_t	$2m_t$	1.08	1.31	1.24	1.40	1.59	1.48
$b\bar{b}$	m_b	$2m_b$	1.20	1.21	2.10	0.98	0.84	2.51
Higgs via WBF	m_H	$\langle p_T^{\text{jet}} \rangle$	1.07	0.97	1.07	1.23	1.34	1.09

can be seen from figure 16 the K-factor depends very strongly upon the renormalization and factorization scales at which it is evaluated. A K-factor can be less than, equal to or greater than 1, depending on all the factors described above.

As examples, in table 1 we show the K-factors that have been obtained for a few interesting processes at the Tevatron and the LHC. In each case the value of the K-factor is compared at two often-used scale choices, where the scale indicated is used for both renormalization and factorization scales. For comparison, we also note the K-factor that is obtained when using the same (CTEQ6M) pdf set at leading order and at NLO. In general, the difference when using CTEQ6L1 and CTEQ6M at leading order is not great. However, for the case of bottom production, the combination of the large difference in $\alpha_S(m_b^2)$ and the gluon distribution at small x results in very different K-factors. The values $\mathcal{K}'$ may, for instance, be useful in performing a NLO normalization of parton shower predictions, as we shall discuss in later sections.

Such K-factors can be used as estimators for the NLO corrections for the listed processes in situations where only the leading-order cross sections are available (for instance, when using a parton shower prediction). Note that, for the case of $W+$ jet production, we have two relevant scales for the hard-scattering process: m_W and the minimum allowed p_T^{jet}. If this threshold is quite low, as is the case in most studies at the Tevatron, these scales are quite different. Thus, there can be a fairly large variation in the size of the predicted cross section even at NLO, as illustrated in figure 17. In the leading-order calculation, the cross section varies by about a factor of 2.5 over the range of scales shown. Although this variation is reduced considerably at NLO, the cross section still increases by about 40% when moving from the highest scale shown to the lowest.

3.4. Next-to-next-to-leading order

With all the advantages of NLO, it is only natural to consider going deeper into the perturbative expansion. In the same sense that one only gains a reliable prediction of an observable at NLO, the first meaningful estimate of the theoretical error comes at NNLO. Further reduction of scale uncertainties is expected and, as we shall see, in cases where NLO corrections are large, it is a chance to check the convergence of the perturbative expansion.
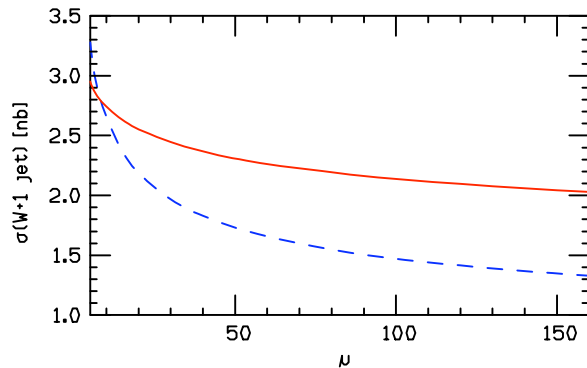
Figure 17. The LO (dashed) and NLO (solid) scale variation of the $W + 1$ jet cross section at the Tevatron, using the same inputs as in table 1.
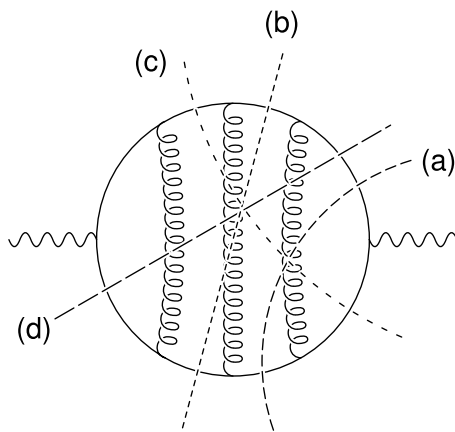
Figure 18. A 3-loop diagram which, when cut in all possible ways, shows the partonic contributions that must be calculated to perform a NNLO prediction of the $e^+e^- \to 3$ jets rate. A description of the contribution represented by each of the cuts (a)–(d) can be found in the text.

With these sorts of justifications in mind, a recent goal of theoretical effort has been the calculation of the 3 jet rate in e^+e^- annihilation to NNLO. Together with data from LEP and the SLC, this could be used to reduce the error on the measurement of $\alpha_S(M_Z^2)$ to a couple of per cent. However, the ingredients of a NNLO calculation are both more numerous and more complicated than those entering at NLO. The different contributions can best be understood by considering all possible cuts of a relevant $\mathcal{O}(\alpha_S^3)$ 3-loop diagram, as shown in figure 18.

The first contribution, represented by cut (a) in figure 18, corresponds to 2-loop 3-parton diagrams. As the result of much innovative work over the last few years, this contribution is now known (see, for example, [4–6] of [47]). The contribution labelled by (b) corresponds to the square of the 1-loop 3-parton matrix elements, the same ones which appear (interfered with tree-level) in the NLO calculation [41,45]. The third contribution (c) also contains 1-loop matrix elements, this time with 4 partons in the final state, one of which is unresolved. As in a NLO calculation, when one parton is unresolved this contribution diverges and a method must be developed to extract all singularities. Both these matrix elements [48–50,52] and such methods (for instance, [53] and references therein) have been known for some time.
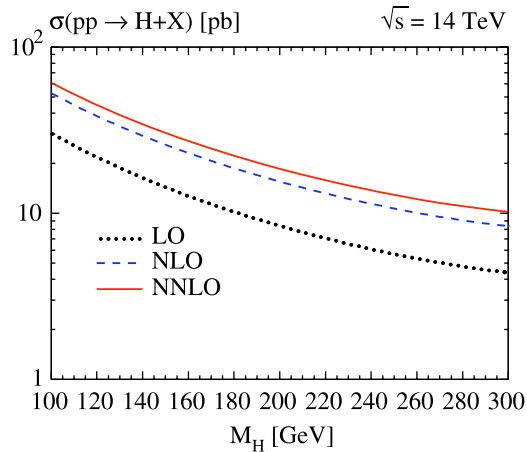
Figure 19. The inclusive Higgs boson cross section as a function of the Higgs boson mass.

The final contribution (d) involves only tree-level 5-parton matrix elements but has so far proven the stumbling block to a complete NNLO 3-jet calculation. This piece contains two unresolved partons and, just as before, this gives rise to singularities that must be subtracted. However, at present no general procedure for doing this exists and instead calculations can only be performed on a case-by-case basis. Quite recently a method has been developed for $e^+e^- \to$ jets calculations which has been used to calculate the doubly-unresolved sub-leading in N_c contribution to the 3-jet rate [47]. Such progress bodes well for the completion both of this calculation and the closely related 2-jet rate at hadron colliders[7].

The calculation that we have described represents the current frontier of NNLO predictions. For slightly simpler $2 \to 1$ and $2 \to 2$ processes, NNLO results are already available. The total inclusive cross section for the Drell–Yan process, production of a lepton pair by a W or Z in a hadronic collision, has long been known to NNLO accuracy [67]. In recent years the inclusive Higgs boson cross section, which is also a one-scale problem in the limit of large m_t, has also been computed at NNLO [4, 5]. For both these processes, the NLO corrections had already been observed to be large and the inclusion of the NNLO terms only provided a small further increase, thus stabilizing the perturbative expansion of these cross sections. This is illustrated in figure 19, taken from [4], which shows the inclusive Higgs boson cross section at the LHC at each order of perturbation theory.

The above calculations have now been extended to include rapidity cuts on the leptons in the Drell–Yan process, in order to be more applicable for studies at the LHC [68]. These calculations extend the method used in [5], which uses an ingenious trick to bypass the problems associated with doubly-unresolved radiation that we have described above. In this approach, the phase-space integrals are related to 2-loop integrals that are known and whose calculation can be automated. In this way, NNLO predictions can be provided for simple quantities such as rapidities. Further developments now allow for the introduction of generic cuts, paving the way for more detailed experimental analyses [69].

---

[7] A consistent NNLO calculation at a hadron collider also requires parton densities evolved at the same order, which is now possible thanks to the calculation of the QCD 3-loop splitting functions [65, 66]. The differences between NLO and NNLO parton densities are reasonably small though, throughout most of the x range.
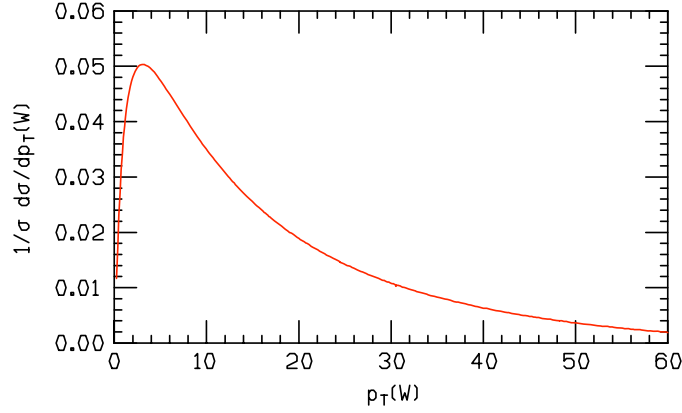
Figure 20. The resummed (leading log) W boson transverse momentum distribution.

3.5. All orders approaches

Rather than systematically calculating to higher and higher orders in the perturbative expansion of a given observable, a number of different 'all-orders' approaches are also commonly used to describe the phenomena observed at high-energy colliders. These alternative descriptions are typically most useful under a different set of conditions than a fixed-order approach. The merging of such a description with fixed-order calculations, in order to offer the best of both worlds, is of course highly desirable.

Resummation is one such approach, in which the dominant contributions from each order in perturbation theory are singled out and 'resummed' by the use of an evolution equation. Near the boundaries of phase space, fixed-order predictions break down due to large logarithmic corrections, as we have seen above. A straightforward example is provided by the production of a vector boson at hadron colliders. In this case, two large logarithms can be generated. One is associated with the production of the vector boson close to threshold ($\hat{s} = Q^2$) and takes the form $\alpha_S^n \log^{2n-1}(1 - z)/(1 - z)$, where $z = Q^2/\hat{s} - 1$. The other logarithm, as illustrated earlier, is associated with the recoil of the vector boson at very small transverse momenta p_T, so that logarithms appear as $\alpha_S^n \log^{2n-1}(Q^2/p_T^2)$, cf (22). Various methods for performing these resummations are available [70–77], with some techniques including both effects at the same time [78–80]. As we shall see later, the inclusion of such effects is crucial in order to describe data at the Tevatron and to estimate genuine non-perturbative effects. The ResBos program[8] [81] is a publicly available program that provides NLO resummed predictions for processes such as W, Z, $\gamma\gamma$ and Higgs boson production at hadron–hadron colliders. Resummation is of course not restricted to the study of these processes alone, with much progress recently in the resummation of event shape variables at hadron colliders (for a recent review, see [82]).

The expression for the W boson transverse momentum in which the leading logarithms have been resummed to all orders is given by (cf (22) and (30))

$$\frac{d\sigma}{dp_T^2} = \sigma \frac{d}{dp_T^2} \exp\left(-\frac{\alpha_S C_F}{2\pi} \log^2 M_W^2/p_T^2\right). \tag{40}$$

This describes the basic shape for the transverse distribution for W production, which is shown in figure 20. Note that in this approximation the p_T^2 distribution vanishes as $p_T \to 0$, a feature

---

[8] http://hep.pa.msu.edu/people/cao/ResBos-A.html

which is not seen experimentally. However this can be explained by the fact that the only configuration included as $p_T \rightarrow 0$ is the one in which all emitted gluons are soft. In reality (and in a more complete resummed prediction), multiple gluon emissions with a vector sum equal to p_T contribute and fill in the dip at $p_T = 0$.

A different, but related, approach is provided by parton showers. The numerical implementation of a parton shower, for instance in the programs PYTHIA, HERWIG (HERWIG++ [83]) and SHERPA [84], is a common tool used in many current physics analyses. By the use of the parton showering process, a few partons produced in a hard interaction at a high-energy scale can be related to partons at an energy scale close to Λ_{QCD}. At this lower energy scale, a universal non-perturbative model can then be used to provide the transition from partons to the hadrons that are observed experimentally. This is possible because the parton showering allows for the evolution, using the DGLAP formalism, of the parton fragmentation function. The solution of this DGLAP evolution equation can be rewritten with the help of the Sudakov form factor, which indicates the probability of evolving from a higher scale to a lower scale without the emission of a gluon greater than a given value. For the case of parton showers from the initial-state, the evolution proceeds backwards from the hard scale of the process to the cutoff scale, with the Sudakov form factors being weighted by the parton distribution functions at the relevant scales.

In the parton showering process, successive values of an evolution variable t, a momentum fraction z and an azimuthal angle ϕ are generated, along with the flavours of the partons emitted during the showering. The evolution variable t can be the virtuality of the parent parton (as in PYTHIA versions 6.2 and earlier and in SHERPA), $E^2(1 - \cos\theta)$, where E is the energy of the parent parton and θ is the opening angle between the two partons (as in HERWIG)[9] or the square of the relative transverse momentum of the two partons in the splitting (as in PYTHIA 6.3). The HERWIG evolution variable has angular ordering built in, angular ordering is implicit in the PYTHIA 6.3 [85] evolution variable and angular ordering has to be imposed after the fact for the PYTHIA 6.2 evolution variable. Angular ordering represents an attempt to simulate more precisely those higher-order contributions that are enhanced due to soft gluon emission (colour coherence). Fixed-order calculations explicitly account for colour coherence, while parton shower Monte Carlos that include colour-flow information model it only approximately.

Note that with parton showering, we in principle introduce two new scales, one for initial-state parton showering and one for the shower in the final state. In the PYTHIA Monte Carlo, the scale used is most often related to the maximum virtuality in the hard-scattering, although a larger ad hoc scale, such as the total centre-of-mass energy, can also be chosen by the user. The HERWIG showering scale is determined by the specific colour flow in the hard process and is related to the invariant mass of the colour connected partons.

We can write an expression for the Sudakov form factor of an initial-state parton in the form shown in (41), where t is the hard scale, t_0 is the cutoff scale and $P(z)$ is the splitting function for the branching under consideration:

$$\Delta(t) \equiv \exp\left[-\int_{t_0}^{t} \frac{dt'}{t'} \int \frac{dz}{z} \frac{\alpha_S}{2\pi} P(z) \frac{f(x/z, t)}{f(x, t)}\right]. \tag{41}$$

The Sudakov form factor has a similar form for the final state but without the pdf weighting. The introduction of the Sudakov form factor resums all the effects of soft and collinear gluon emission, which leads to well-defined predictions even in these regions. However, this ability comes at a price. Although the soft and collinear regions are logarithmically enhanced and thus the dominant effect, this method does not attempt to correctly include the non-singular

---

[9] An extension of this angular variable that allows for showering from heavy objects has been implemented in HERWIG++.
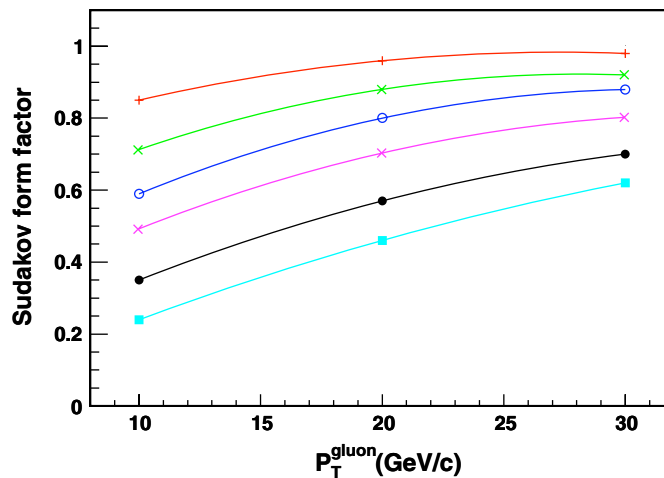
Figure 21. The Sudakov form factors for initial-state gluons at a hard scale of 100 GeV as a function of the transverse momentum of the emitted gluon. The form factors are for (top to bottom) parton x values of 0.3, 0.1, 0.03, 0.01, 0.001 and 0.0001.

contributions that are due to large energy, wide angle gluon emission. We shall return to this discussion later.

3.5.1. Sudakov form factors.   As discussed in the previous section, the Sudakov form factor gives the probability for a parton to evolve from a harder scale to a softer scale without emitting a parton harder than some resolution scale, either in the initial-state or in the final state. Sudakov form factors form the basis for both parton showering and resummation. Typically, the details of the form factors are buried inside the interior of such programs. It is useful, however, to generate plots of the initial-state Sudakov form factors for the kinematic conditions encountered at both the Tevatron and LHC. Such plots indicate the likelihood for the non-radiation of gluons from the initial-state partons, and thus conversely for the radiation of at least one such gluon. Thus, they can also serve as a handy reference for the probability of jets from initial-state radiation. A Sudakov form factor will depend on (1) the parton type (quark or gluon), (2) the momentum fraction x of the initial-state parton, (3) the hard and cutoff scales for the process and (4) the resolution scale for the emission. Several examples are discussed below. These plots were generated with the HERWIG++ parton shower formalism [86][10].

In figure 21 are plotted the Sudakov form factors for the splitting $g \rightarrow gg$, at a hard scale of 100 GeV, and for several different values of the parton x value. The form factors are plotted versus the resolution scale for the emitted gluon, which can be thought of roughly as the transverse momentum of the emitted gluon. The probability for no emission decreases as the transverse momentum of the emitted gluon decreases and as the parton x decreases. The former is fairly obvious; the latter may not be so. The smaller the value of the initial parton momentum fraction, the larger is the possible phase space for gluon emission.

For example, the probability for a gluon with an x value of 0.03 to evolve from 100 GeV down to 10 GeV without emitting a gluon of 10 GeV or greater can be read off the plot as being 60%; thus the probability for at least one such emission is 40%. This is another example where the probability of emission of a hard gluon is enhanced by a logarithm (in this case the

[10] We thank Stefan Gieseke for providing us with the relevant information.
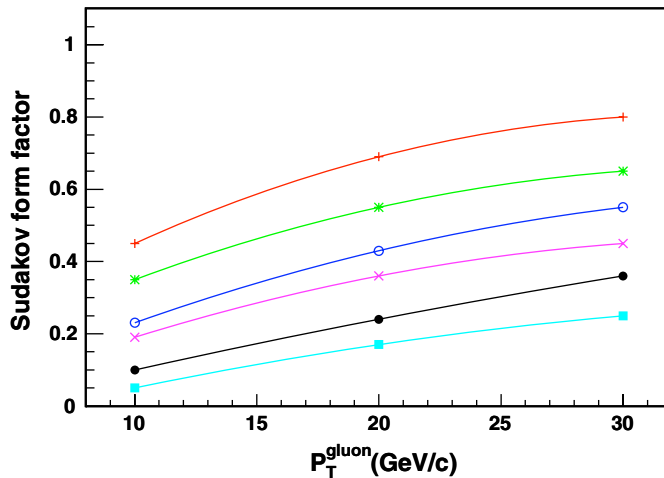
Figure 22. The Sudakov form factors for initial-state gluons at a hard scale of 500 GeV as a function of the transverse momentum of the emitted gluon. The form factors are for (top to bottom) parton x values of 0.3, 0.1, 0.03, 0.01, 0.001 and 0.0001.

ratio of the hard scale to the resolution scale) compared with the naive expectation of a factor of α_S. The probability of emission of such a gluon from an initial-state gluon on the opposite side of the collision would of course be the same.

In figure 22, the same Sudakov form factors are plotted but now using a hard scale of 500 GeV. The increased probability of a hard gluon emission can be observed. In figures 23 and 24, the Sudakov form factors are plotted for the hard scales of 100 and 500 GeV as before but now for the splitting $q \to qg$. The probability of no emission is larger, due to the smaller colour factor of the initial-state quark compared with the gluon. Note that the form factor curves for x values of less than 0.03 have not been plotted as they would essentially lie on top of the $x = 0.03$ curve. It is not the smaller colour factor that causes the difference with the gluon but rather the splitting function. The splitting function for $g \to gg$ has singularities both as $z \to 0$ and as $z \to 1$, while the $q \to qg$ has only the $z \to 1$ singularity. Thus, for the $q \to qg$ splitting, there is not much to gain from decreasing x on a logarithmic scale, as there is no singularity at $z = 0$ in the splitting function.

3.6. Partons and jet algorithms

In the detectors of experiments at the Tevatron and the LHC, collimated beams of particles are observed. In order to categorize these events, the hadrons are collected into jets using a jet algorithm. To make a comparison with a theoretical calculation of the types we have been discussing, it is necessary to also apply a jet algorithm at the parton level. Ideally, one would like an algorithm which yields similar results at the experimental (hadron) and theoretical (parton) levels. The goal is to characterize the short-distance physics event-by-event, in terms of the jets formed by the algorithm.

There are two essential stages for any jet algorithm. First, the objects belonging to a cluster are identified. Second, the kinematic variables defining the jet are calculated from the objects defining the cluster. The two stages are independent. For the latter stage, using the jet algorithms developed for Run 2 at the Tevatron, the jet kinematic properties are defined (using a 4-vector recombination scheme) in terms of p^{jet}, p_T^{jet}, y^{jet} and ϕ^{jet}.
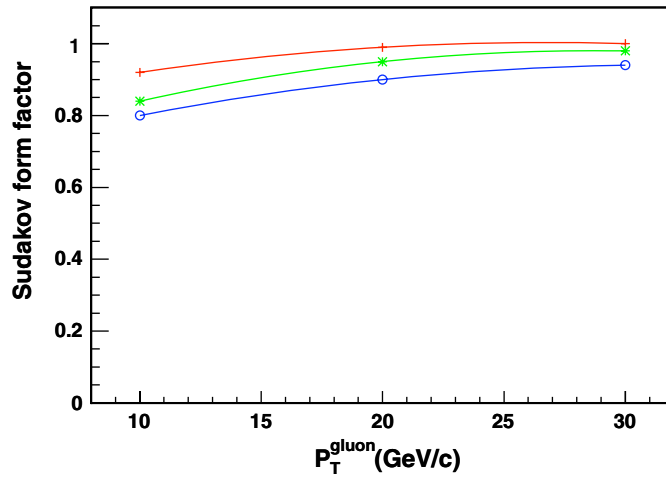
Figure 23. The Sudakov form factors for initial-state quarks at a hard scale of 100 GeV as a function of the transverse momentum of the emitted gluon. The form factors are for (top to bottom) parton x values of 0.3, 0.1 and 0.03.
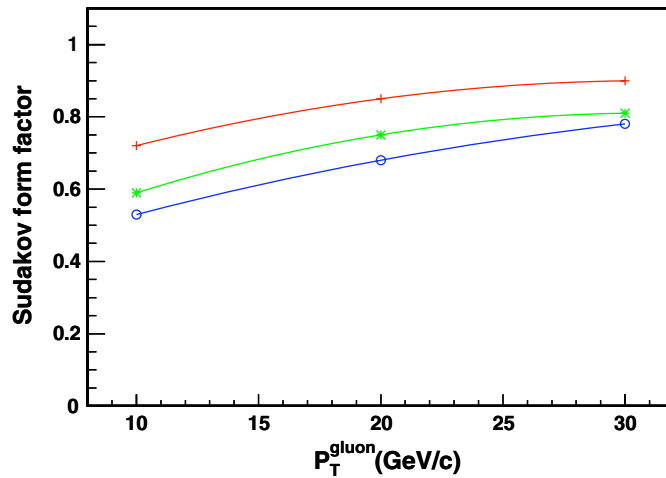
Figure 24. The Sudakov form factors for initial-state quarks at a hard scale of 500 GeV as a function of the transverse momentum of the emitted gluon. The form factors are for (top to bottom) parton x values of 0.3, 0.1 and 0.03.

At the experimental or simulated data level, jet algorithms cluster together objects such as particles or energies measured in calorimeter cells. At the theoretical level, partons are clustered. The goal of a jet algorithm is to produce similar results no matter at what level it is applied. For a $2 \rightarrow 2$ LO calculation, a jet consists simply of 1 parton and no jet algorithm is necessary. As more partons are added to a calculation, the complexity of a jet grows and approaches the complexity found either in parton shower Monte Carlos or in data. For all situations in which a jet can consist of more than 1 parton, a completely specified jet algorithm is needed. The clustering algorithms rely on the association of these objects based on transverse momentum (the k_T algorithm) [87] or angles (the cone algorithm), relative to a jet axis.

For NLO calculations, as for example $W + 2$ jets, a jet can consist of either 1 or 2 partons. Cone jet algorithms as currently used by the Tevatron experiments require the use of seeds (initial directions for jet cones) as the starting points for jet searches. For a partonic level final state, the seeds are the partons themselves. The Run 2 cone algorithm (midpoint) places additional seeds between stable cones having a separation of less than twice the size of the clustering cones; the use of these additional seeds removes problems with infrared instabilities in theoretical calculations. Without a midpoint seed, a jet could be formed/not formed depending on the presence of a soft gluon between two hard partons; this leads to an undesirable logarithmic dependence of the cross section on the energy of this soft gluon.

With a cone algorithm, two partons are nominally included in the same jet if they are within R_{cone} of the p_T-weighted jet centroid and so within a maximum ΔR of 1.4 of each other if a cone radius of 0.7 is used. However, it was noted that with the experimental jet algorithms used at the Tevatron, the two jets would not be merged into a single jet if they were separated by a distance greater than 1.3 times the cone radius. Thus, a phenomenological parameter $R_{\text{sep}} = 1.3$ was added to the theoretical prediction; two partons would not be merged into a single jet if they were separated by more than $R_{\text{sep}} \times R_{\text{cone}}$ from each other. So, in a parton level calculation having at most 3 partons in the final state, two partons are merged into the same jet if they are within R_{cone} of the p_T-weighted jet centroid and within $R_{\text{sep}} \times R_{\text{cone}}$ of each other; otherwise the two partons are termed separate jets. Thus, for $W + 2$ jet production at NLO, the final state can consist of either 2 or 3 partons. The 2 parton final state will always be reconstructed as 2 jets; the 3 parton final state may be reconstructed as either 2 or 3 jets depending on whether the 2 lowest p_T partons satisfy the clustering criteria described above. Note that for some partonic level programs such as JETRAD [88], the clustering is not performed prior to the evaluation of the matrix element. Thus, the individual transverse momenta of the jets are also not known at this time; only the transverse momentum of the highest p_T parton, which by momentum conservation must remain unclustered, is known. For this reason, a renormalization/factorization scale of p_T^{max} (the p_T of this parton) is used in calculating the cross section of each jet.

A schematic diagram indicating the region in which two partons will be included in the same jet is shown in figure 25 [89]. All partons within R_{cone} of each other will always be clustered in the same jet. This corresponds to the region labelled I. An ideal cone algorithm acting on data would cluster together only the underlying parton level configurations corresponding to region II and not configurations in region III. However, as will be seen in section 5, the stochastic character of the parton showering and hadronization process makes such a clean division difficult in either real data or with a parton shower Monte Carlo. Because the matrix element for the emission of an additional real parton has both a collinear and soft pole, configurations in regions II and III with two partons having ΔR near 0.7 and z near 0 will be most heavily populated. The fractional contribution to the inclusive jet cross section of the merged two parton configurations in Region II is proportional to $\alpha_S(p_T^2)$ and thus should decrease with increasing jet transverse momentum.

The k_T algorithm [87] is conceptually simpler at all levels. Two partons (or particles or energies) in calorimeter towers are combined if their relative transverse momentum is less than a given measure. At the parton level, each parton is considered as a proto-jet. The quantities $k_{T,i}^2 = P_{T,i}^2$ and $k_{T,(i,j)} = \min(P_{T,i}^2, P_{T,j}^2) \cdot \Delta R_{i,j}^2 / D^2$ are computed for each parton and each pair of partons, respectively. $P_{T,i}$ is the transverse momentum of the ith parton, $\Delta R_{i,j}$ is the distance (in y, ϕ space) between each pair of partons and D is a parameter that controls the size of the jet. If the smallest of the above quantities is a $k_{T,i}$ then that parton becomes a jet; if the smallest quantity is a $k_{T,(i,j)}$, then the two partons are combined into a single proto-jet
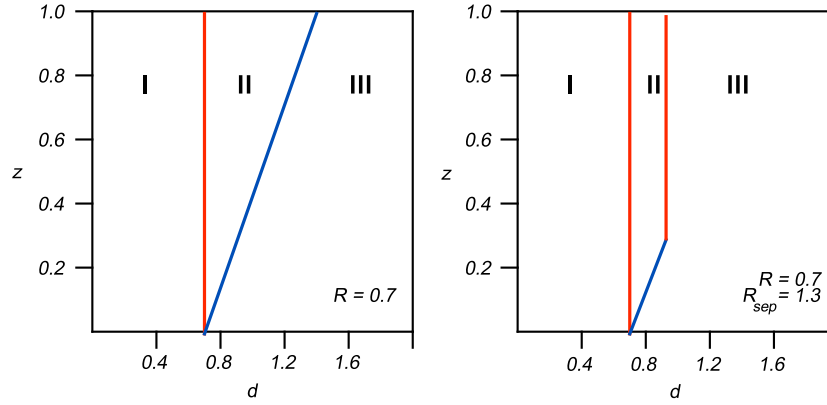
Figure 25. The parameter space (d, Z) for which two partons will be merged into a single jet.

by summing their four-vector components. In a NLO inclusive jet calculation, the two lowest p_T partons may be combined into a single jet, and thus the final state can consist of either 2 or 3 jets, as was also true for the case of the cone algorithm. The k_T algorithm merges two partons into a single jet if $\Delta R_{ij} < D$. In figure 25, if D is set to R_{cone}, the k_T algorithm would merge partons for which $d < R$ or in the language used above for the cone algorithm, $R_{sep} = 1$. Since the cone algorithm merges the partons not only for $d < R$ but also in the triangular region above the line $d = R(1 + z)$, a cone jet cross section at the parton level, for cone radius R, will necessarily be larger than a k_T jet cross section with $D = R$. If we use an R_{sep} value of 1.3 rather than 2 for the cone algorithm, the difference in relative cross sections between the two algorithms will be reduced. As we will see in section 5, this relative behaviour of the two algorithms does not hold at the hadron level.

The assumption we are making above is that the jets of hadrons measured in a collider experiment can be represented by the 1 or 2 partons that comprise a jet at the NLO theoretical level. That is, the 1 or 2 partons present in a NLO jet effectively represent the many partons produced by a parton shower. For example, an equivalent description of the jet shape is provided by the two types of calculation. This approximation has been borne out in practice with one remaining correction being necessary. Partons whose trajectories lie inside the jet cone eventually produce hadrons, some of which may land outside the cone due to the fragmentation process. The fragmentation correction takes a particularly simple form. For a cone of radius 0.7, each jet loses approximately 1 GeV due to fragmentation, basically independent of the jet transverse energy. The naïve assumption might be that the energy outside the cone due to fragmentation would rise with the jet energy; however, the jet becomes narrower at higher E_T, leading to a roughly constant amount of energy in the outermost portions of the jet. As will be described in section 5, corrections also need to be applied to the data or to the theory to take into account the underlying event energy.

A quantity related to the jet shape is the jet mass. To first order, the jet mass, like the jet shape, is determined by the hardest gluon emission. This emission is governed by the Sudakov form factor, and thus the jet mass distribution should fall roughly as $1/m^2$, with modification at the two endpoints. There will be a Sudakov suppression for low jet masses (corresponding to little or no gluon emission), and at high jet masses the jet algorithm will tend to break the jet up into two separate jets. The average mass for this falling distribution will be approximately 10–15% of the transverse momentum of the jet.

3.7. Merging parton showers and fixed order

As we have discussed previously in section 3.5, parton showers provide an excellent description in regions which are dominated by soft and collinear gluon emission. On the other hand, matrix element calculations provide a good description of processes where the partons are energetic and widely separated and, in addition, include the effects of interference between amplitudes with the same external partons. But, on the other hand, the matrix element calculations do not take into account the interference effects in soft and collinear gluon emissions which cannot be resolved, and which lead to a Sudakov suppression of such emissions.

Clearly, a description of a hard interaction which combines the two types of calculations would be preferable. For this combination to take place, there first needs to be a universal formalism that allows the matrix element calculation to 'talk' to the parton shower Monte Carlo. Such a universal formalism was crafted during the Les Houches Workshop on Collider Physics in 2001 and the resulting 'Les Houches Accord' is in common use [90]. The accord specifies an interface between the matrix element and the parton shower program which provides information on the parton 4-vectors, the mother–daughter relationships and the spin/helicities and colour flow. It also points to intermediate particles whose mass should be preserved in the parton showering. All the details are invisible to the casual user and are intended for the matrix element/parton shower authors.

Some care must be taken, however, as a straight addition of the two techniques would lead to double-counting in kinematic regions where the two calculations overlap. There have been many examples where matrix element information has been used to correct the first or the hardest emission in a parton shower. There are also more general techniques that allow matrix element calculations and parton showers each to be used in kinematic regions where they provide the best description of the event properties and that avoid double-counting. One such technique is termed CKKW [91].

With the CKKW technique, the matrix element description is used to describe parton branchings at large angle and/or energy, while the parton shower description is used for the smaller angle, lower energy emissions. The phase space for parton emission is thus divided into two regions, matrix element dominated and parton shower dominated, using a resolution parameter d_{ini}. The argument of α_S at all the vertices is chosen to be equal to the resolution parameter d_i at which the branching has taken place and Sudakov form factors are inserted on all the quark and gluon lines to represent the lack of any emissions with a scale larger than d_{ini} between vertices. The d_i represent a virtuality or energy scale. Parton showering is used to produce additional emissions at scales less than d_{ini}. For a typical matching scale, approximately 10% of the n-jet cross section is produced by parton showering from the n-1 parton matrix element; the rest arises mostly from the n-parton matrix element. A schematic representation of the CKKW scheme is shown in figure 26 for the case of $W+$ jets production at a hadron–hadron collider. A description of a $W + 2$ jet event in the NLO formalism is also shown for comparison.

The CKKW procedure provides a matching between the matrix element and parton shower that should be correct to the next-to-leading-logarithm (NLL) level. There are, however, a number of choices that must be made in the matching procedure that do not formally affect the logarithmic behaviour but do affect the numerical predictions, on the order of 20–30%. The CKKW procedure gives the right amount of radiation but tends to put some of it in the wrong place with the wrong colour flow. Variations that result from these choices must be considered as part of the systematic error inherent in the CKKW process. This will be discussed further in section 5.
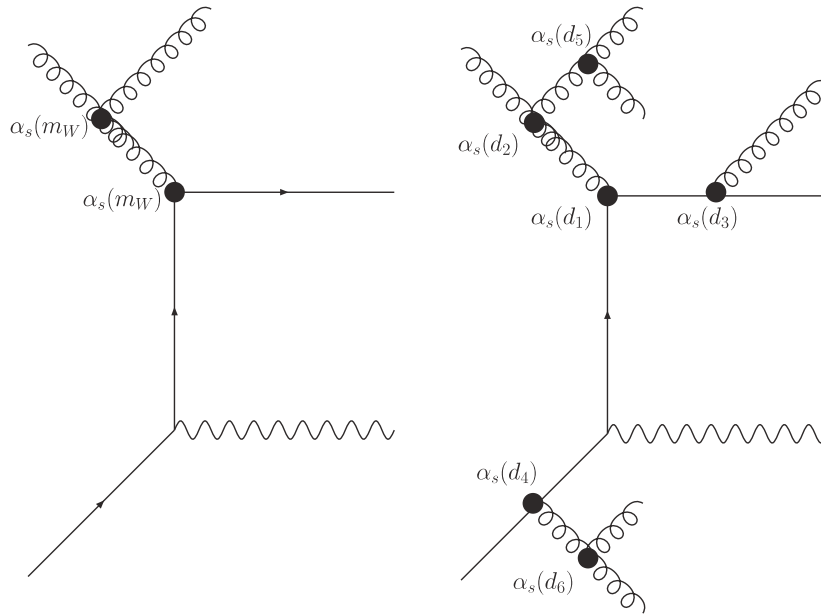
Figure 26. In the NLO formalism, the same scale, proportional to the hardness of the process, is used for each QCD vertex. For the case of the $W+2$ jet diagram shown above to the left, a scale related to the mass of the W boson, or to the average transverse momentum of the produced jets, is typically used. The figure to the right shows the results of a simulation using the CKKW formalism. Branchings occur at the vertices with resolution parameters d_i, where $d_1 > d_2 \gg d_{ini} > d_3 > d_4 > d_5 > d_6$. Branchings at the vertices 1–2 are produced with matrix element information while the branchings at vertices 3–6 are produced by the parton shower.

For the CKKW formalism to work, matrix element information must in principle be available for any number n of partons in the final state. Practically speaking, having information available for n up to 4 is sufficient for the description of most events at the Tevatron or LHC. The CKKW formalism is implemented in the parton shower Monte Carlo SHERPA [92] and has also been used for event generation at the Tevatron and LHC using the Mrenna–Richardson formalism [94]. An approximate version of CKKW matching (the 'MLM approach'[11]) is available in ALPGEN 2.0 [18].

3.8. Merging NLO calculations and parton showers

A combination of NLO calculations with parton shower Monte Carlos leads to the best of both worlds. The NLO aspect leads to a correct prediction for the rate of the process and also improves the description of the first hard parton emission. The parton shower aspect provides a sensible description of multiple/soft collinear emissions with a final state consisting of hadrons, which can then be input to a detector simulation. In a parton shower interface, a specific subtraction scheme must be implemented to preserve the NLO cross section. As each parton shower Monte Carlo may produce a different real radiation component, the subtraction scheme must necessarily depend on the Monte Carlo program to which the matrix element program is matched. The presence of interference effects with NLO calculations requires that a relatively small fraction ($\sim 10\%$) of events have negative weights (of value -1).

[11] ...which one of the authors takes credit for naming.

Several groups have worked on the subject to consistently combine partonic NLO calculations with parton showers.

- Collins, Zu [95, 96].
- Frixione, Nason, Webber (MC@NLO) [97–99].
- Kurihara, Fujimoto, Ishikawa, Kato, Kawabata, Munehisa, Tanaka [100].
- Krämer, Soper [101–103].
- Nagy, Soper [104, 105].

MC@NLO is the only publicly available program that combines NLO calculations with parton showering and hadronization. The HERWIG Monte Carlo is used for the latter. The use of a different Monte Carlo, such as PYTHIA, would require a different subtraction scheme for the NLO matrix elements. The processes included to date are $(W, Z, \gamma^*, H, b\bar{b}, t\bar{t}, HW, HZ, WW, WZ, ZZ)$. Recently, single top hadroproduction has been added to MC@NLO [106]. This is the first implementation of a process that has both initial- and final-state singularities. This allows a more general category of additional processes to be added in the future. Work is proceeding on the addition of inclusive jet production and the production of a Higgs boson via WW fusion. Adding spin correlations to a process increases the level of difficulty but is important for processes such as single top production.

If, in addition, the CKKW formalism could be used for the description of hard parton emissions, the utility and accuracy of a NLO Monte Carlo could be greatly increased. The merger of these two techniques should be possible in Monte Carlos available by the time of the LHC turn-on.

4. Parton distribution functions

4.1. Introduction

As mentioned in section 2, the calculation of the production cross sections at hadron colliders for both interesting physics processes and their backgrounds relies upon a knowledge of the distribution of the momentum fraction x of the partons (quarks and gluons) in a proton in the relevant kinematic range. These parton distribution functions (pdfs) cannot be calculated perturbatively but rather are determined by global fits to data from deep-inelastic scattering (DIS), Drell–Yan (DY) and jet production at current energy ranges. Two major groups, CTEQ [11] and MRST [10], provide semi-regular updates to the parton distributions when new data and/or theoretical developments become available. In addition, there are also pdfs available from Alekhin [107] and from the two HERA experiments [108–111]. The newest pdfs, in most cases, provide the most accurate description of the world's data and should be utilized in preference to older pdf sets.

4.2. Processes involved in global analysis fits

Measurements of deep-inelastic scattering (DIS) structure functions (F_2, F_3) in lepton–hadron scattering and of lepton pair production cross sections in hadron–hadron collisions provide the main source of information on quark distributions $f_{q/p}(x, Q^2)$ inside hadrons. At leading order, the gluon distribution function $f_{g/p}(x, Q^2)$ enters directly in hadron–hadron scattering processes with jet final states. Modern global parton distribution fits are carried out to NLO and in some cases to NNLO, which allow $\alpha_S(Q^2)$, $f_{q/p}(x, Q^2)$ and $f_{g/p}(x, Q^2)$ to all mix and contribute in the theoretical formulae for all processes. Nevertheless, the broad picture described above still holds to some degree in global pdf analyses.

The data from DIS, DY and jet processes utilized in pdf fits cover a wide range in x and Q^2. HERA data (H1 [54]+ZEUS [55]) are predominantly at low x, while the fixed-target DIS [57–61] and DY [56, 62] data are at higher x. Collider jet data [63, 64] cover a broad range in x and Q^2 by themselves and are particularly important in the determination of the high x gluon distribution. There is considerable overlap, however, among the datasets with the degree of overlap increasing with time as the statistics of the HERA experiments increase. Parton distributions determined at a given x and Q^2 'feed-down' or evolve to lower x values at higher Q^2 values. DGLAP-based NLO (and NNLO) pQCD should provide an accurate description of the data (and of the evolution of the parton distributions) over the entire kinematic range present in current global fits. At very low x and Q, DGLAP evolution is believed to be no longer applicable and a BFKL [174–177] description must be used. No clear evidence of BFKL physics is seen in the current range of data; thus all global analyses use conventional DGLAP evolution of pdfs.

Many processes have been calculated to NLO and there is the possibility of including data from these processes in global fits. For example, the rapidity distributions for W^+, W^- and Z production at the Tevatron and LHC should prove to be very useful in constraining u and d valence and sea quarks.

There is a remarkable consistency between the data in the pdf fits and the perturbative QCD theory fit to them. Both the CTEQ and MRST groups use over 2000 data points in their global pdf analyses and the χ^2/DOF for the fit of theory to data is on the order of unity. For most of the data points, the statistical errors are smaller than the systematic errors, so a proper treatment of the systematic errors and their bin-to-bin correlations is important.

The accuracy of the extrapolation to higher Q^2 depends on the accuracy of the original measurement, any uncertainty on $\alpha_S(Q^2)$ and the accuracy of the evolution code. Most global pdf analyses are carried out at NLO; recently, the DGLAP evolution kernels have been calculated at NNLO [112], allowing a full NNLO evolution to be carried out, and NNLO pdfs calculated in this manner are available [107, 113]. However, not all processes in the global fits, and specifically inclusive jet production, are available at NNLO. Thus, any current NNLO global pdf analyses are still approximate for this reason, but in practice the approximation should work well. Current programs in use by CTEQ and MRST should be able to carry out the evolution using NLO DGLAP to an accuracy of a few per cent over the hadron collider kinematic range, except perhaps at very large x and very small x. (See the discussion in section 6 regarding the validity of NLO analysis at the LHC.) The kinematics appropriate for the production of a state of mass M and rapidity y at the LHC was shown in figure 3 in section 2. For example, to produce a state of mass 100 GeV and rapidity 2 requires partons of x values 0.05 and 0.001 at a Q^2 value of 1×10^4 GeV^2. Also shown in the figure is a view of the kinematic coverage of the fixed-target and HERA experiments used in the global pdf fits.

4.3. Parametrizations and schemes

A global pdf analysis carried out at next-to-leading order needs to be performed in a specific renormalization and factorization scheme. The evolution kernels are calculated in a specific scheme and to maintain consistency, any hard-scattering cross section calculations used for the input processes or utilizing the resulting pdfs need to have been implemented in that same renormalization scheme. Almost universally, the $\overline{\text{MS}}$ scheme is used; pdfs are also available in the DIS scheme, a fixed flavour scheme (see, for example, GRV [114]) and several schemes that differ in their specific treatment of the charm quark mass.

It is also possible to use only leading-order matrix element calculations in the global fits which result in leading-order parton distribution functions, which have been made available
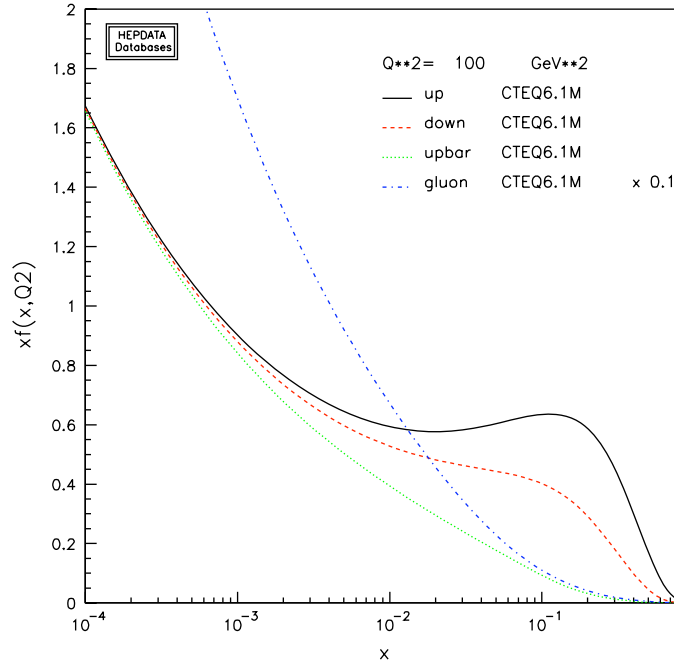
Figure 27. The CTEQ6.1 parton distribution functions evaluated at a Q of 10 GeV.

by both the CTEQ and MRST groups. For many hard matrix elements for processes used in the global analysis, there exist K factors significantly different from unity. Thus, one expects there to be noticeable differences between the LO and NLO parton distributions.

All global analyses use a generic form for the parametrization of both the quark and gluon distributions at some reference value Q_0:

$$F(x, Q_0) = A_0 x^{A_1} (1 - x)^{A_2} P(x; A_3, ...).\tag{42}$$

The reference value Q_0 is usually chosen in the range 1–2 GeV. The parameter A_1 is associated with small-x Regge behaviour while A_2 is associated with large-x valence counting rules.

The first two factors, in general, are not sufficient to describe either quark or gluon distributions. The term $P(x; A_3, ...)$ is a suitably chosen smooth function, depending on one or more parameters, that adds more flexibility to the pdf parametrization. In general, both the number of free parameters and the functional form can have an influence on the global fit. The pdfs made available to the world from the global analysis groups can either be in a form where the x and Q^2 dependence is parametrized or the pdfs for a given x and Q^2 range can be interpolated from a grid that is provided or the grid can be generated given the starting parameters for the pdfs (see the discussion on LHAPDF in section 4.7). All techniques should provide an accuracy on the output pdf distributions on the order of a few per cent.

The parton distributions from the CTEQ6.1 pdfs release are plotted in figure 27 at a Q value of 10 GeV. The gluon distribution is dominant at x values of less than 0.01 with the valence quark distributions dominant at higher x. One of the major influences of the HERA data has been to steepen the gluon distribution at low x.

4.4. Uncertainties on pdfs

In addition to having the best estimates for the values of the pdfs in a given kinematic range, it is also important to understand the allowed range of variation of the pdfs, i.e. their uncertainties. A conventional method of estimating parton distribution uncertainties has been to compare different published parton distributions. This is unreliable since most published sets of parton distributions (for example from CTEQ and MRST) adopt similar assumptions and the differences between the sets do not fully explore the uncertainties that actually exist.

The sum of the quark distributions $(\Sigma f_{q/p}(x, Q^2) + f_{g/p}(x, Q^2))$ is, in general, well determined over a wide range of x and Q^2. As stated above, the quark distributions are predominantly determined by the DIS and DY data sets which have large statistics and systematic errors in the few per cent range ($\pm 3\%$ for $10^{-4} < x < 0.75$). Thus the sum of the quark distributions is basically known to a similar accuracy. The individual quark flavours, though, may have a greater uncertainty than the sum. This can be important, for example, in predicting distributions that depend on specific quark flavours, such as the W asymmetry distribution [115] and the W and Z rapidity distributions.

However, the largest uncertainty of any parton distribution is that on the gluon distribution. The gluon distribution can be determined indirectly at low x by measuring the scaling violations in the quark distributions, but a direct measurement is necessary at moderate to high x. The best direct information on the gluon distribution at moderate to high x comes from jet production at the Tevatron.

There has been a great deal of recent activity on the subject of pdf uncertainties. Two techniques in particular, the Lagrange Multiplier and Hessian techniques, have been used by CTEQ and MRST to estimate pdf uncertainties [116–118]. The Lagrange Multiplier technique is useful for probing the pdf uncertainty of a given process, such as the W cross section, while the Hessian technique provides a more general framework for estimating the pdf uncertainty for any cross section. In addition, the Hessian technique results in tools more accessible to the general user.

In the Hessian method a large matrix (20×20 for CTEQ, 15×15 for MRST), with dimension equal to the number of free parameters in the fit, has to be diagonalized. The result is 20 (15) orthonormal eigenvector directions for CTEQ (MRST) which provide the basis for the determination of the pdf error for any cross section. This process is shown schematically in figure 28. The eigenvectors are now admixtures of the 20 pdf parameters left free in the global fit. There is a broad range for the eigenvalues, over a factor of one million. The eigenvalues are distributed roughly linearly as $\log \epsilon_i$, where ϵ_i is the eigenvalue for the ith direction. The larger eigenvalues correspond to directions which are well determined; for example, eigenvectors 1 and 2 are sensitive primarily to the valence quark distributions at moderate x, a region where they are well constrained. The theoretical uncertainty on the determination of the W mass at both the Tevatron and the LHC depends primarily on these 2 eigenvector directions, as W production at the Tevatron proceeds primarily through collisions of valence quarks. The most significant eigenvector directions for determination of the W mass at the LHC correspond to larger eigenvector numbers, which are primarily determined by sea quark distributions. In most cases, the eigenvector cannot be directly tied to the behaviour of a particular pdf in a specific kinematic region. A longer discussion of the meaning of the eigenvectors for the CTEQ6.1 pdf analysis can be found at the benchmark website.

There are two things that can happen when new pdfs (eigenvector directions) are added: a new direction in parameter space can be opened to which some cross sections will be sensitive (such as eigenvector 15 in the CTEQ6.1 error pdf set which is sensitive to the high x gluon behaviour and thus influences the high p_T jet cross section at the Tevatron). In this case,

2-dim (i,j) rendition of d-dim (~16) PDF parameter space

contours of constant χ^2_{global}

$\mathbf{u}_i$: *eigenvector in the l-direction*

$\mathbf{p}(i)$: *point of largest a_i with tolerance T*

$\mathbf{s}_0$: *global minimum*

diagonalization and

rescaling by

the iterative method

• *Hessian eigenvector basis sets*

(a)

Original parameter basis

(b)

Orthonormal eigenvector basis
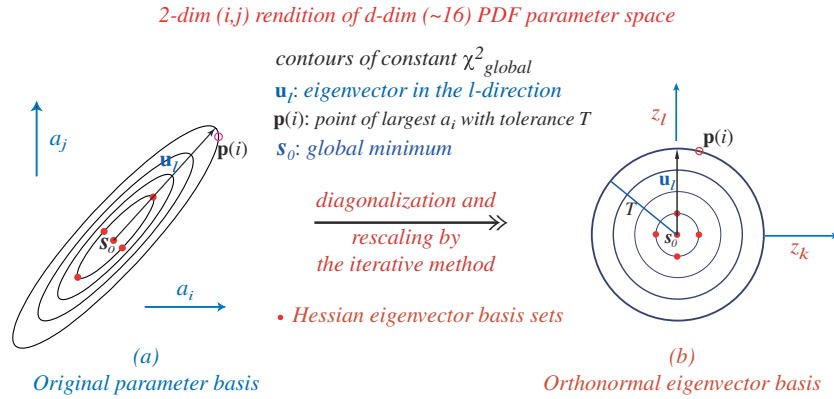
Figure 28. A schematic representation of the transformation from the pdf parameter basis to the orthonormal eigenvector basis.
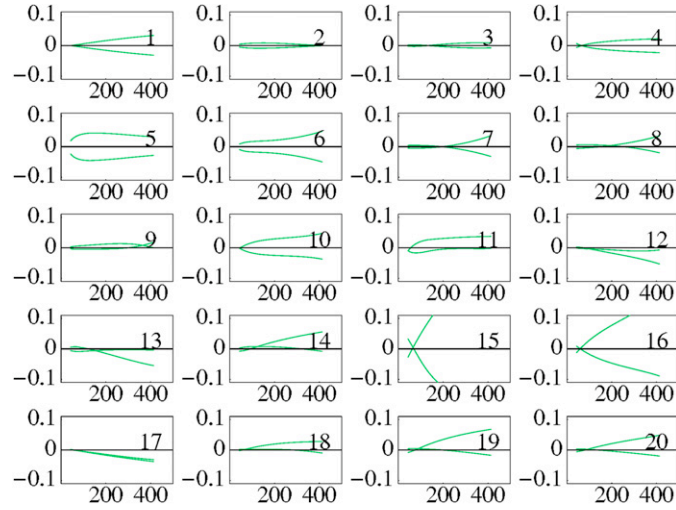
Figure 29. The pdf errors for the CDF inclusive jet cross section in Run 1 for the 20 different eigenvector directions. The vertical axes show the fractional deviation from the central prediction and the horizontal axes the jet transverse momentum in GeV.

a smaller parameter space is an underestimate of the true pdf error since it did not sample a direction important for some physics. In the second case, adding new eigenvectors does not appreciably open new parameter space and the new parameters should not contribute much pdf error to most physics processes (although the error may be redistributed somewhat among the new and old eigenvectors).

Each error pdf results from an excursion along the '+' and '−' directions for each eigenvector. The excursions are symmetric for the larger eigenvalues but may be asymmetric for the more poorly determined directions. There are 40 pdfs for the CTEQ6.1 error set and 30 for the MRST error set. In figure 29, the pdf errors are shown in the '+' and '−' directions for the 20 CTEQ eigenvector directions for predictions for inclusive jet production at the Tevatron. The excursions are symmetric for the first 10 eigenvectors but can be asymmetric for the last 10.

Consider a variable X; its value using the central pdf for an error set (say CTEQ6.1M) is given by X_0. X_i^+ is the value of that variable using the pdf corresponding to the '+' direction for eigenvector i and X_i^- the value for the variable using the pdf corresponding to the '−' direction. In order to calculate the pdf error for an observable, a *Master Equation* should be used:

$$\Delta X_{\max}^+ = \sqrt{\sum_{i=1}^{N} [\max(X_i^+ - X_0, X_i^- - X_0, 0)]^2},$$

$$\Delta X_{\max}^- = \sqrt{\sum_{i=1}^{N} [\max(X_0 - X_i^+, X_0 - X_i^-, 0)]^2}. \tag{43}$$

ΔX^+ adds in quadrature the pdf error contributions that lead to an increase in the observable X and ΔX^- the pdf error contributions that lead to a decrease. The addition in quadrature is justified by the eigenvectors forming an orthonormal basis. The sum is over all N eigenvector directions or 20 in the case of CTEQ6.1. Ordinarily, $X_i^+ - X_0$ will be positive and $X_i^- - X_0$ will be negative, and thus it is trivial as to which term is to be included in each quadratic sum. For the higher number eigenvectors, however, we have seen that the '+' and '−' contributions may be in the same direction (see for example eigenvector 17 in figure 29). In this case, only the most positive term will be included in the calculation of ΔX^+ and the most negative in the calculation of ΔX^-. Thus, there may be less than N terms for either the '+' or '−' directions. There are other versions of the *Master Equation* in current use but the version listed above is the 'official' recommendation of the authors. Either X_0 and $X_i^\pm$ can be calculated separately in a matrix element/Monte Carlo program (requiring the program to be run $2N + 1$ times) or X_0 can be calculated with the program and at the same time the ratio of the pdf luminosities (the product of the two pdfs at the x values used in the generation of the event) for eigenvector i ($\pm$) to that of the central fit can be calculated and stored. This results in an effective sample with $2N + 1$ weights, but identical kinematics, requiring a substantially reduced amount of time to generate.

Perhaps the most controversial aspect of pdf uncertainties is the determination of the $\Delta \chi^2$ excursion from the central fit that is representative of a reasonable error. CTEQ chooses a $\Delta \chi^2$ value of 100 (corresponding to a 90% CL limit) while MRST uses a value of 50. Thus, in general, the pdf uncertainties for any cross section will be larger for the CTEQ set than for the MRST set. The difference in the criterion indicates the difficulty of treating the error analysis for such a large disparate sample of data in a statistically rigorous and unique manner. But in any case, both groups are in agreement that a χ^2 excursion of 1 (for a 1σ error) is too low of a value in a global pdf fit. The global fits use data sets arising from a number of different processes and different experiments; there is a non-negligible tension between some of the different data sets. pdf fits performed within a single experiment or with a single data type may be able to set tighter tolerances. The uncertainties for all predictions should be linearly dependent on the tolerance parameter used; thus, it should be reasonable to scale the uncertainty for an observable from the 90% CL limit provided by the CTEQ/MRST error pdfs to a one-sigma error by dividing by a factor of 1.6. Such a scaling will be a better approximation for observables more dependent on the low number eigenvectors, where the χ^2 function is closer to a quadratic form. Note that such a scaling may result in an underestimate of the *true* pdf uncertainty, as the central results for CTEQ and MRST often differ by an amount similar to this one-sigma error. (See the discussion in section 2.2 regarding the W cross section predictions at the Tevatron.)
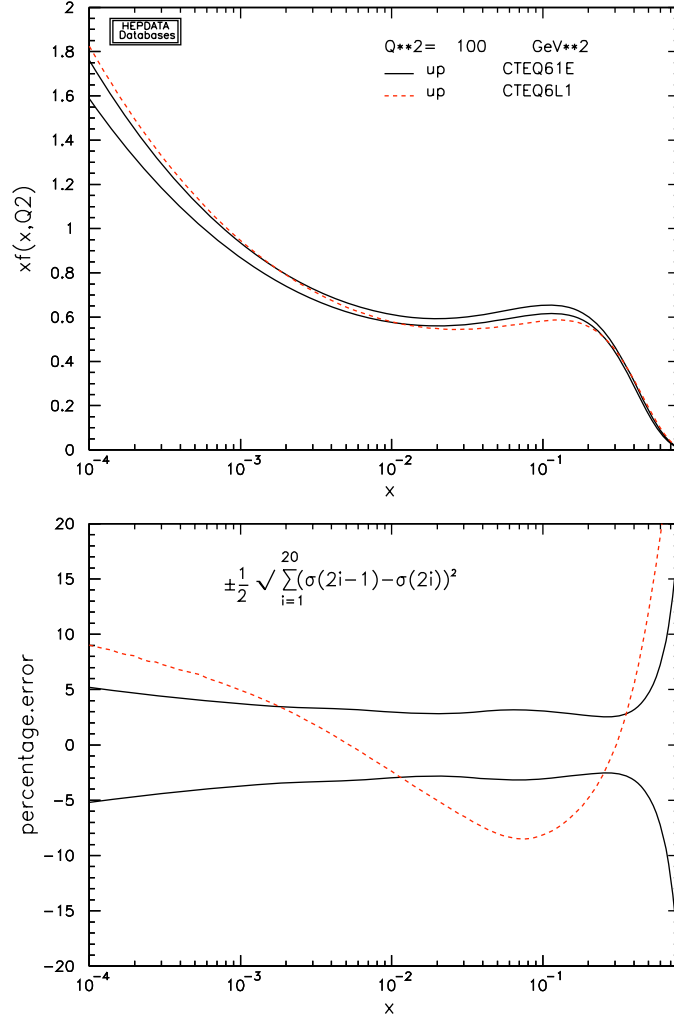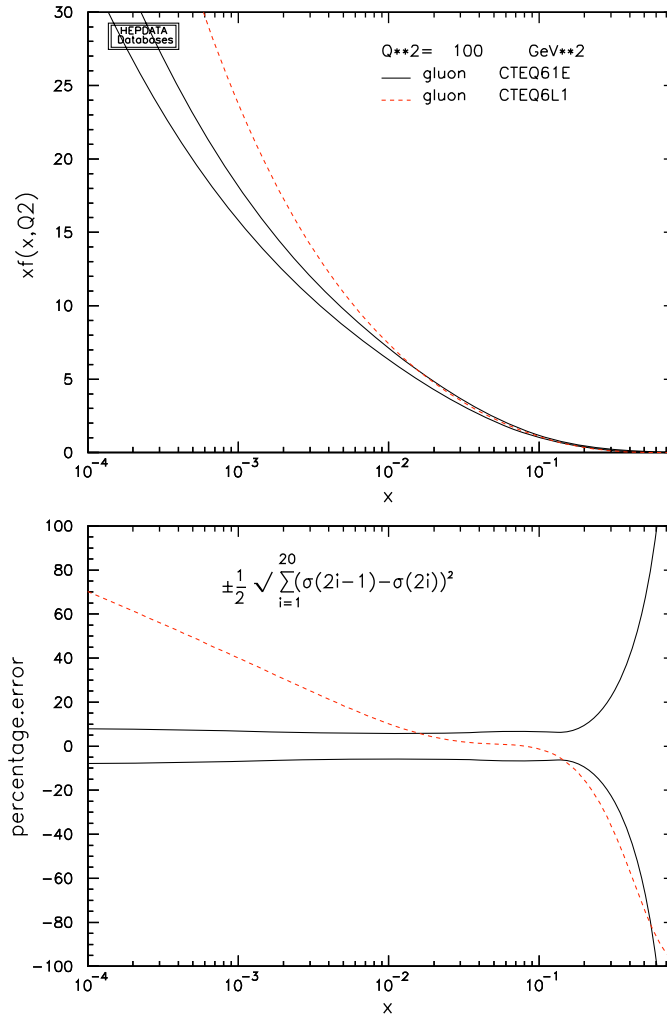
Figure 30. The pdf uncertainty for the up quark distribution from the CTEQ6.1 pdf set and a comparison to the CTEQ6L1 up quark distribution.

The CTEQ and MRST uncertainties for the up quark and gluon distributions are shown in figures 30–33. The pdf luminosity uncertainties for various pdf combinations for some kinematic situations appropriate to the LHC will be discussed in section 6.

Both the CTEQ and MRST groups typically use a fixed value of $\alpha_S(M_Z^2)$ equal to the PDG world average [119] in their global fits. An additional uncertainty in the determination of pdfs results from the uncertainty in the value of $\alpha_S(M_Z^2)$ used in the global fits. Figures 34 and 35 show the results of varying the value of α_S on the up quark and gluon distributions [120]. As expected, the gluon distribution has a greater sensitivity on α_S due to the coupling mentioned earlier.

4.5. NLO and LO pdfs

In the past, the global pdf fitting groups have produced sets of pdfs in which leading order rather than next-to-leading order matrix elements, along with the 1-loop α_S rather than the

Figure 31. The pdf uncertainty for the gluon distribution from the CTEQ6.1 pdf set and a comparison to the CTEQ6L1 gluon distribution.

2-loop α_S, have been used to fit the input datasets. The resultant leading-order pdfs have most often been used in conjunction with leading-order matrix element programs or parton shower Monte Carlos. However, the leading-order pdfs of a given set will tend to differ from the central pdfs in the NLO fit, and in fact will most often lie outside the pdf error band. Such is the case for the up quark distribution shown in figures 30 and 32 and the gluon distribution shown in figures 31 and 33, where the LO pdfs are plotted along with the NLO pdf error bands.

The global pdf fits are dominated by the high statistics, low systematic error deep-inelastic scattering data and the differences between the LO and NLO pdfs are determined most often by the differences between the LO and NLO matrix elements for deep-inelastic scattering. As the NLO corrections for most processes of interest at the LHC are reasonably small, the use of NLO pdfs in conjunction with LO matrix elements will most often give a closer approximation of the full NLO result (although the result remains formally LO). In many cases in which a
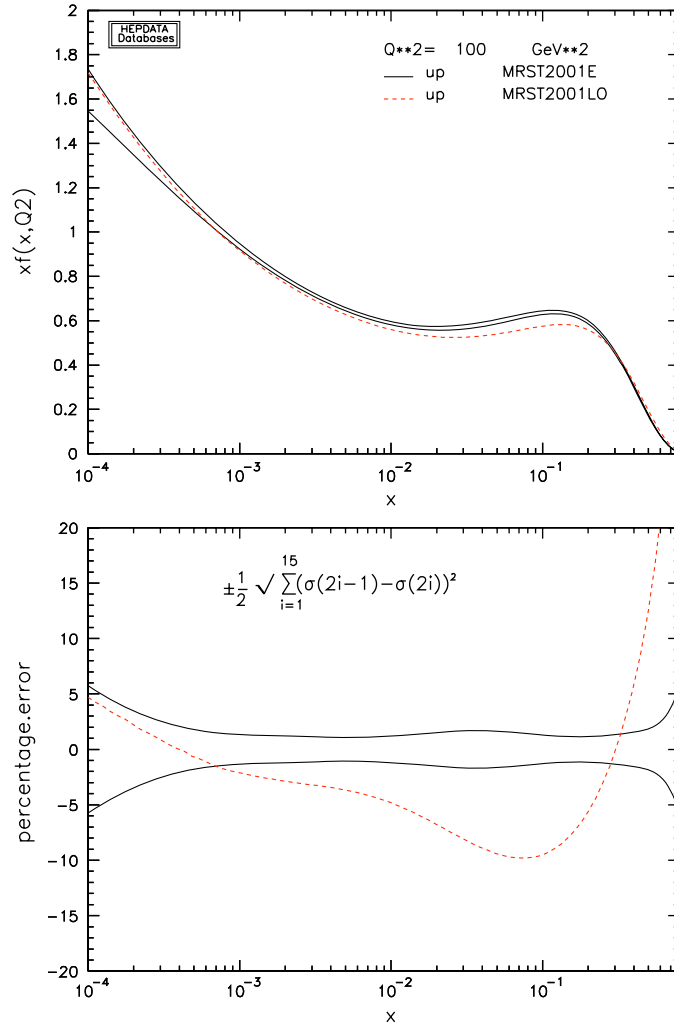
Figure 32. The pdf uncertainty for the up quark distribution from the MRST2001 pdf set and a comparison to the MRST2001LO up quark distribution.

relatively large K-factor results from a calculation of collider processes, the primary cause is the difference between LO and NLO pdfs, rather than the differences between LO and NLO matrix elements.

In addition, it is often useful to examine variations in acceptances in Monte Carlos using the families of NLO error pdfs; thus, it is important to also compare with the predictions using the central (NLO) pdf. It is our recommendation, then, that NLO pdfs be used for predictions at the LHC, even with LO matrix element programs and parton shower Monte Carlos. There are two consequences: (1) the pdfs must be positive-definite in the kinematic regions of interest as they will be used to develop the initial-state showering history and (2) underlying event tunes must be available using the NLO pdfs. An underlying event model that uses multiple-parton interactions depends strongly on the slope of the low x gluon distribution. The NLO gluon distribution tends to have a much shallower slope than does the LO gluon and thus a different set
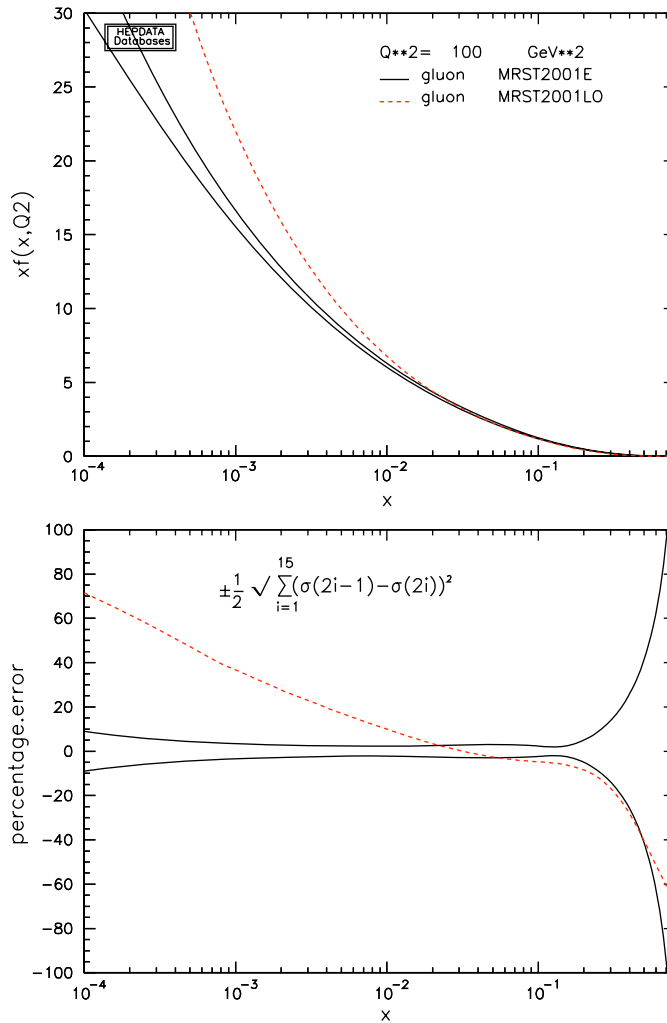
Figure 33. The pdf uncertainty for the gluon distribution from the MRST2001 pdf set and a comparison to the MRST2001LO gluon distribution.

of parameters will be needed for the tune[12]. A NLO tune is currently available for PYTHIA using the (NLO) CTEQ6.1 pdfs that is equivalent to Tune A (see section 5.2), which uses CTEQ5L. An equivalent tune for HERWIG (with Jimmy) is also available [93]. At the end of the day, though, the accuracy of the LO prediction is still only LO[13].

The transition from NLO to NNLO results in much smaller changes to the pdfs as can be observed in figure 36.

---

[12] The low x behaviour for the 40 CTEQ6.1 error pdfs are similar enough to that of the central CTEQ6.1 pdf that the same underlying event tune will work for all.

[13] It has been pointed out in [121] that $\overline{MS}$ pdfs are appropriate for calculations of inclusive cross sections but are not suitable for the exclusive predictions inherent in Monte Carlo event generators. It is in principle necessary to define pdfs specific to the parton showering algorithm for each Monte Carlo. However, the error introduced by using $\overline{MS}$ pdfs with leading-order parton shower Monte Carlos should be of a higher logarithmic order than the accuracy we are seeking.
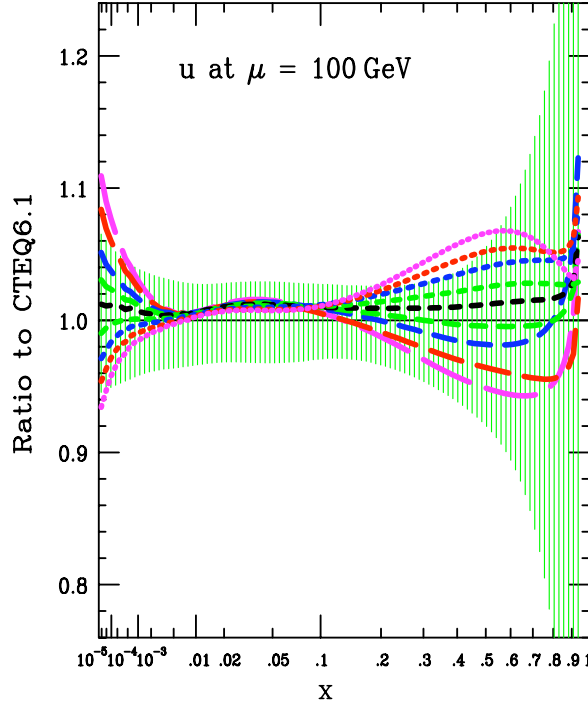
Figure 34. Variation of the up quark distribution for different values of α_S. α_S varies from 0.110 (short-dash) to 0.124 (long-dash) in increments of 0.002.

4.6. Pdf uncertainties and Sudakov form factors

As discussed in the above section, it is often useful to use the error pdf sets with parton shower Monte Carlos. The caveat still remains that a true test of the acceptances would use a NLO MC. Similar to their use with matrix element calculations, events can be generated once using the central pdf and the pdf weights stored for the error pdfs. These pdf weights then can be used to construct the pdf uncertainty for any observable. The sample code for PYTHIA is given on the benchmark website. One additional complication with respect to their use in matrix element programs is that the parton distributions are used to construct the initial-state parton showers through the backward evolution process. The space-like evolution of the initial-state partons is guided by the ratio of parton distribution functions at different x and Q^2 values, cf (41). Thus the Sudakov form factors in parton shower Monte Carlos will be constructed using only the central pdf and not any of the individual error pdfs and this may lead to some errors for the calculation of the pdf uncertainties of some observables. However, it was demonstrated in [86] that the pdf uncertainty for Sudakov form factors in the kinematic region relevant for the LHC is minimal, and the weighting technique can be used just as well with parton shower Monte Carlos as with matrix element programs.

4.7. LHAPDF

Libraries such as PDFLIB [122] have been established that maintain a large collection of available pdfs. However, the PDFLIB is no longer supported, making it more difficult for easy access to the most up-to-date pdfs. In addition, the determination of the pdf uncertainty of any
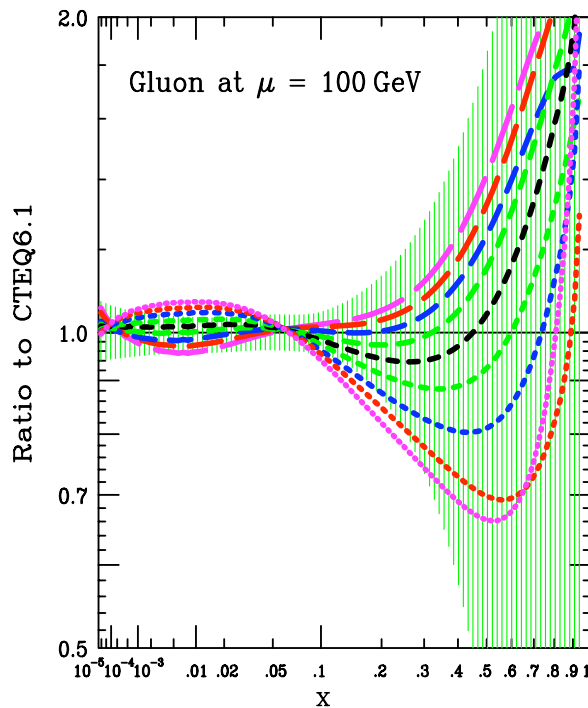
Figure 35. Variation of the gluon distribution for different values of α_S. α_S varies from 0.110 (short-dash) to 0.124 (long-dash) in increments of 0.002.

cross section typically involves the use of a large number of pdfs (on the order of 30–100) and the PDFLIB is not set up for easy accessibility for a large number of pdfs.

At Les Houches in 2001, representatives from a number of pdf groups were present and an interface (Les Houches Accord 2, or LHAPDF) [124] that allows the compact storage of the information needed to define a pdf was defined. Each pdf can be determined either from a grid in x and Q^2 or by a few lines of information (basically the starting values of the parameters at $Q = Q_o$) and the interface carries out the evolution to any x and Q value, at either LO or NLO as appropriate for each pdf.

The interface is as easy to use as PDFLIB and consists essentially of 3 subroutine calls:

- call Initpdfset(*name*): called once at the beginning of the code; *name* is the file name of the external pdf file that defines the pdf set (for example, CTEQ, GKK [123] or MRST);
- call Initpdf(*mem*): *mem* specifies the individual member of the pdf set; and
- call evolvepdf(*x,Q,f*): returns the pdf momentum densities for flavour f at a momentum fraction x and scale Q.

Responsibility for LHAPDF has been taken over by the Durham HEPDATA project [125] and regular updates/improvements have been produced. It is currently included in the matrix element program MCFM [126] and will be included in future versions of other matrix element and parton shower Monte Carlo programs. Recent modifications make it possible to include all error pdfs in memory at the same time. Such a possibility reduces the amount of time needed for pdf error calculations on any observable. The matrix element result can be calculated once using the central pdf and the relative (pdf)×(pdf) parton–parton luminosity can be calculated for each of the error pdfs (or the values of x_1,x_2, the flavour of partons
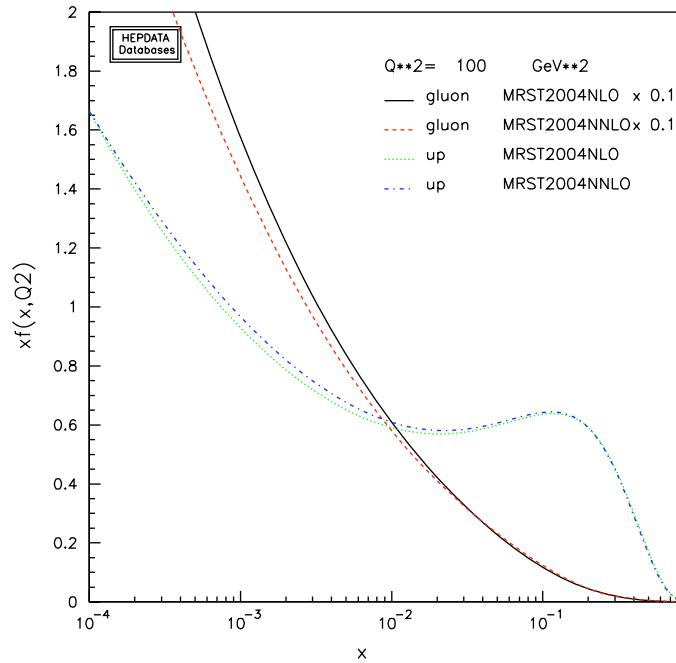
Figure 36. A comparison of the NLO and NNLO gluon and up quark distributions for the MRST2004 sets of pdfs.

1 and 2 and the value of Q^2 can be stored). Such a pdf re-weighting has been shown to work both for exact matrix element calculations as well as for matrix element+parton shower calculations. In addition, a new routine LHAGLUE [125] provides an interface from PDFLIB to LHAPDF making it possible to use the PDFLIB subroutine calls that may be present in older programs.

5. Comparisons with Tevatron data

5.1. W/Z production

As discussed earlier, W production at hadron–hadron colliders serves as a precision benchmark for Standard Model physics. Experimentally, the systematic errors are small. The decay leptons are easy to trigger on and the backgrounds are under good control. Theoretically, the cross section and rapidity distributions are known to NNLO. The W and Z cross sections measured at the Tevatron are shown in figure 37 for both Run 1 and Run 2 [12]. The experimental cross sections agree well with the predictions and the Run 2 cross sections show the rise expected from the increase in centre-of-mass energy over Run 1. In figure 4 in section 2, the Run 2 cross sections from CDF and D0 are compared with predictions at LO, NLO and NNLO. The NNLO predictions are a few per cent larger than the NLO predictions. Good agreement is observed with both. It is noteworthy that the largest experimental uncertainty for the W and Z cross sections is the uncertainty in the luminosity, typically on the order of 5%. The theoretical systematic errors are primarily from the pdf uncertainty. If other Tevatron cross sections were normalized to the W cross section, then both the theoretical and experimental systematic errors for those cross sections could be reduced.
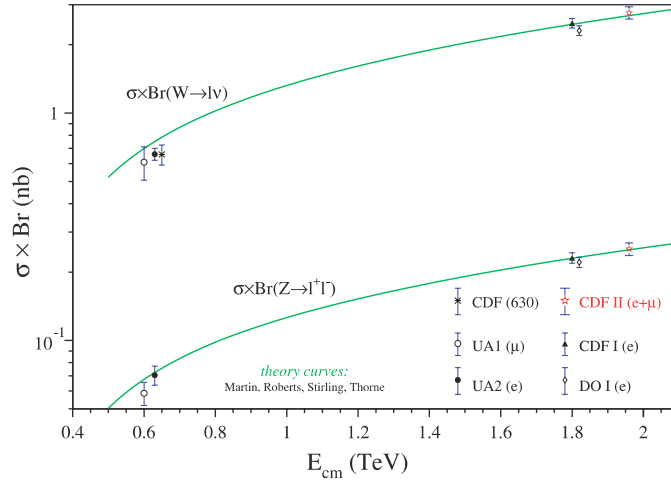
Figure 37. *W* and *Z* cross sections as a function of the centre-of-mass energy.
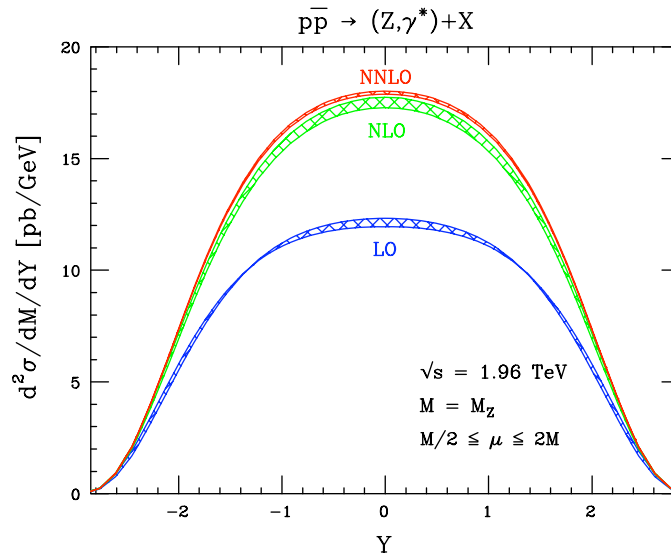
Figure 38. Predictions for the rapidity distribution of an on-shell *Z* boson in Run 2 at the Tevatron at LO, NLO and NNLO. The bands indicate the variation of the renormalization and factorization scales within the range $M_Z/2$ to $2M_Z$.

Predictions of the rapidity distribution for Z ($\rightarrow e^+e^-$) production at the Tevatron are shown in figure 38 [68, 129]. There is a shape change in going from LO to NLO, as well as an increase in normalization, while the transition from NLO to NNLO is essentially just a small K-factor with little change in shape. The Z rapidity distribution measured by D0 in Run 2 is shown in figure 39 [13]; the measurement agrees with the NNLO prediction over the entire rapidity range. Such cross sections may be useful as input to global pdf fits in the near future.

The transverse momentum distribution for Z bosons at the Tevatron (CDF Run 1) is shown in figures 40 (low p_T) and 41 (all p_T) along with comparisons to the parton showers PYTHIA and ResBos which are discussed in section 3.5. The ResBos predictions agree well with the
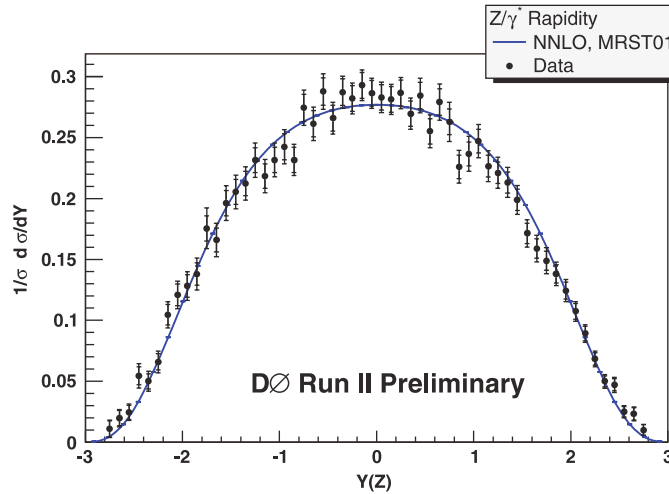
Figure 39. Z rapidity distribution from D0 in Run 2.
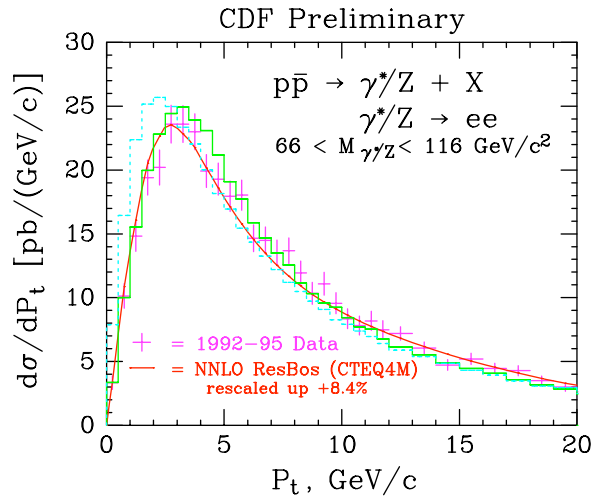
Figure 40. The transverse momentum distribution (low p_T) for $Z \to e^+e^-$ from CDF in Run 1, along with comparisons to predictions from PYTHIA and ResBos. The dashed blue curve is the default PYTHIA prediction. The PYTHIA solid-green curve has had an additional 2 GeV of k_T added to the parton shower.

data over the entire kinematic region, while the PYTHIA predictions require the addition of an intrinsic k_T of approximately 2 GeV for best agreement at lower transverse momentum. This intrinsic k_T is not totally due to the finite size of the proton; it mostly results from the finite cutoff in the parton shower evolution and the need to add the missing component back 'by-hand'. ResBos correctly describes the non-perturbative as well as the perturbative region.

The average transverse momentum for Drell–Yan production has been measured as a function of the Drell–Yan pair mass in CDF in Run 2. This is shown in figure 42 [127]. The average transverse momentum (neglecting the high p_T tail) increases roughly logarithmically with the square of the Drell–Yan mass. The data agree well with the default PYTHIA 6.2
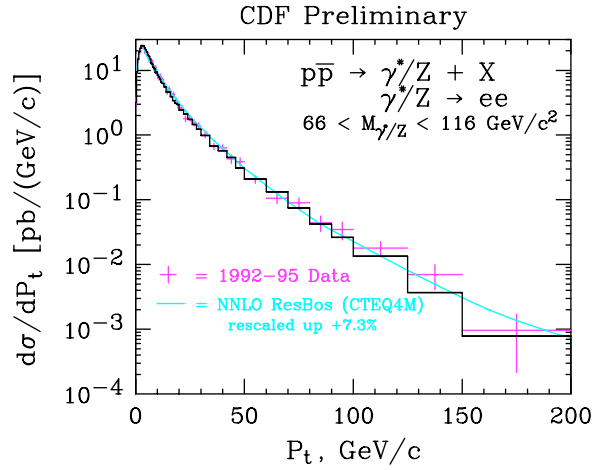
Figure 41. The transverse momentum distribution (full p_T range) for $Z \to e^+e^-$ from CDF in Run 1, along with comparisons to predictions from PYTHIA (solid histogram) and ResBos.
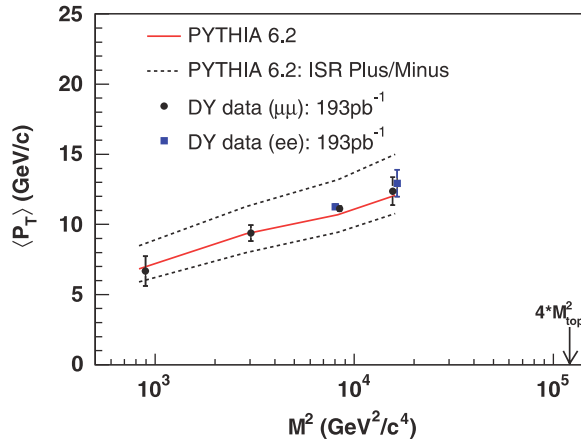
Figure 42. The average transverse momentum for Drell–Yan pairs from CDF in Run 2, along with comparisons to predictions from PYTHIA.

prediction using Tune A. Also shown are two predictions involving tunes of PYTHIA that give larger/smaller values for the average Drell–Yan transverse momentum as a function of the Drell–Yan mass. The *Plus/Minus* tunes were used to estimate the initial-state-radiation uncertainty for the determination of the top mass in CDF. Most of the $t\bar{t}$ cross section at the Tevatron arises from $q\bar{q}$ initial-states, so the Drell–Yan measurements serve as a good model. (See further discussion in section 5.5.) The information regarding these tunes is available on the benchmarks website.

5.2. Underlying event

What is meant by a 'minimum bias event' is somewhat murky, and the exact definition will depend on the trigger of each experiment. The description of the underlying event energy and of minimum bias events requires a non-perturbative and/or semi-perturbative phenomenological

model. There are currently a number of models available, primarily inside parton shower Monte Carlo programs, to predict both of these processes. We discuss several of the popular models below. An understanding of this soft physics is interesting in its own right but is also essential for precision measurements of hard interactions where the soft physics effects need to be subtracted.

Perhaps the simplest model for the underlying event is the uncorrelated soft scattering model present in HERWIG. Basically, the model is a parametrization of the minimum bias data taken by the UA5 experiment [128] at the CERN $p\bar{p}$ Collider. The model tends to predict underlying event distributions softer than those measured at the Tevatron and has a questionable extrapolation to higher centre-of-mass energies. A newer model for the underlying event in HERWIG is termed 'Jimmy'[14] and describes the underlying event in terms of multiple-parton interactions at a scale lower than the hard scale and with the number of such parton scatterings depending on the impact parameter overlap of the two colliding hadrons.

The PYTHIA model for the underlying event also utilizes a multiple-parton interaction framework with the total rate for parton–parton interactions assumed to be given by perturbative QCD. A cutoff, p_{Tmin}, is introduced to regularize the divergence as the transverse momentum of the scattering goes to zero. The rate for multiple-parton interactions depends strongly on the value of the gluon distribution at low x. The cutoff, p_{Tmin}, is the main free parameter of the model and basically corresponds to an inverse colour screening distance. A tuning of the PYTHIA underlying event parameters (Tune A) basically succeeds in describing most of the global event properties in events at the Tevatron. With the new version of PYTHIA (version 6.4) [85, 16], a new model for the underlying event is available, similar in spirit to the old multiple-parton interaction model, but with a more sophisticated treatment of colour, flavour and momentum correlations in the remnants.

5.3. Inclusive jet production

It is useful to consider the measurement of inclusive jet production at the Tevatron as (1) it probes the highest transverse momentum range accessible at the Tevatron, (2) it has a large impact on global pdf analyses and (3) many of the subtleties regarding measurements with jets in the final state and the use of jet algorithms come into play.

As shown in figure 43, a dijet event at a hadron–hadron collider consists of a hard collision of two incoming partons (with possible gluon radiation from both the incoming and outgoing legs) along with softer interactions from the remaining partons in the colliding hadrons ('the underlying event energy').

The inclusive jet cross section measured by the CDF Collaboration in Run 2 is shown in figure 44, as a function of the jet transverse momentum [130]. Due to the higher statistics compared with Run 1, and the higher centre-of-mass energy, the reach in transverse momentum has increased by approximately 150 GeV. The measurement uses the midpoint cone algorithm with a cone radius of 0.7. As discussed in section 3.6, the midpoint algorithm places additional seeds (directions for jet cones) between stable cones having a separation of less than twice the size of the clustering cones. The midpoint algorithm uses four-vector kinematics for clustering individual partons, particles or energies in calorimeter towers, and jets are described using rapidity (y) and transverse momentum (p_T)[15].

---

[14] http://hepforge.cedar.ac.uk/jimmy/

[15] Self-contained versions of the CDF midpoint cone algorithm, as well as the Run 1 cone algorithm JetClu, are available at the benchmark website, in both Fortran and C++ versions.
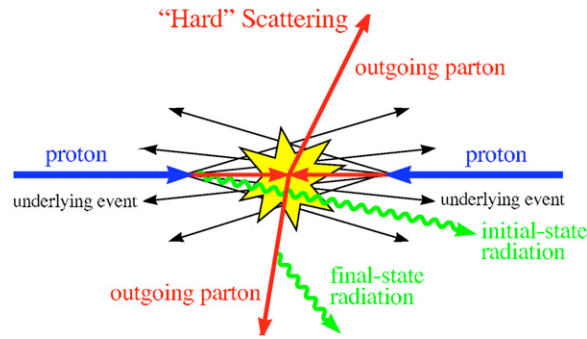
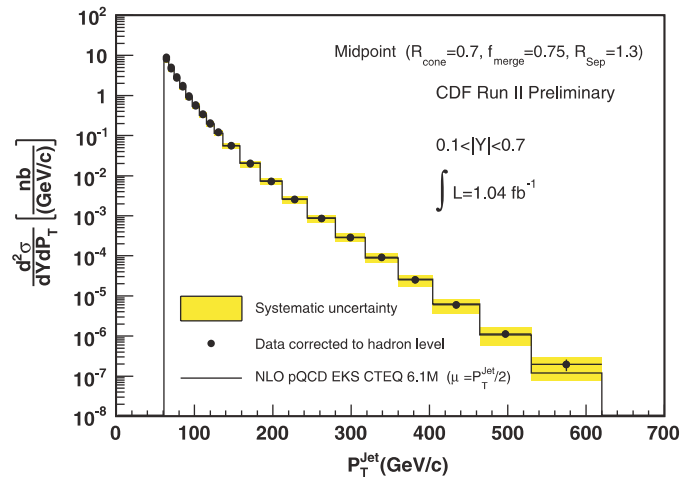**Figure 43.** Schematic cartoon of a 2 → 2 hard-scattering event.

Figure 44. The inclusive jet cross section from CDF in Run 2.

5.3.1. Corrections. For comparison of data to theory, the calorimeter tower energies clustered into a jet must first be corrected for the detector response. The calorimeters in the CDF experiment respond differently to electromagnetic showers than to hadronic showers, and the difference varies as a function of the transverse momentum of the jet. The detector response corrections are determined using a detector simulation in which the parameters have been tuned to test-beam and *in situ* calorimeter data. PYTHIA 6.216, with Tune A, is used for the production and fragmentation of jets. The same clustering procedure is applied to the final-state particles in PYTHIA as is done for the data. The correction is determined by matching the calorimeter jet to the corresponding particle jet. An additional correction accounts for the smearing effects due to the finite energy resolution of the calorimeter. At this point, the jet is said to be determined at the 'hadron level.'

For data to be compared to a parton level calculation, either the data must be corrected from the hadron level to the parton level or the theory must be corrected to the hadron level. Here we describe the former; the latter just involves the inverse corrections. It is our 'official recommendation' that, where possible, the data be presented at least at the hadron level, and the corrections between hadron and parton levels be clearly stated. The hadronization corrections consist of two components: the subtraction from the jet of the underlying event energy not
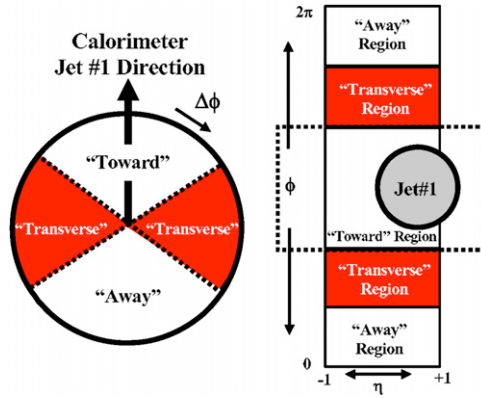
Figure 45. Definition of the 'toward', 'away' and 'transverse' regions.
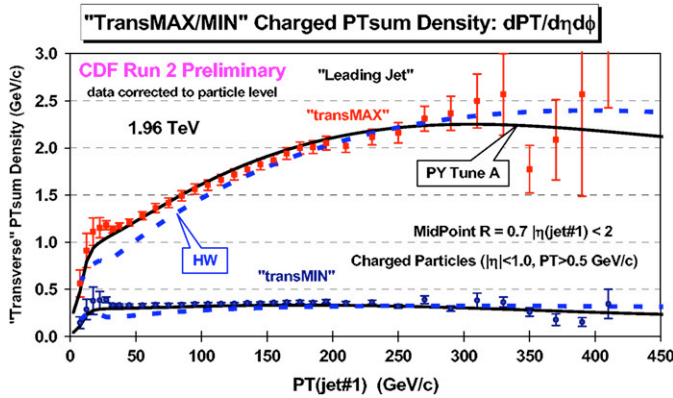
Figure 46. The sum of the transverse momenta of charged particles inside the TransMAX and TransMIN regions, as a function of the transverse momentum of the leading jet.

associated with the hard scattering and the correction for a loss of energy outside a jet due to the fragmentation process. The hadronization corrections can be calculated by comparing the results obtained from PYTHIA at the hadron level to the results from PYTHIA when the underlying event and the parton fragmentation into hadrons has been turned off. The underlying event energy is due to the interactions of the spectator partons in the colliding hadrons and the size of the correction depends on the size of the jet cone. It is approximately 0.5 GeV for a cone of radius 0.7 and is similar to the amount of energy observed in minimum bias events with a high track multiplicity. The rule-of-thumb has always been that the underlying event energy in a jet event looks very much like that observed in minimum bias events, i.e. that there is a rough factorization of the event into a hard-scattering part and a soft physics part.

Studies have been carried out with inclusive jet production in CDF, examining the transverse momentum carried by charged particles inside and outside of jets [131, 132]. For example, the geometry for one study is shown in figure 45, where the 'towards' and 'away' regions have been defined with respect to the direction of the leading jet. The transverse momenta in the two transverse regions are shown in figure 46.

The region with the largest transverse momentum is designated as the max region and the one with the lowest, the min region. As the lead jet transverse momentum increases, the
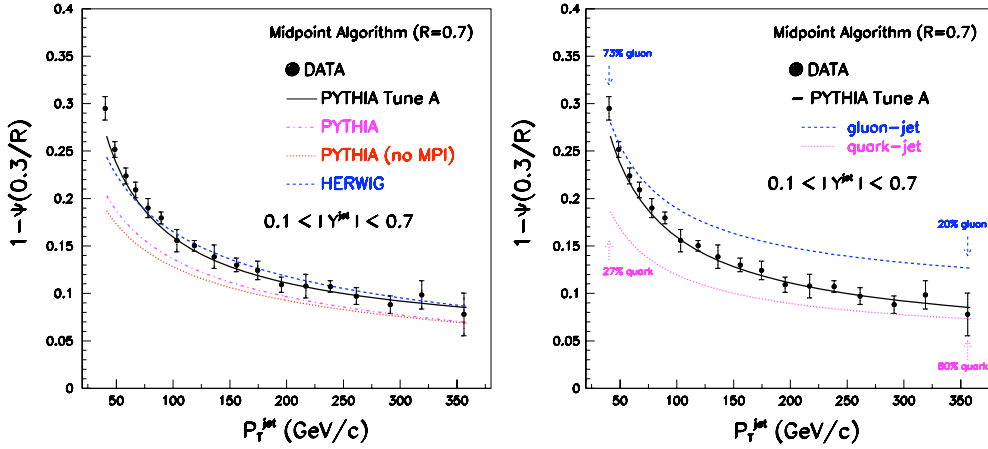
Figure 47. The fraction of the transverse momentum in a cone jet of radius 0.7 that lies in the annulus from 0.3 to 0.7, as a function of the transverse momentum of the jet. Comparisons are made to several tunes of PYTHIA (left) and to the separate predictions for quark and gluon jets (right).

momentum in the max region increases; the momentum in the min region does not. The amount of transverse momentum in the min region is consistent with that observed in minimum bias events at the Tevatron. At the partonic level, the max region can receive contributions from the extra parton present in NLO inclusive jet calculations. The min region cannot. There is good agreement between the Tevatron data and the PYTHIA tunes. Tune A was determined using the LO pdf CTEQ5L; an equivalently good agreement is also observed with a tune using the NLO pdf CTEQ6.1[16]. As discussed previously, such a tune is necessary for the use of a NLO pdf such as CTEQ6.1 with the PYTHIA Monte Carlo.

The jet shape is also well-described by PYTHIA predictions using Tune A, as can be seen in figure 47 [134], where the jet energy away from the core of the jet (i.e. in the annulus from 0.3 to 0.7) is plotted as a function of the transverse momentum of the jet. A better description is provided by the use of Tune A then with the default PYTHIA prediction. A reasonable description of the core of the jet (<0.3) can also be provided by the pure NLO prediction [14]. Jets become more collimated as the inclusive jet transverse momentum increases for three reasons: (1)) power corrections that tend to broaden the jet decrease as $1/p_T$ or $1/p_T^2$, (2) a larger fraction of jets are quark jets rather than gluon jets and (3), the probability of a hard gluon to be radiated (the dominant factor in the jet shape) decreases as $\alpha_S(p_T^2)$.

The fragmentation correction accounts for the daughter hadrons ending up outside the jet cone from mother partons whose trajectories lie inside the cone (also known as *splash-out*); it does not correct for any out-of-cone energy arising from perturbative effects as these should be correctly accounted for in a NLO calculation. It is purely a power correction to the cross section. The numerical value of the splash-out energy is roughly constant at 1 GeV for a cone of radius 0.7, independent of the jet transverse momentum. This constancy may seems surprising. But, as the jet transverse momentum increases, the jet becomes more collimated; the result is that the energy in the outermost annulus (the origin of the splash-out energy) is roughly constant. The correction for splash-out derived using parton shower Monte Carlos can be applied to a NLO parton level calculation to the extent to which both the parton shower and the 2 partons in a NLO jet correctly describe the jet shape.

[16] The parameters for the tune are given on the benchmarks website.
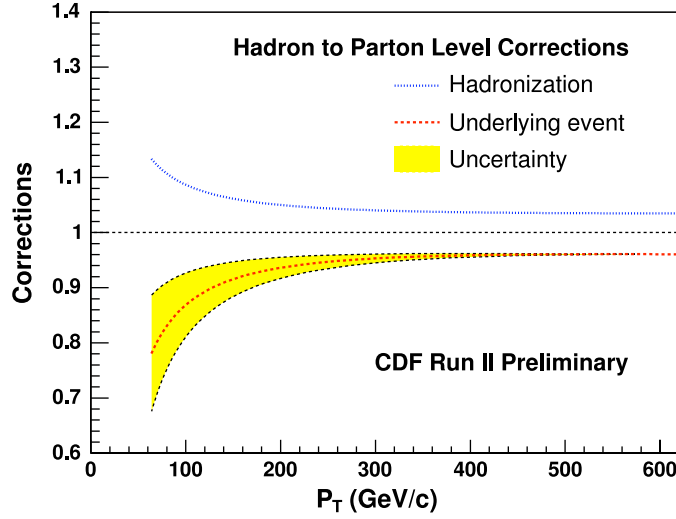
Figure 48. Fragmentation and underlying event corrections for the CDF inclusive jet result, for a cone size $R = 0.7$.

The two effects (underlying event and splash-out) go in opposite directions so there is a partial cancellation in the correction to parton level. For a jet cone of 0.7, the underlying event correction is larger, as seen in figure 48, for the case of inclusive jet production at CDF. For a jet cone radius of 0.4, the fragmentation correction remains roughly the same size but the underlying event corrections scales by the ratio of the cone areas; as a result the two effects basically cancel each other out over the full transverse momentum range at the Tevatron.

5.3.2. Results. A comparison of the inclusive jet cross section measured by CDF in Run 2 with the midpoint cone algorithm [135] to NLO pQCD predictions using the EKS [133] program with the CTEQ6.1 and MRST2004 pdfs is shown in figure 49. A renormalization/factorization scale of ($p_T^{jet}/2$) has been used in the calculation. Typically, this leads to the highest predictions for inclusive jet cross sections at the Tevatron, as discussed in section 3.3.2. There is good agreement with the CTEQ6.1 predictions over the transverse momentum range of the prediction. The MRST2004 predictions are slightly higher at lower p_T and slightly lower at higher p_T, but still in good overall agreement. As noted before, the CTEQ6.1 and MRST2004 pdfs have a higher gluon at large x as compared with previous pdfs, due to the influence of the Run 1 jet data from CDF and D0. This enhanced gluon provides good agreement with the high p_T Run 2 measurement as well which, as stated before, extends approximately 150 GeV higher in transverse momentum. The red curves indicate the pdf uncertainty for the prediction using the CTEQ6.1 pdf error set. The yellow band indicates the experimental systematic uncertainty, which is dominated by the uncertainty in the jet energy scale (on the order of 3%). The purple band shows the effect of the uncertainty due to the hadronization and underlying event, which is visible only for transverse momenta below 100 GeV. In figure 50, the jet cross sections measured with the midpoint cone algorithm are shown for the full rapidity coverage of the CDF experiment. Good agreement is observed in all rapidity regions with the CTEQ6.1 predictions. It is also important to note that for much of the kinematic range, the experimental systematic errors are less than pdf uncertainties; thus, the use of this data in future global pdf fits should serve to further constrain the gluon pdf.
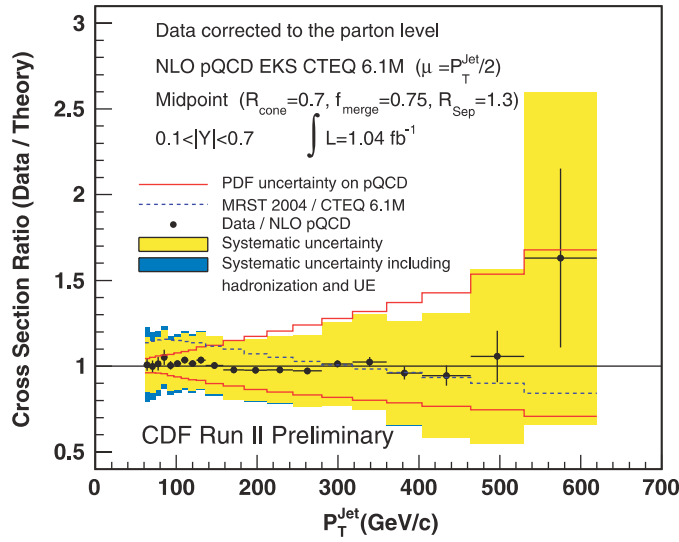
Figure 49. The inclusive jet cross section from CDF in Run 2 compared on a linear scale to NLO theoretical predictions using CTEQ6.1 and MRST2004 pdfs.
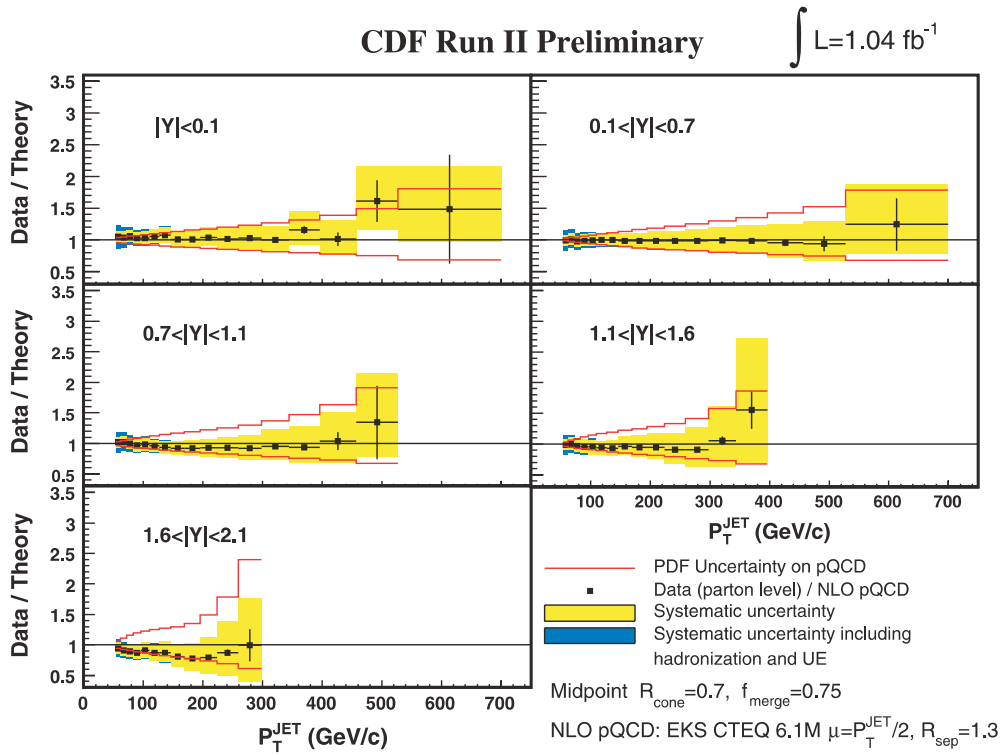
Figure 50. The inclusive jet cross section from CDF in Run 2, for several rapidity intervals using the midpoint cone algorithm, compared on a linear scale to NLO theoretical predictions using CTEQ6.1 pdfs.
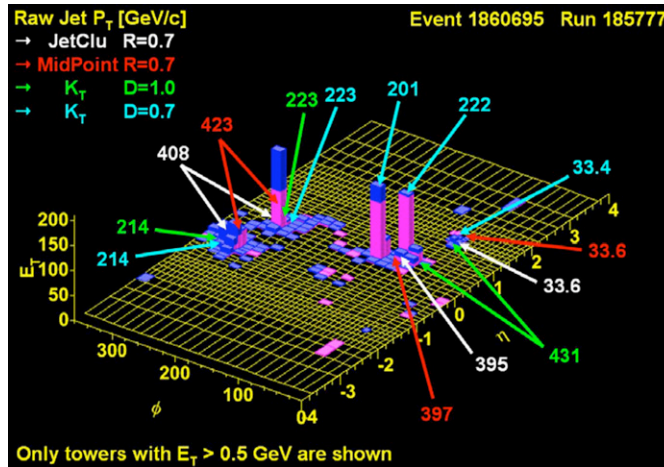
**Figure 51.** Impact of different jet clustering algorithms on an interesting event.

5.3.3. Jet algorithms and data.   For many events, the jet structure is clear and the jets to which
the individual towers should be assigned are fairly unambiguous. However, in other events
such as figure 51, the complexity of the energy depositions means that different algorithms
will result in different assignments of towers to the various jets. This is no problem to the
extent that a similar complexity can be matched by the theoretical calculation to which it is
being compared. This is the case, for example, for events simulated with parton shower Monte
Carlos, but, as discussed in section 3, current NLO calculations can place at most 2 partons in
a jet.

In figure 52, the experimental jet cross sections using the k_T algorithm from CDF
Run 2 [136] are compared with NLO predictions using the JETRAD [88] programme. Similarly
good agreement with that obtained for the midpoint cone algorithm is observed. This is
an important observation. The two different jet algorithms have different strengths and
weaknesses. It is our recommendation that, where possible, analyses at the Tevatron and
LHC use both algorithms in order to obtain more robust results.

We noted in section 3.6 that on general principles, for NLO parton level predictions, the
cone jet cross section is larger than the k_T jet cross section when $R_{cone} = D$. At the hadron
level, this is no longer true; the cone jet loses energy by the 'splash-out' effect while the k_T
algorithm has a tendency to 'vacuum up' contributions from the underlying event. This will
be corrected at least partially by the hadron-to-parton level corrections for each algorithm.

A particular complexity with the cone algorithm occurs when two jets overlap; a decision
must be made whether to merge the two jets into one, or to separate them. This is an
experimental decision; in CDF in Run 2, the two overlapping jets are merged when more
than 75% of the smaller jet energy overlaps with the larger jet. When the overlap is less, the
towers are assigned to the nearest jet. D0 uses a criterion of a 50% fraction. NLO theory is
agnostic on the subject as there is no overlap between the two partons that can comprise a jet.
Further study is needed as to which choice is best, especially for the high luminosity conditions
at the LHC.

Another problem that can arise on the particle or calorimeter level, but not on the NLO
parton level, occurs when particles or calorimeter towers remain unclustered in any jet, due to
the strong attraction of a nearby larger jet peak that will attract away any trial jet cone placed
at the location of the original particles/calorimeter towers. The result will be what [89] calls
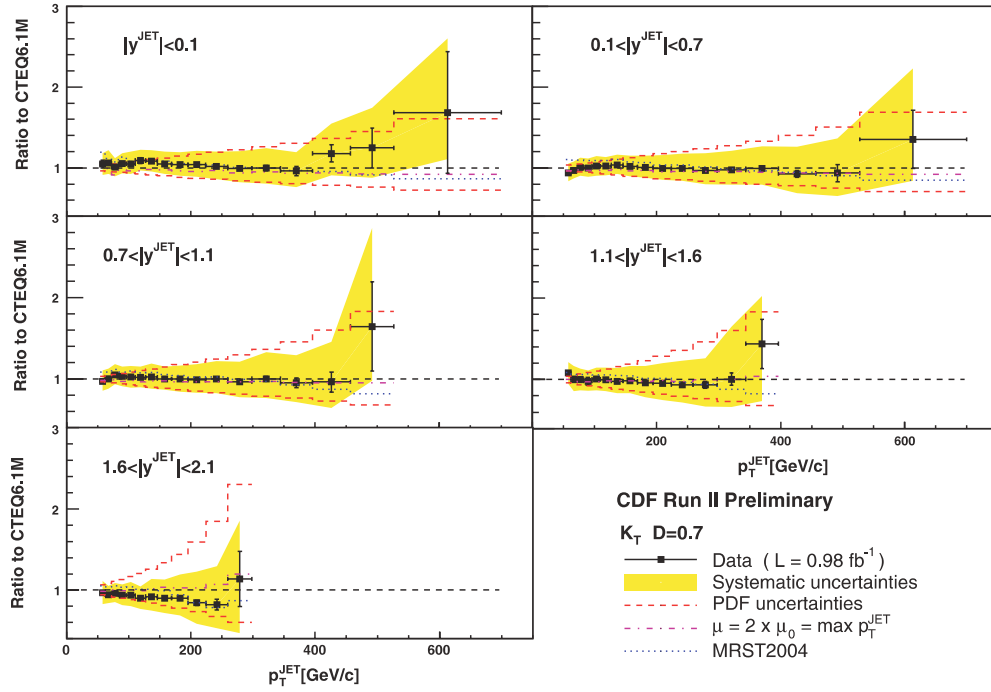
Figure 52. The inclusive jet cross section from CDF in Run 2, for several rapidity intervals using the k_T jet algorithm, compared on a linear scale to NLO theoretical predictions using CTEQ6.1 pdfs.
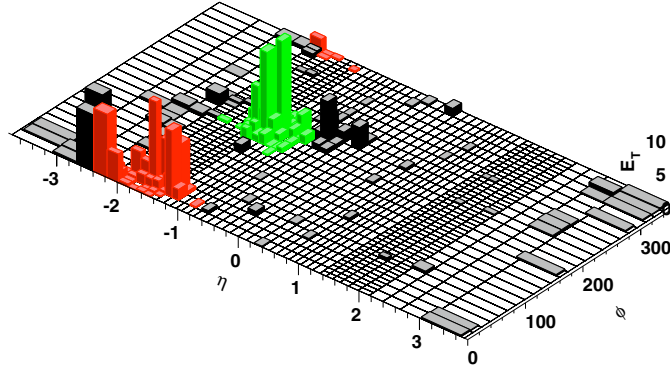
Figure 53. An example of a Monte Carlo inclusive jet event where the midpoint algorithm has left substantial energy unclustered.

'dark towers', i.e. clusters that have a transverse momentum large enough to be designated either a separate jet or to be included in an existing nearby jet, but which are not clustered into either. Such a Monte Carlo event is shown in figure 53, where the towers unclustered into any jet are shaded black. A simple way of understanding these dark towers begins by defining a 'Snowmass potential' in terms of the two-dimensional vector $\vec{r} = (y, \phi)$ via

$$V(\vec{r}) = -\frac{1}{2} \sum_j p_{T,j} \left(R_{\mathrm{cone}}^2 - (\vec{r}_j - \vec{r})^2 \right) \Theta \left(R_{\mathrm{cone}}^2 - (\vec{r}_j - \vec{r})^2 \right) . \tag{44}$$
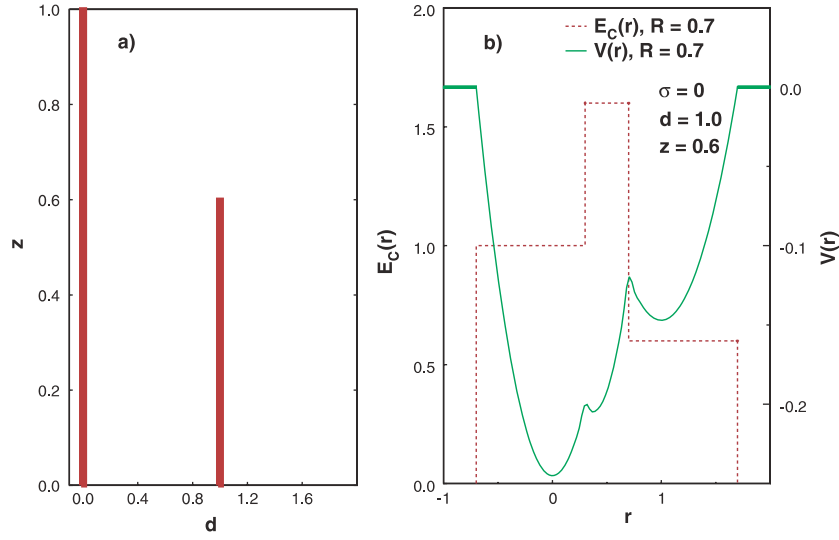
Figure 54. A schematic depiction of a specific parton configuration and the results of applying the midpoint cone jet clustering algorithm. The potential discussed in the text and the resulting energy in the jet are plotted.

The flow is then driven by the 'force' $\vec{F}(\vec{r}) = -\vec{\nabla}V(\vec{r})$ which is thus given by,

$$\vec{F}(\vec{r}) = \sum_j p_{T,j}(\vec{r}_j - \vec{r})\,\Theta\left(R_{\text{cone}}^2 - (\vec{r}_j - \vec{r})^2\right)$$

$$= \left(\vec{\bar{r}}_{C(\vec{r})} - \vec{r}\right) \sum_{j \subset C(r)} p_{T,j}, \tag{45}$$

where $\vec{\bar{r}}_{C(\vec{r})} = \left(\bar{y}_{C(\vec{r})}, \bar{\phi}_{C(\vec{r})}\right)$ and the sum runs over $j \subset C(\vec{r})$ such that $\sqrt{(y_j - y)^2 + (\phi_j - \phi)^2}$ $\leqslant R_{\text{cone}}$. As desired, this force pushes the cone to the stable cone position.

In figure 54 (left), two partons are placed at a distance $\Delta R = 0.9$ apart; the second parton has a fractional energy 0.6 that of the first parton. On the right, the potential $V(r)$ and the energy contained inside a cone of radius 0.7 are plotted for this parton configuration. At the parton level, there are three positions where minima are present in the potential: at the position of the left parton, the right parton and the midpoint between the two partons. The midpoint jet algorithm applied to a NLO parton level calculation, as discussed in section 3.6, would find all three solutions. In figure 55(left), the spatial distributions of the two partons' energies have been smeared with a spatial resolution σ of 0.1, as would take place for example due to the effects of parton showering and hadronization. The central minimum is wiped out by the smearing. On the right, the spatial distributions of the two partons' energy distributions have been smeared with a resolution σ of 0.25 and both the midpoint and right minima have been wiped out. Any attempt to place the centroid of a jet cone at the position of the right parton will result in the centroid 'sliding' to the position of the left parton and the energy corresponding to the right parton remaining unclustered in any jet. This is the origin of the dark towers. The effective smearing in the data lies between a σ of 0.1 and 0.25.

The TeV4LHC workshop [93] has recommended the following solution to the problem of unclustered energy with cone jet algorithms, which we pass on as one of our recommendations as well. The standard midpoint algorithm should be applied to the list of calorimeter
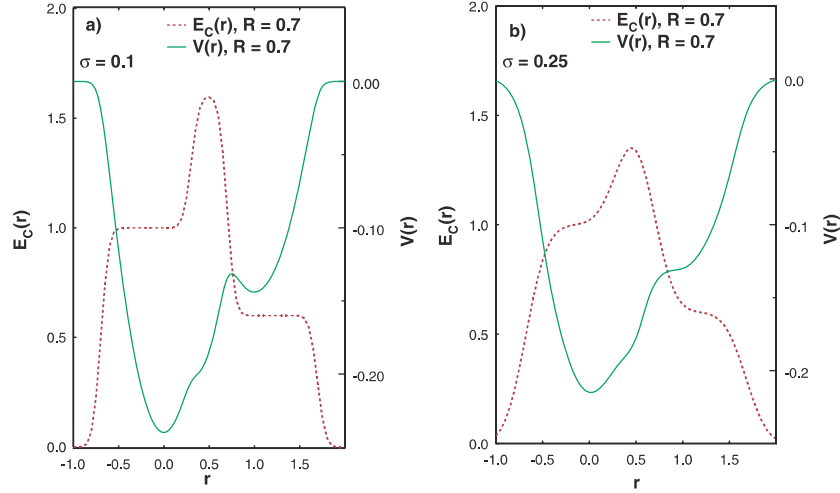
Figure 55. A schematic depiction of the effects of smearing on the midpoint cone jet clustering algorithm.

towers/particles/partons, including the full split/merge procedure. The resulting identified jets are then referred to as first pass jets and their towers/particles/partons are removed from the list. The same algorithm is then applied to the remaining unclustered energy and any jets that result are referred to as second pass jets. There are various possibilities for making use of the second pass jets. They can be kept as separate jets, in addition to the first pass jets, or they can be merged with the nearest first pass jets. The simplest solution, until further study, is to keep the second pass jets as separate jets. The coding of this solution is available in the midpoint algorithm given on the benchmark website.

It was originally thought that with the addition of a midpoint seed, the value of R_{sep} used with the NLO theory could be returned to its *natural* value of 2.0(cf section 3.6). Now it is realized that the effects of parton showering/hadronization result in the midpoint solution virtually always being lost. Thus, a value of R_{sep} of 1.3 is required for the NLO jet algorithm to best model the experimental one. The theory cross section with $R_{\mathrm{sep}} = 1.3$ is approximately 3–5% smaller than with $R_{\mathrm{sep}} = 2.0$, decreasing slowly with the jet transverse momentum.

5.3.4. Inclusive jet production at the Tevatron and global pdf fits. Inclusive jet production receives contributions from gg, gq and $qq(q\bar{q})$ initial-states as shown in figure 56 [11]. The experimental precision of the measurement, along with the remaining theoretical uncertainties, means that the cross sections do not serve as a meaningful constraint on the quark or antiquark distributions. However, they do serve as an important constraint on the gluon distribution, especially at high x. Figure 57 shows the gluon distributions for the CTEQ and MRST groups prior to the inclusion of any inclusive jet data and the latest sets which include the Run 1 data from both CDF and D0. The influence of the high E_T Run 1 jet cross section on the high x gluon is evident. There is always the danger of sweeping new physics under the rug of pdf uncertainties. Thus, it is important to measure the inclusive jet cross section over as wide a kinematic range as possible. New physics tends to be central while a pdf explanation should be universal, i.e. fit the data in all regions.
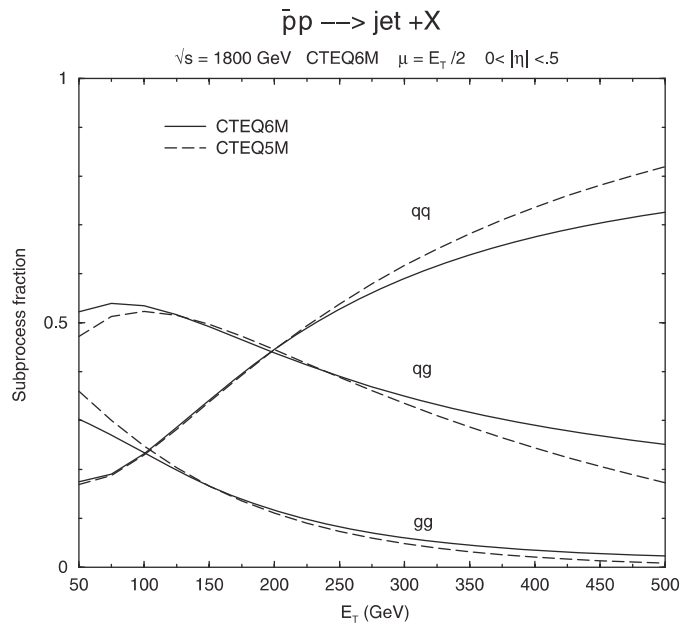
Figure 56. The subprocess contributions to inclusive jet production at the Tevatron for the CTEQ5M and CTEQ6M pdfs. The impact of the larger larger gluon at high x for CTEQ6 is evident.
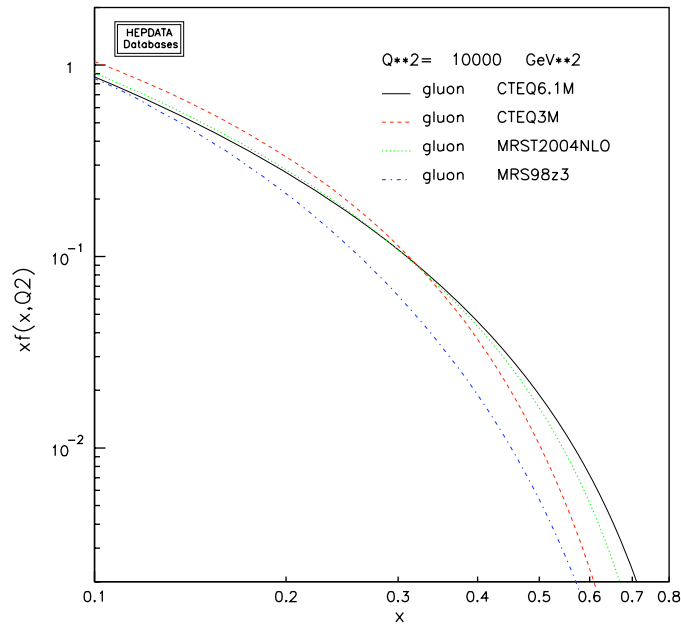
**Figure 57.** Gluon pdfs before and after the inclusion of Tevatron inclusive jet data.
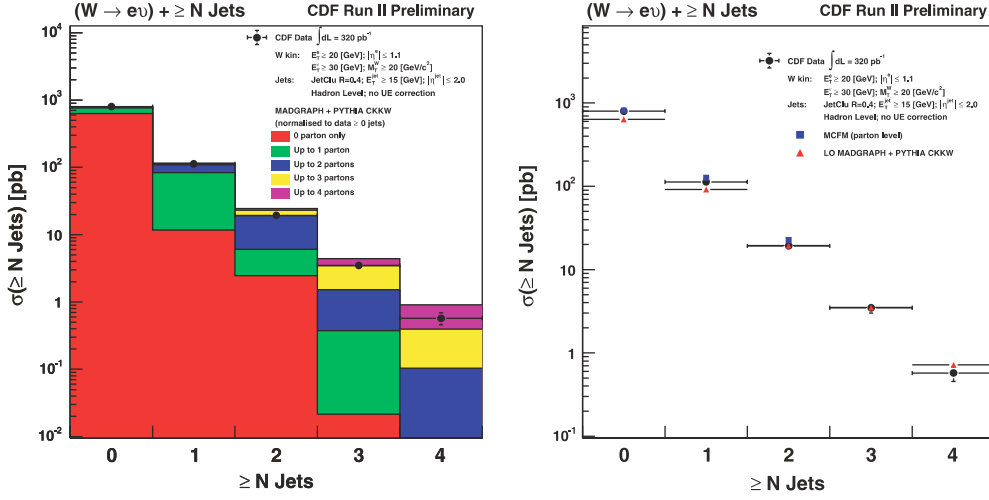
Figure 58. The rate of production of *W* + *n* jets at CDF, compared to CKKW (left) and also NLO QCD using MCFM (right). The measurements and predictions were performed with a cone jet of radius 0.4 and with a requirement of 15 GeV or greater. The CKKW predictions are normalized to the first bin and use a scale of 10 GeV for the matching; the MCFM predictions are absolutely normalized.

5.4. W/Z + jets

The production of a *W* or *Z* boson in conjunction with jets is an interesting process in its own right as well as a background to many SM and non-SM physics signals. Jet multiplicities of up to 7 have been measured at the Tevatron. Production of *W*/*Z*+ jets at the Tevatron is dominated by *gq* initial-states. The NLO cross sections have been calculated only for *W*/*Z* + 2 jets; predictions for the higher jet multiplicity final states are accessible through matrix element (+ parton shower) predictions and in fact can be considered a prime testing ground for the accuracy of such predictions as well as for measurements of α_S. Some comparisons to a recent measurement of $W \rightarrow e\nu+ \geqslant n$ jets from CDF are shown below [130]. In this analysis, the data have been reconstructed using the CDF Run 1 cone algorithm (with a midpoint cone analysis to come) with a cone radius of 0.4. A smaller jet cone size is preferred for final states that may be 'complicated' by the presence of a large number of jets. The data have been compared, at the hadron level, to predictions using matrix element information from ALPGEN and parton shower and hadronization information from PYTHIA.

The jet multiplicity distribution for *W* + *n* jets measured at the Tevatron is shown in figure 58. In the left-hand plot, the data have been compared to the CKKW predictions from [94] (normalized to the first bin of the data). The CKKW predictions use matrix element information for up to 4 partons in the final state. Thus, most of the cross section in the $\geqslant$ 4-jet bin has been constructed from the 4 parton matrix element information, but a non-negligible number of events have been generated from a 2 or 3 parton final state, with the extra jets coming from the parton shower. In the right-hand plot, the jet multiplicity distribution is shown again, this time compared as well with the NLO (LO) prediction from MCFM for the 1, 2 (3) jet final states. The CKKW prescription agrees well with the NLO calculation for the jet multiplicities where it is available and agrees reasonably well with the Tevatron data for the range shown. Note that the production of each additional jet in this inclusive distribution is suppressed by a factor of the order of 0.2, or approximately α_S.
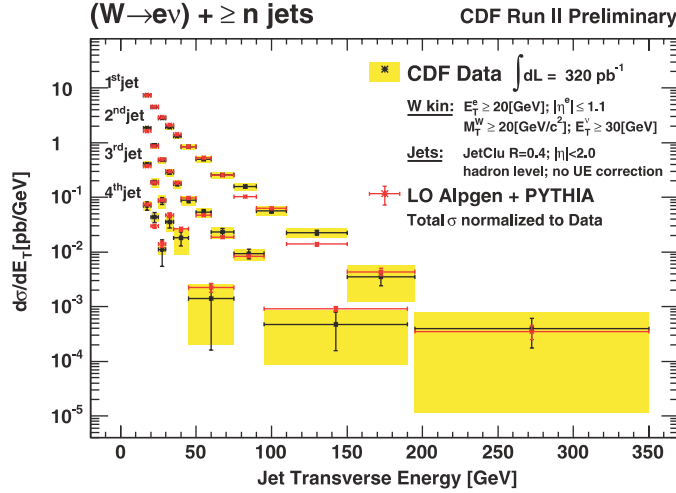
Figure 59. A comparison of the measured cross sections for $W+ \geqslant n$ jets in CDF Run 2 to predictions from ALPGEN+PYTHIA. The experimental cross sections have been corrected to the hadron level.

A comparison of the measured cross sections for $W+ \geqslant n$ jets in CDF Run 2 as a function of the jet transverse momentum, to predictions from ALPGEN+PYTHIA is shown in figure 59. The agreement is good. Note that this data is in a form (at the hadron level, corrected for detector effects) that makes it convenient for comparison to any hadron level Monte Carlo prediction[17]. Such a form should be the norm for measurements at both the Tevatron and LHC.

Comparisons with the NLO predictions of MCFM will be available in the near future. There is little change in normalization in going from LO to NLO predictions; as we saw in section 3, the K-factor for these processes is close to unity. The major impact of the NLO corrections for the two highest p_T jets is to soften the distributions. The NLO calculation allows some of the momentum of the hard partons to be carried off by gluon radiation. A similar effect also occurs with the CKKW calculation where again there is the possibility for the parton momentum to be decreased by additional branchings. This is an instance of where parton showering contains some of the physics present in NLO calculations.

The transverse momentum distribution for the highest p_T jet in $W+$ jets events at CDF is shown in figure 60, etc along with the CKKW predictions. Both the total CKKW prediction and its decomposition into $W+1$ jet, $W+2$ jet, ... contributions are indicated. As the transverse momentum of the lead jet increases, more contributions are seen to come from the higher jet multiplicity CKKW components. The exact subdivision of contributions will depend on where the cutoff was applied in the formation of the CKKW sample. Note that when the lead jet has a transverse momentum of the order of 200 GeV, the events are dominated by the higher multiplicity matrix elements, i.e. there is a large probability for the event to contain a second (or more) jet given the large p_T of the first. If the same transverse momentum cut were applied to all jets in the event, then the expectation would be that adding an additional jet would lead to a penalty of α_S (as we have seen for the inclusive jet multiplicity distribution). In this case, since the additional jet is soft compared with the leading jet, α_S is multiplied by a log relating the energies of the leading and additional jet. The logarithm more than makes up for the factor

---

[17] As mentioned before, the corrections for underlying event and for fragmentation basically cancel each other out for a cone of radius 0.4, so that the hadron level predictions are essentially parton level predictions as well

(W → eυ) + ≥ 1 Jets   **CDF Run II Preliminary**
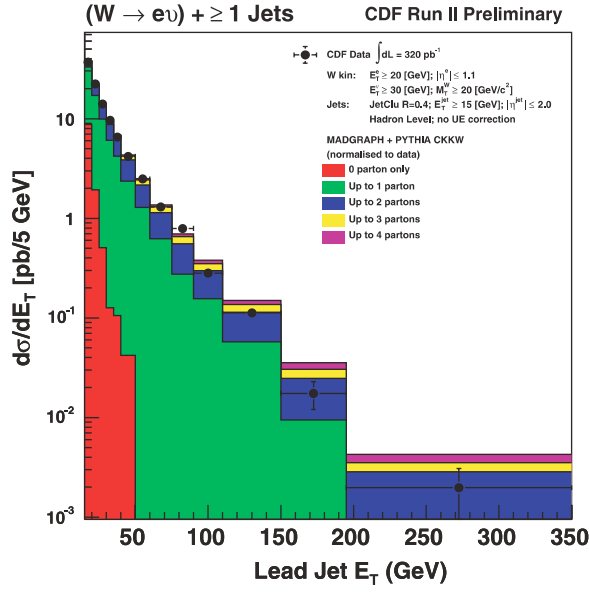
Figure 60. The E_T distribution of the lead jet in $W + \geqslant 1$ jet events, along with the CKKW decomposition.

of α_S. Another way of looking at the jet multiplicity is to say that there would be a Sudakov suppression on each of the incoming and outgoing parton legs if a requirement was imposed that no extra jet be produced. An estimate of the approximate size of the Sudakov suppression can be made using the figures given in section 3.

A category of $W/Z+$ jets event that has drawn particular interest lately is where two jets are produced separated by a large rapidity gap. Such a configuration (involving a Z) serves as a background to vector boson fusion (VBF) production of a Higgs boson, where the two forward-backward jets serve to tag the event. As the Higgs boson is produced through a colourless exchange, the rate for an additional jet to be produced in the central region between the two tagging jets should be suppressed with respect to the QCD production of $Z + \geqslant 2$ jets. The probability for an additional jet to be emitted in QCD $W + 2$ jet events (rather than Z, in order to obtain a higher rate), plus the ability of various theoretical predictions to describe this rate, is a measurement that can be carried out at the Tevatron prior to the turn-on of the LHC. Such a measurement is shown in figure 61, where the rate for a 3rd jet to be emitted is shown versus the rapidity separation of the two tagging jets. It is evident that (1) the rate for a 3rd jet to be produced is large and (2) that the observed rate is in agreement with the CKKW predictions, and is bracketed by the predictions of MCFM for two choices of scale. Since the prediction is for $W + 3$ jets, the MCFM calculation is at LO and retains a large scale dependence. The $W/Z + 3$ jets process is one to which high priority has been given for calculation to NLO, as will be discussed in section 6.5. The rate for an additional jet to be emitted is roughly independent of the rapidity separation of the two tagging jets. The agreement of the data with the CKKW predictions is heartening for two reasons: (1) it indicates that CKKW predictions will most likely provide accurate predictions for similar topologies at the LHC and (2) the rate for additional jet production in $W/Z + 2$ widely separated jet events is high, leading to an effective veto in VBF Higgs boson searches at the LHC.

For many of the analyses at the Tevatron, it is useful to calculate the rate of leading-order parton shower Monte Carlo predictions. For example, the Method 2 technique [137] in CDF's
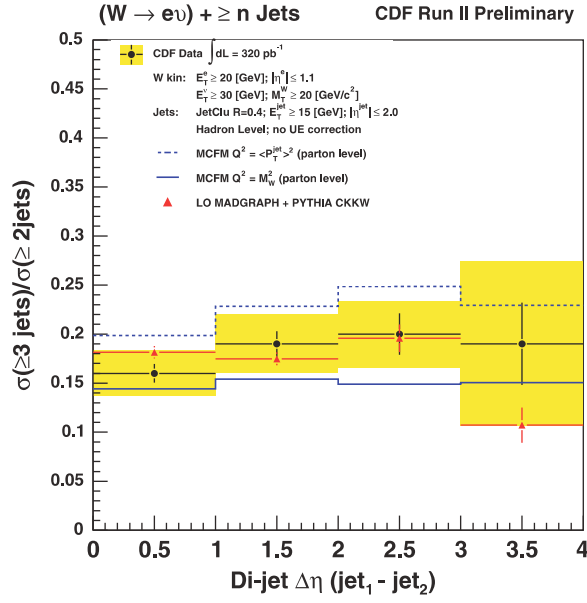
Figure 61. Predictions and a measurement from CDF Run 2 for the rate for the production of a third jet in $W+ \geqslant 2$ jet events, as a function of the rapidity separation of the two lead jets.

top analysis uses the calculated ratio of $[Wb\bar{b}+(n-2)$ jets]$/[W+n$ jets] (for $n = 3, 4$) and the measured rate for $W+n$ jets to calculate the $Wb\bar{b}+(n-2)$ jet background to top production. The ratio of the two processes should be more reliable than the absolute leading-order prediction for $Wb\bar{b} + (n - 2)$ jets. The above statement should be true as long as the NLO corrections (the K-factors) do not have an appreciable difference in shape between the two processes. As discussed previously, NLO corrections are available for $Wb\bar{b}$ and Wjj but not for higher jet multiplicities. A recent study has shown that the relative shape of the two processes is indeed different at NLO if highly exclusive variables (such as H_T, the sum of the transverse energy of all final-state objects in the event) are used for the measurement [139]. On the other hand, inclusive variables such as the transverse momentum of the leading jet seem to be safe in this regard. The dependence of the ratio on these two variables is contrasted in figure 62. There is some indication that the change in shape observed in going from LO to NLO can also be reproduced by including higher jet multiplicities using the CKKW procedure.

5.5. $t\bar{t}$ production at the Tevatron

Perhaps the greatest discovery at the Tevatron was that of the top quark. The production mechanism was through $t\bar{t}$ pair production, dominated by a $q\bar{q}$ initial-state. The top quark decays essentially 100% into a W and a b quark; thus the final states being investigated depend on the decays of the two W's. The most useful (combination of rate and background) final state occurs when one of the W's decays into a lepton and neutrino and the other decays into two quarks. Thus, the final state consists of a lepton, missing transverse energy and of the order of four jets. The number of jets may be less than 4 due to one or more of the jets not satisfying the kinematic cuts, or more than 4 due to additional jets being created by gluon radiation off the initial or final state. Because of the relatively large number of jets, a smaller cone size ($R = 0.4$) has been used for jet reconstruction. Unfortunately, no top analysis has
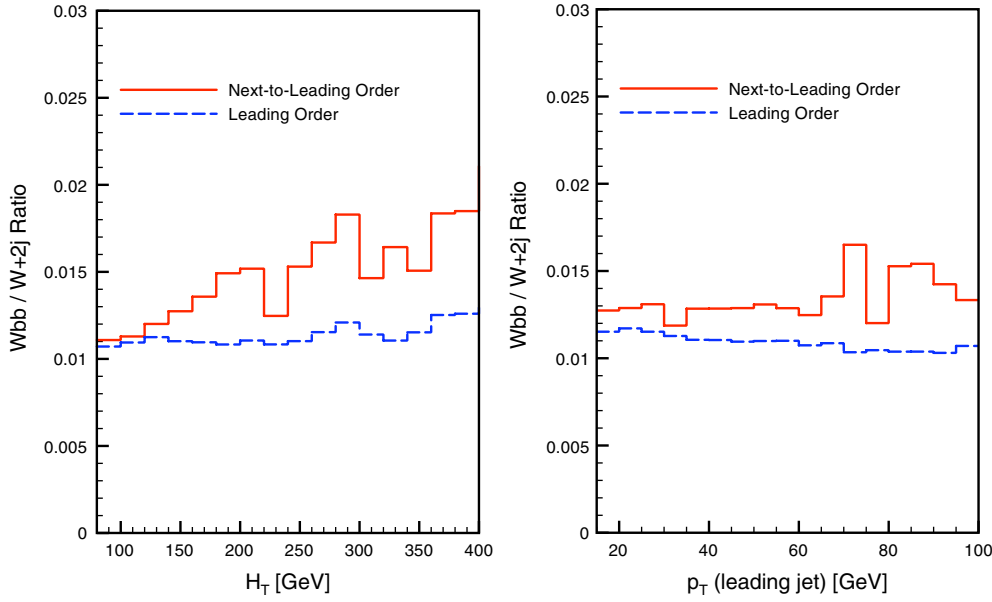
Figure 62. The ratio of the cross sections for $Wb\bar{b}$ and Wjj is plotted at LO and NLO as a function of the variables H_T (left) and the p_T of the leading jet (right). The ratio is observed to have a different slope at NLO than at LO on the left, but a similar slope on the right.

yet been performed using the k_T jet algorithm. There is a sizeable background for this final state through QCD production of $W+$ jets. Two of the jets in $t\bar{t}$ events are created by b quarks; thus there is the additional possibility of an improvement in signal purity by the requirement of one or two b-tags.

In figure 63 are shown the CDF measurement of the H_T (sum of the transverse energies of all jets, leptons, missing E_T in the event) distribution for lepton $+ \geqslant 4$ jets final states, along with the predictions for the H_T distributions from $t\bar{t}$ events and from the $W+$ jets background [140, 141]. A requirement of high H_T improves the $t\bar{t}$ signal purity, as the jets from the $t\bar{t}$ decays tend to be at higher transverse momentum than from the QCD backgrounds.

The jet multiplicity distribution for the top candidate sample from CDF in Run 2 is shown in figure 64 for the case of one of the jets being tagged as a b-jet (left) and two of the jets being tagged (right) [137, 142]. The requirement of one or more b-tags greatly reduces the $W+$ jets background in the 3 and 4 jet bins, albeit with a reduction in the number of events due to the tagging efficiency.

The lepton + jets final state (with one or more b-tags) is also the most useful for the determination of the top mass. A compilation of top mass determinations from the Tevatron is shown in figure 65 (left) along with the implications for the measured top and W masses for the Higgs mass (right) [143].

The precision of the top mass determination has reached the point where some of the systematics due to QCD effects must be considered with greater care. One of the larger systematics is that due to the effects of initial-state radiation. Jets created by initial-state radiation may replace one or more of the jets from the top quark decays, affecting the reconstructed top mass. In the past, the initial-state radiation (ISR) systematic was determined by turning the radiation off/on, leading to a relatively large impact. A more sophisticated treatment was adopted in Run 2, where the tunings for the parton shower Monte Carlos
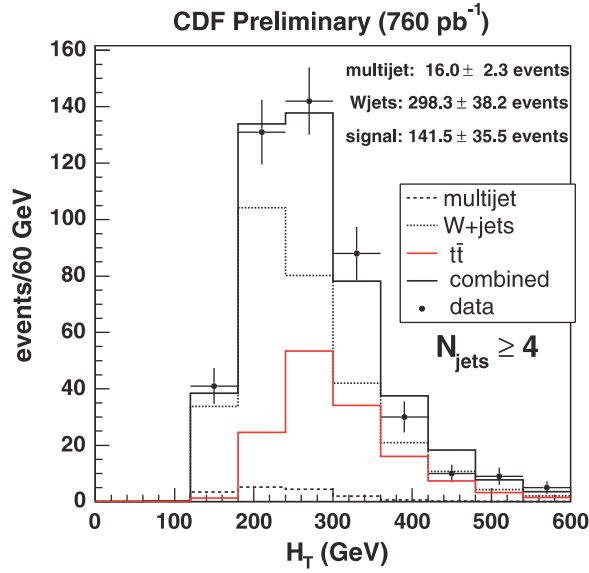
Figure 63. The H_T distribution in $W+ \geqslant 4$ jet events at CDF, along with the fitted components for $t\bar{t}$ production and backgrounds from W + jets and multijet events.
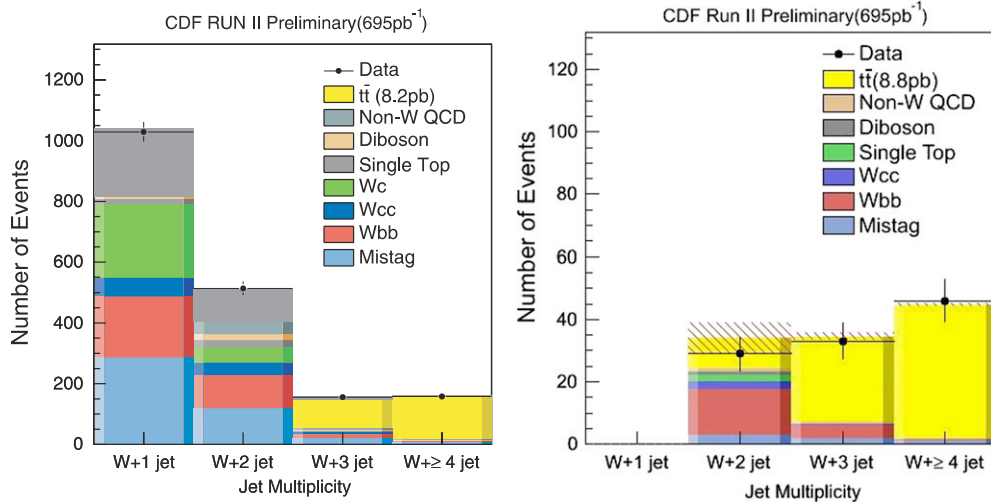

Figure 64. The expected number of $W+$ jets tagged (left) and double-tagged (right) events indicated by source.

were modified leading to more/less initial-state radiation, in keeping with the uncertainties associated with Drell–Yan measurements as discussed in section 5.1. The resultant $t\bar{t}$ pair transverse momentum distributions are shown in figure 66. The changes to the $t\bar{t}$ transverse momentum distribution created by the tunes are relatively modest, as is the resultant systematic error on the top mass determination.

Note that the peak of the $t\bar{t}$ transverse momentum spectrum is slightly larger than that for Z production at the Tevatron, due to the larger mass of the $t\bar{t}$ system. As both are produced primarily by $q\bar{q}$ initial-states, the differences are not large.
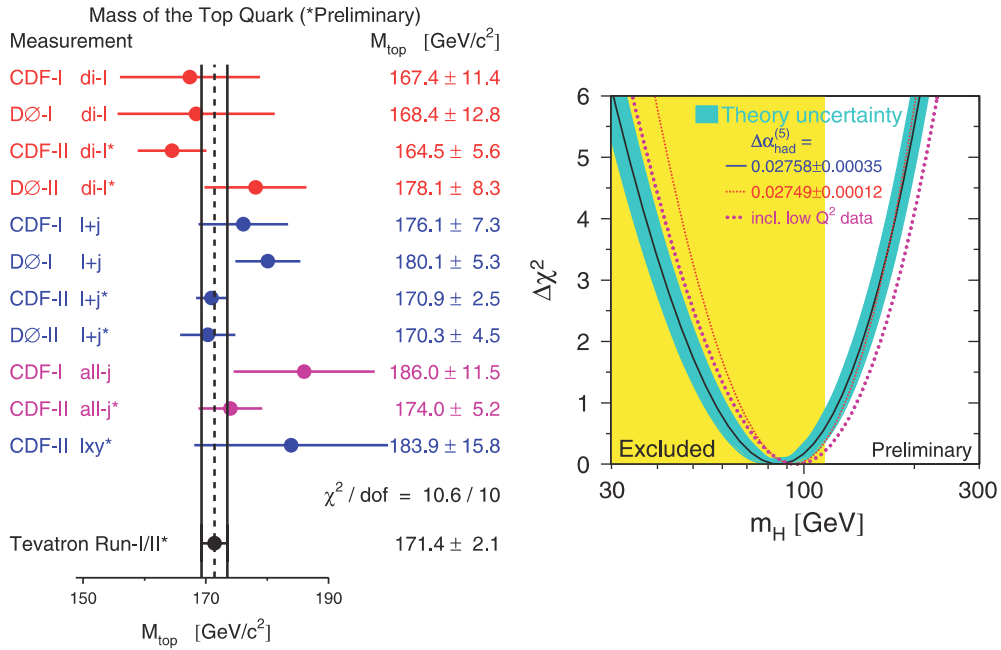
Figure 65. A compilation of the top quark mass measurements from CDF and D0 (left) and the implications for the mass of the Higgs boson (right).
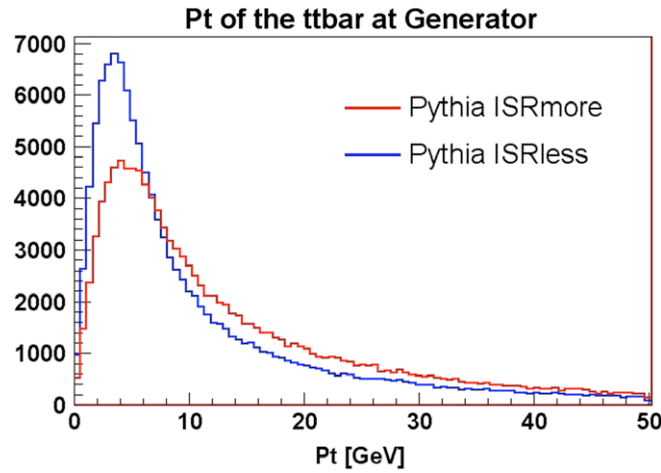
Figure 66. The PYTHIA predictions for the $t\bar{t}$ transverse momentum using the 'Plus/Minus' tunes.

It is also interesting to look at the mass distribution of the $t\bar{t}$ system, as new physics (such as a Z' [144]) might couple preferentially to top quarks. Such a comparison for CDF Run 2 is shown in figure 67 where no signs of a high mass resonance are evident. If we look at predictions for the $t\bar{t}$ mass distribution at NLO, we see that the NLO cross section is substantially less than the LO one at high mass (see figure 68). This should be taken into account in any searches for new physics at high $t\bar{t}$ mass.
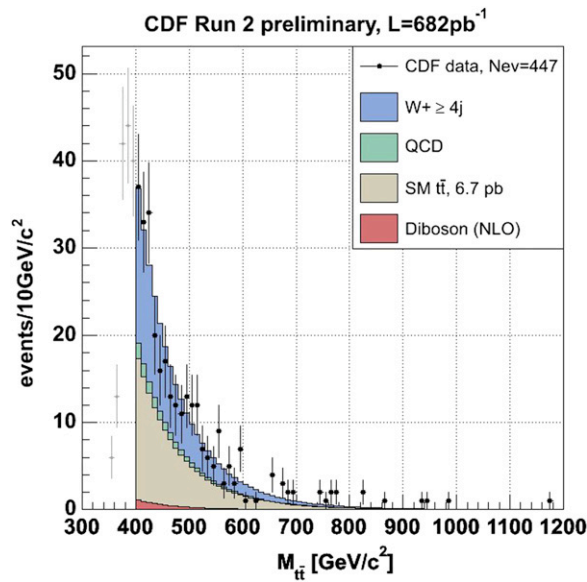
Figure 67. The $t\bar{t}$ mass distribution as observed by CDF in Run 2.
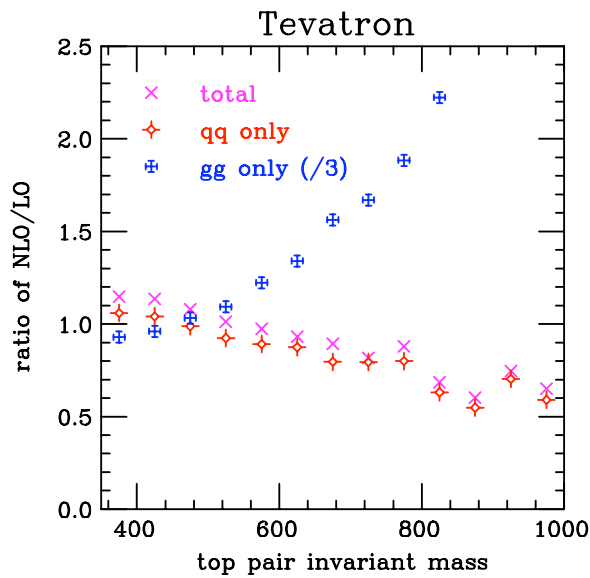
Figure 68. The ratio of the NLO to LO predictions for the $t\bar{t}$ mass at the Tevatron. The predictions include the ratio for the total cross section and for the specific $q\bar{q}$ and gg initial-states. Note that the total also includes a gq contribution (not present at LO) and that the gg ratio is divided by a factor of 3.

Further investigation shows that the decrease in NLO compared with LO at high mass is found only in the $q\bar{q}$ initial-state and not in the gg initial-state. In fact, at the Tevatron, the ratio of NLO to LO for gg initial-states grows dramatically with increasing top pair invariant mass. This effect is largely due to the increase in the gluon distribution when going from CTEQ6L1

in the LO calculation to CTEQ6M at NLO. For instance, at $x \sim 0.4$ (and hence an invariant mass of about 800 GeV) the gluon distribution is about a factor two larger in CTEQ6M than in CTEQ6L1, giving a factor of four increase in the cross section. Conversely, the quark distribution is slightly decreased at such large x. However, the absolute contribution of the $t\bar{t}$ cross at high masses from gg initial-states is small, due to the rapidly falling gluon distribution at high x.

6. Benchmarks for the LHC

6.1. Introduction

Scattering at the LHC is not simply *rescaled* scattering at the Tevatron. For many of the key processes the typical momentum fractions x are small; thus, there is a dominance of sea quark and gluon scattering as compared with valence quark scattering at the Tevatron. There is a large phase space for gluon emission and thus intensive QCD backgrounds for many of the signatures of new physics. Many of the scales relating to interesting processes are large compared with the W mass; thus, electroweak corrections can become important even for nominal QCD processes. In this section, we will try to provide some useful benchmarks for LHC predictions.

6.2. Parton-parton luminosities at the LHC[18]

It is useful to return to the idea of differential parton–parton luminosities. Such luminosities, when multiplied by the dimensionless cross section $\hat{s}\hat{\sigma}$ for a given process, provide a useful estimate of the size of an event cross section at the LHC. Below we define the differential parton–parton luminosity $dL_{ij}/d\hat{s}\,dy$ and its integral $dL_{ij}/d\hat{s}$:

$$\frac{dL_{ij}}{d\hat{s}\,dy} = \frac{1}{s}\frac{1}{1+\delta_{ij}}\left[f_i(x_1,\mu)f_j(x_2,\mu) + (1 \leftrightarrow 2)\right]. \qquad (46)$$

The prefactor with the Kronecker delta avoids double-counting in case the partons are identical. The generic parton model formula

$$\sigma = \sum_{i,j}\int_0^1 dx_1\,dx_2\,f_i(x_1,\mu)\,f_j(x_2,\mu)\,\hat{\sigma}_{ij} \qquad (47)$$

can then be written as

$$\sigma = \sum_{i,j}\int\left(\frac{d\hat{s}}{\hat{s}}\,dy\right)\left(\frac{dL_{ij}}{d\hat{s}\,dy}\right)\left(\hat{s}\,\hat{\sigma}_{ij}\right). \qquad (48)$$

(Note that this result is easily derived by defining $\tau = x_1 x_2 = \hat{s}/s$ and observing that the Jacobian $\partial(\tau,y)/\partial(x_1,x_2) = 1$.)

Equation (48) can be used to estimate the production rate for a hard scattering process at the LHC as follows. Figure 69 shows a plot of the luminosity function integrated over rapidity, $dL_{ij}/d\hat{s} = \int(dL_{ij}/d\hat{s}\,dy)\,dy$, at the LHC $\sqrt{s} = 14$ TeV for various parton flavour combinations, calculated using the CTEQ6.1 parton distribution functions [11]. The widths of the curves indicate an estimate of the pdf uncertainties. We assume $\mu = \sqrt{\hat{s}}$ for the scale[19]. As expected, the gg luminosity is large at low $\sqrt{\hat{s}}$ but falls rapidly with respect to the other parton luminosities. The gq luminosity is large over the entire kinematic region plotted.

[18] Parts of this discussion also appeared in a contribution to the Les Houches 2005 proceedings [149] by A Belyaev, J Huston and J Pumplin.
[19] Similar plots made with earlier pdfs are shown in Ellis, Stirling, Webber [8]
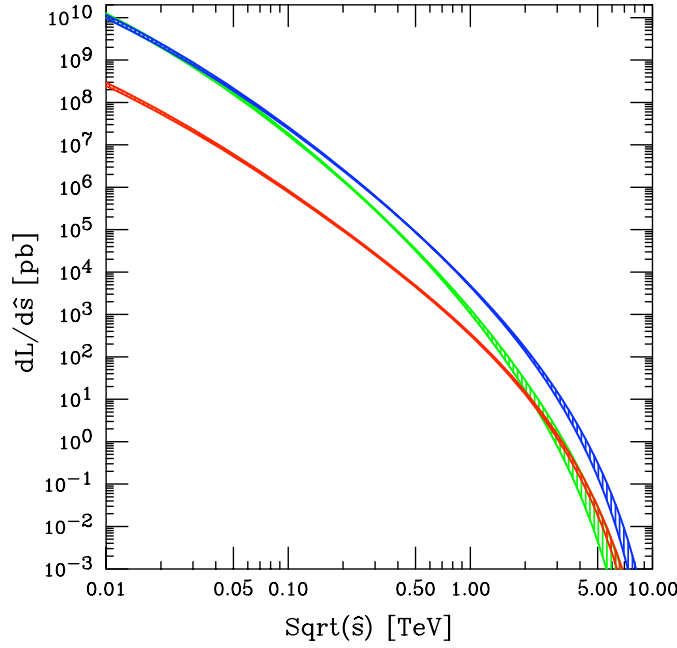
Figure 69. The parton–parton luminosity $\left[\frac{dL_{ij}}{d\tau}\right]$ in picobarns, integrated over y. Green=gg, Blue=$\sum_i (gq_i + g\bar{q}_i + q_i g + \bar{q}_i g)$, Red=$\sum_i (q_i \bar{q}_i + \bar{q}_i q_i)$, where the sum runs over the five quark flavours d, u, s, c, b.

Figures 70 and 71 present the second product, $\left[\hat{s}\hat{\sigma}_{ij}\right]$, for various $2 \to 2$ partonic processes with massless and massive partons in the final state, respectively. The parton level cross sections have been calculated for a parton $p_T > 0.1 \times \sqrt{\hat{s}}$ cut and for fixed $\alpha_S = 0.118$ using the CalcHEP package [150]. For the case of massive partons in the final state, there is a threshold behaviour not present with massless partons. Note also that the threshold behaviour is different for $q\bar{q}$ and gg initial-states. The gg processes can proceed through the t-channel as well as the s-channel and this is responsible for the extra structure.

The products $\left[\hat{s}\hat{\sigma}_{ij}\right]$ are plotted for massless and massive final-state partons as a function of the ratio $p_T/\sqrt{\hat{s}}$ in figures 72 and 73. One can use (48) in the form

$$\sigma = \frac{\Delta\hat{s}}{\hat{s}} \left(\frac{dL_{ij}}{d\hat{s}}\right) \left(\hat{s}\,\hat{\sigma}_{ij}\right). \tag{49}$$

and figures 70–73 to estimate the QCD production cross sections for a given $\Delta\hat{s}$ interval and a particular cut on $p_T/\sqrt{\hat{s}}$. For example, for the $gg \to gg$ rate for $\hat{s} = 1\,\text{TeV}$ and $\Delta\hat{s} = 0.01\hat{s}$, we have $dL_{gg}/d\hat{s} \simeq 10^3$ pb and $\hat{s}\,\hat{\sigma}_{gg} \simeq 20$ leading to $\sigma \simeq 200$ pb (for the $p_T^g > 0.1 \times \sqrt{\hat{s}}$ cut we have used above). Note that for a given small $\Delta\hat{s}/\hat{s}$ interval, the corresponding invariant mass $\Delta\sqrt{\hat{s}}/\sqrt{\hat{s}}$ interval, is $\Delta\sqrt{\hat{s}}/\sqrt{\hat{s}} \simeq \frac{1}{2}\Delta\hat{s}/\hat{s}$. One should also mention that all hard cross sections presented in figure 70 are proportional to α_S^2 and have been calculated for $\alpha_S = 0.118$, so production rates can be easily rescaled for a particular α_S at a given scale.

One can further specify the parton–parton luminosity for a specific rapidity y and $\hat{s}$, $dL_{ij}/d\hat{s}\,dy$. If one is interested in a specific partonic initial-state, then the resulting differential luminosity can be displayed in families of curves as shown in figure 74, where the differential parton–parton luminosity at the LHC is shown as a function of the subprocess centre-of-mass energy $\sqrt{\hat{s}}$ at various values of rapidity for the produced system for several different
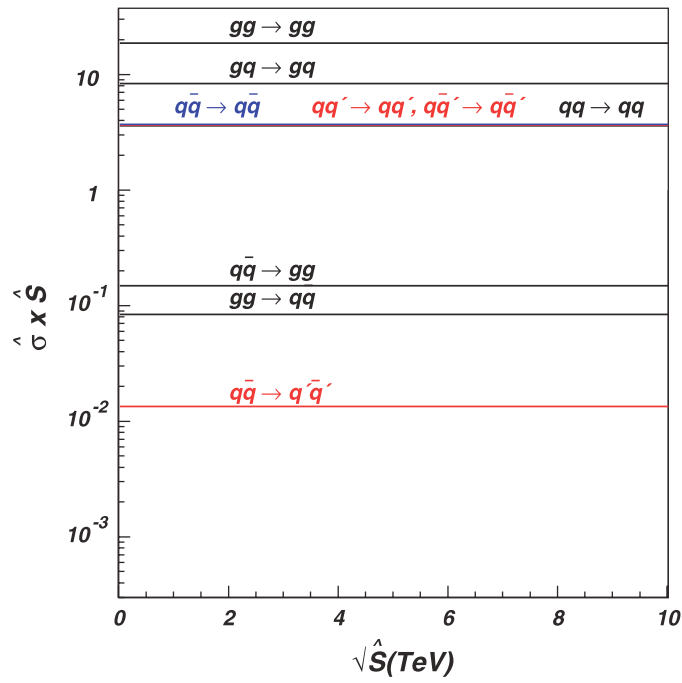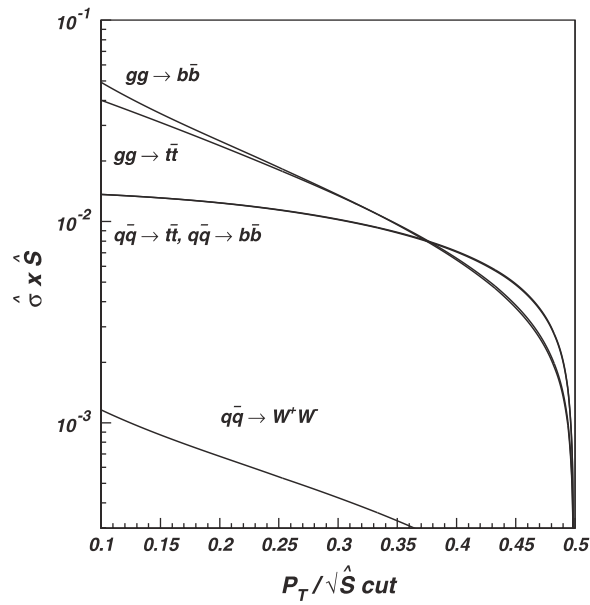
Figure 70. Parton level cross sections $\left(\hat{s}\hat{\sigma}_{ij} \right)$ for various processes involving massless partons in the final state.
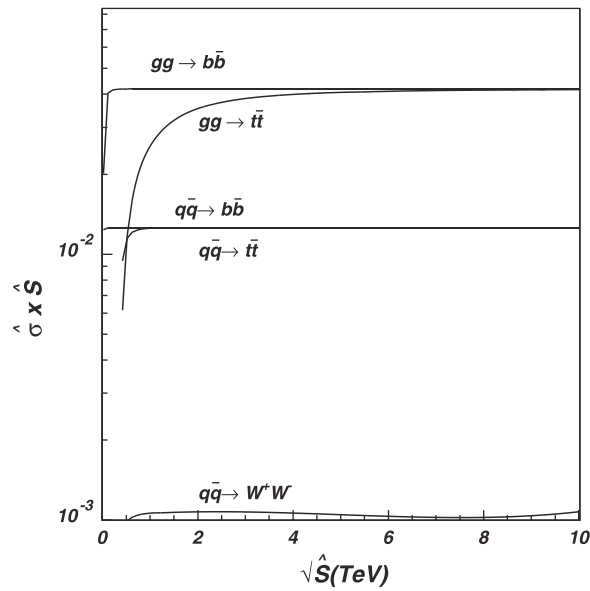

Figure 71. Parton level cross sections $\left(\hat{s}\hat{\sigma}_{ij} \right)$ for various processes involving massive partons in the final state.
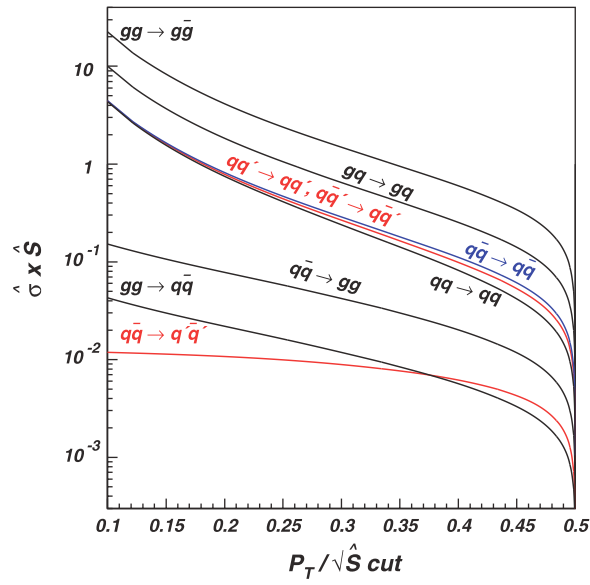
Figure 72. Parton level cross sections $\left(\hat{s}\hat{\sigma}_{ij}\right)$ for various processes involving massless partons in the final state as a function of the variable $p_T/\sqrt{\hat{s}}$.

Figure 73. Parton level cross sections $\left(\hat{s}\hat{\sigma}_{ij}\right)$ for various processes involving massive partons in the final state as a function of the variable $p_T/\sqrt{\hat{s}}$. The calculations were performed for $\sqrt{\hat{s}} = 2\,\text{TeV}$, in the region where $\hat{\sigma}\hat{s}$ has a relatively flat behaviour with $\sqrt{\hat{s}}$.
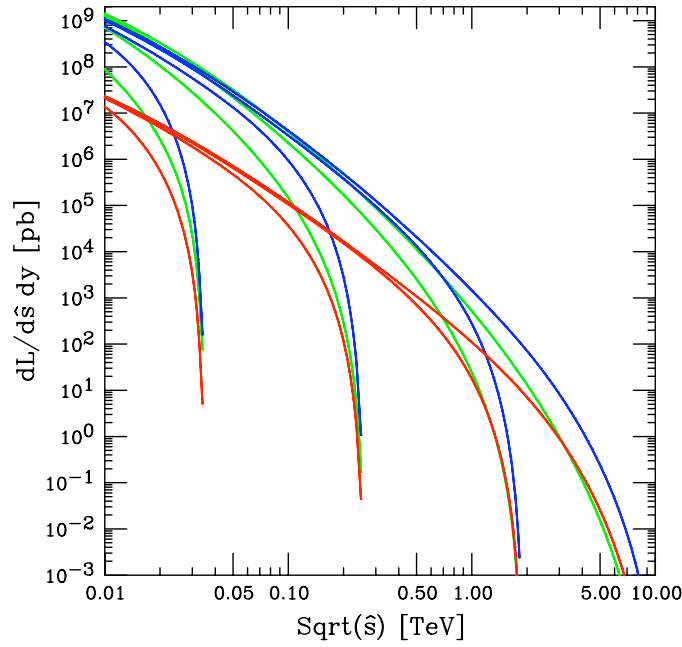
Figure 74. d(Luminosity)/dy at rapidities (right to left) $y = 0, 2, 4, 6$. Green=gg, Blue=$\sum_i (gq_i + g\bar{q}_i + q_i g + \bar{q}_i g)$, Red=$\sum_i (q_i \bar{q}_i + \bar{q}_i q_i)$, where the sum runs over the five quark flavours d, u, s, c, b.

combinations of initial-state partons. One can read from the curves the parton–parton luminosity for a specific value of mass fraction and rapidity. (It is also easy to use the Durham pdf plotter to generate the pdf curve for any desired flavour and kinematic configuration[20].)

It is also of great interest to understand the uncertainty in the parton–parton luminosity for specific kinematic configurations. Some representative parton–parton luminosity uncertainties, integrated over rapidity, are shown in figures 75–77. The pdf uncertainties were generated from the CTEQ6.1 Hessian error analysis using the standard $\Delta\chi^2 = 100$ criterion. Except for kinematic regions where one or both partons is a gluon at high x, the pdf uncertainties are of the order of 5–10%. Luminosity uncertainties for specific rapidity values are available at the SM benchmark website. Even tighter constraints will be possible once the LHC Standard Model data is included in the global pdf fits. Again, the uncertainties for individual pdfs can also be calculated online using the Durham pdf plotter. Often it is not the pdf uncertainty for a cross section that is required, but rather the pdf uncertainty for an acceptance for a given final state. The acceptance for a particular process may depend on the input pdfs due to the rapidity cuts placed on the jets, leptons, photons, etc and the impacts of the varying longitudinal boosts of the final state caused by the different pdf pairs. An approximate 'rule-of-thumb' is that the pdf uncertainty for the acceptance is a factor of 5–10 times smaller than the uncertainty for the cross section itself.

In figure 78, the pdf luminosity curves shown in figure 69 are overlaid with equivalent luminosity curves from the Tevatron. In Figure 79, the ratios of the pdf luminosities at the LHC to those at the Tevatron are plotted. The most dramatic increase in pdf luminosity at the LHC comes from gg initial-states, followed by gq initial-states and then $q\bar{q}$ initial-states. The latter ratio is smallest because of the availability of valence antiquarks at the Tevatron at
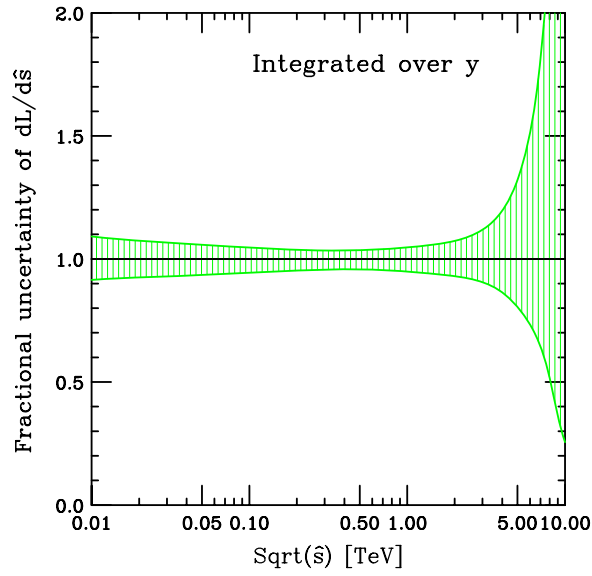
[20] http://durpdg.dur.ac.uk/hepdata/pdf3.html
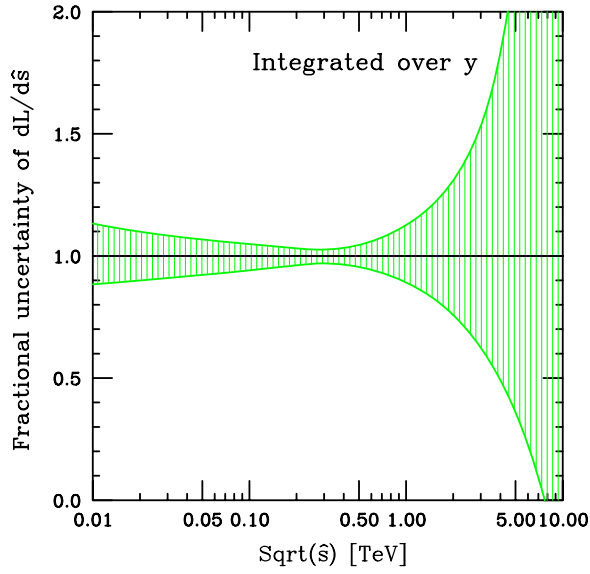
**Figure 75.** Fractional uncertainty of the gg luminosity integrated over y.
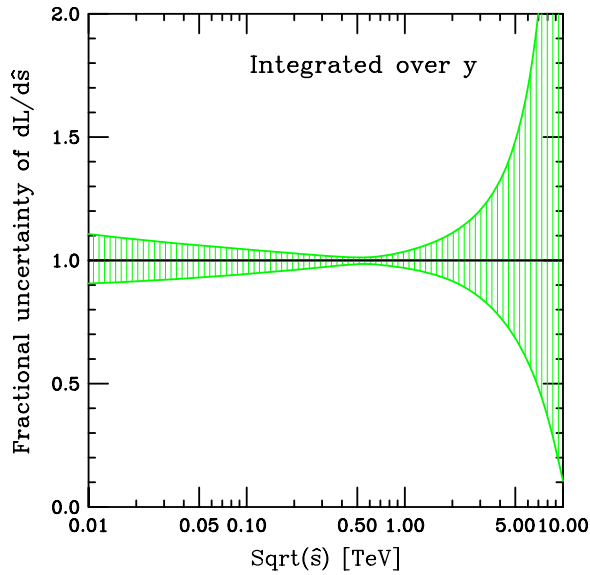
Figure 76. Fractional uncertainty for the parton-parton luminosity integrated over y for $\sum_i (q_i \bar{q}_i + \bar{q}_i q_i)$, where the sum runs over the five quark flavours d, u, s, c, b.

moderate to large x. As an example, consider chargino pair production with $\sqrt{\hat{s}} = 0.4$ TeV. This process proceeds through $q\bar{q}$ annihilation; thus, there is only a factor of 10 enhancement at the LHC compared with the Tevatron.

Backgrounds to interesting physics at the LHC proceed mostly through gg and gq initial-states. Thus, there will be a commensurate increase in the rate for background processes at the LHC.

Figure 77. Fractional uncertainty for the luminosity integrated over y for $\sum_i (q_i \bar{q}_i + \bar{q}_i q_i)$, where the sum runs over the five quark flavours d, u, s, c, b.
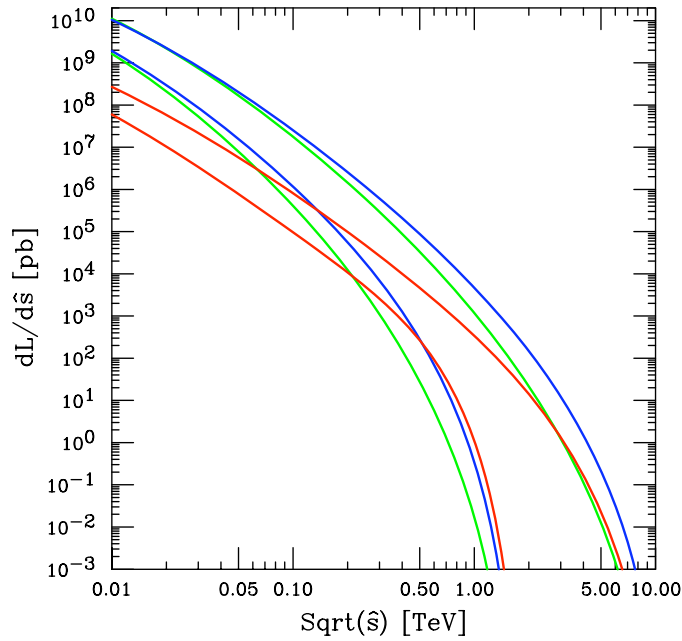
Figure 78. The parton–parton luminosity $\left[\frac{1}{\hat{s}} \frac{dL_{ij}}{d\tau} \right]$ in pb integrated over y. Green = gg, Blue = $\sum_i (g q_i + g \bar{q}_i + q_i g + \bar{q}_i g)$, Red = $\sum_i (q_i \bar{q}_i + \bar{q}_i q_i)$, where the sum runs over the five quark flavours d, u, s, c, b. The top family of curves are for the LHC and the bottom for the Tevatron.
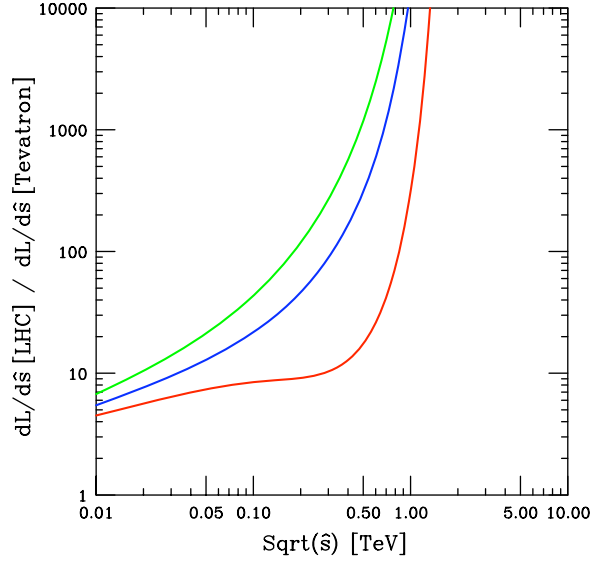
Figure 79. The ratio of parton–parton luminosity $\left[\frac{1}{\hat{s}}\frac{\mathrm{d}L_{ij}}{\mathrm{d}\tau}\right]$ in pb integrated over y at the LHC and Tevatron. Green=gg (top), Blue=$\sum_i(gq_i + g\bar{q}_i + q_i g + \bar{q}_i g)$ (middle), Red=$\sum_i(q_i\bar{q}_i + \bar{q}_i q_i)$ (bottom), where the sum runs over the five quark flavours d, u, s, c, b.
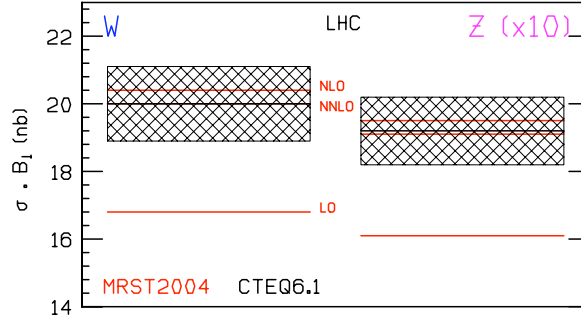

Figure 80. Predicted cross sections for W and Z production at the LHC using MRST2004 and CTEQ6.1 pdfs. The overall pdf uncertainty of the NLO CTEQ6.1 prediction is approximately 5%, consistent with figure 77.

6.3. Stability of NLO global analyses

The W and Z cross sections at the LHC are shown in figure 80. The MRST2004 predictions are shown at LO, NLO and NNLO; also shown are the CTEQ6.1 predictions at NLO, along with the CTEQ6.1 pdf error band. There is a significant increase in cross section when going from LO to NLO, and then a small decrease when going from NLO to NNLO. The NLO MRST2004 and CTEQ6.1 predicted cross sections agree with each other, well within the CTEQ6.1 pdf uncertainty band.

Most of the absolute predictions for LHC observables have been carried out at NLO, i.e. with NLO pdfs and with NLO matrix elements. Such predictions have worked well at the Tevatron, but the LHC explores a new region of (small) x for a hadron–hadron collider. Thus, it is important to understand whether the NLO formalism carries over to the LHC with
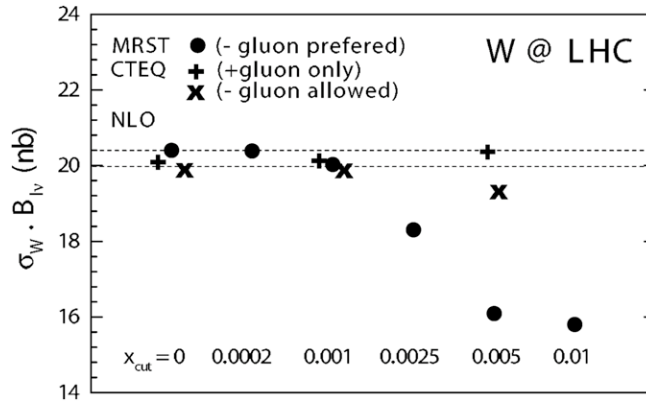
Figure 81. Predicted total cross section of $W^+ + W^-$ production at the LHC for the fits obtained
in the CTEQ stability study, compared with the MRST results. The overall pdf uncertainty of the
prediction is ∼5%, as observed in figure 77.

the same degree of accuracy. In recent years, some preliminary next-to-next-leading-order
global pdf analyses have been carried out either for DIS alone [151], or in a global analysis
context [153]. The differences with respect to the corresponding NLO analyses are reasonably
small. However, most observables of interest (including inclusive jet production) have not yet
been calculated at NNLO.

   All other considerations being equal, a global analysis at NNLO must be expected to have a
higher accuracy. However, NLO analyses can be adequate as long as their accuracy is sufficient
for the task, and as long as their predictions are stable with respect to certain choices inherent
in the analysis. Examples of those choices are the functional forms used to parametrize the
initial non-perturbative parton distribution functions, and the selection of experimental data
sets included in the fit—along with the kinematic cuts that are imposed on that data. In a recent
MRST analysis [152], a 20% variation in the cross section predicted for W production at the
LHC—a very important 'standard candle' process for hadron colliders—was observed when
data at low x and Q^2 were removed from the global fit. This is a fundamental consideration,
since the presence of this instability would significantly impact the phenomenology of a wide
range of physical processes for the LHC. The instability was removed in the same study when
the analysis was carried out at NNLO.

   A similar study was also carried out by the CTEQ collaboration in which this instability was
not observed, and the predictions for the W cross section at the LHC remained stable (but with
increased uncertainties) when more severe low (x, Q^2) kinematic cuts were performed [154].
The predicted cross sections, as a function of the x cut on the data removed, are shown in
figure 81 for the two studies. In figure 82, the uncertainty on the predictions for the W cross
section at the LHC is shown from a study that uses the Lagrange Multiplier Method. As more
data are removed at low x and Q^2, the resulting uncertainty on the predicted W cross section
increases greatly. If the gluon is parametrized in a form that allows it to become negative at
low x, such as the parametrization that MRST used, then the uncertainty becomes even larger,
especially for the lower range of the cross section.

6.4. The future for NLO calculations

Unfortunately, our ability to take advantage of the benefits of NLO predictions is severely
limited by the calculations available. Currently, no complete NLO QCD calculation exists for
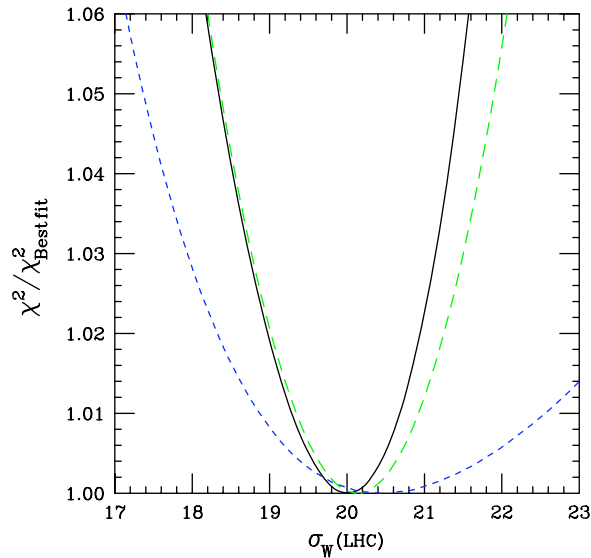
Figure 82. Lagrange multiplier results for the *W* cross section (in nb) at the LHC using a positive–definite gluon. The three curves, in order of decreasing steepness, correspond to three sets of kinematic cuts, standard/intermediate/strong.

a process involving more than 5 particles. This means that we are limited to the consideration of scenarios such as 4 jet production at LEP (effectively a $1 \rightarrow 4$ process) and a number of $2 \rightarrow 3$ processes of interest at hadron colliders.

The bottleneck for these calculations is the evaluation of the loop diagrams. The real radiation component consists of the evaluation of known lowest-order matrix elements combined with a method for systematically removing their singularities, several of which are well-understood. In contrast, the evaluation of the virtual contribution must at present be performed on a case-by-case basis. Even the most basic integral that can appear depends non-trivially on the number of external legs in the loop, as well as on the masses of all the external and internal particles. To complicate matters further, the presence of powers of loop momenta in the integrals (from fermion propagators or multi-gluon vertices) leads to 'tensor integrals' which typically are expressed as the sum of many terms. Taken all together, this means that traditional methods based on an analytical Feynman diagram approach are already limited by the computing power currently available. It seems unlikely that further progress, such as the NLO calculation of a $2 \rightarrow 4$ process, will be made in this fashion.

An alternative to this brute-force Feynman diagram approach is provided by 'unitarity-based' methods, which are based on sewing together tree-level amplitudes (for a review, see [155]). These methods rely on the Cutkosky rules to generate the 1-loop amplitude by summing over all possible cuts of sewn-together tree amplitudes. Although this knowledge in itself only suffices for sufficiently supersymmetric theories, results for 1-loop amplitudes in non-supersymmetric theories (such as QCD) can be obtained by consideration of the collinear limits of the amplitudes. Such techniques were used to obtain relatively compact expressions for the 1-loop amplitudes required to evaluate the process $e^+e^- \rightarrow 4$ partons [52].

More recently the 'twistor-inspired' methods, which have proven so efficient at generating compact expressions for tree-level amplitudes, have been considered at the 1-loop level [156]. The MHV rules (discussed in section 3.2.3) were shown to reproduce known results at the

1-loop level [157] and their application has passed from calculations in $N = 4$ supersymmetric Yang–Mills theory to the evaluation of amplitudes in QCD ([158] and references therein). Similarly, the on-shell recursion relations have proven equally useful at 1-loop [159], even allowing for the calculation of MHV amplitudes involving an arbitrary number of gluons [160]. These methods will doubtless be refined and extended to more complicated calculations over time.

An alternative path to 1-loop amplitudes is provided by numerical approaches. Such techniques have long been applied at lowest order, with the main attraction deriving from the promise of a generic solution that can be applied to any process (given sufficient computing power). The techniques are generally either completely numerical evaluations of loop integrals [161,162], or they are semi-numerical approaches that perform only the tensor integral reductions numerically [163–168]. In most cases these algorithms have only been applied to individual integrals or diagrams, although one recent application evaluates the 1-loop matrix elements for the Higgs+4 parton process (which is otherwise uncalculated) [169][21]. Once more, the study of these approaches is in its infancy and the coming years promise significant further development.

It should also be noted that many of the recent simplifying techniques and numerical approaches have concentrated on processes involving gluons and massless quarks. Although this is sufficient for many hadron collider applications, there are many processes for which a calculation which includes the quark mass is necessary. The top quark mass must clearly be taken into account and, in addition, the experimental ability to identify b-quarks in events often demands that the mass of the bottom quark is included. When including the mass, the evaluation of Feynman diagrams becomes much more complicated and the expressions for amplitudes do not simplify as conveniently. However, the presence of an additional hard scale renders the loop amplitudes less infrared divergent, so that some numerical approaches may in fact benefit from the inclusion of quark masses. Due to the large role of the top quark in much of the LHC programme, advances on this front are to be expected in the near future.

6.5. A realistic NLO wishlist for multi-parton final states at the LHC

A somewhat whimsical experimenter's *wishlist* was first presented at the Run 2 Monte Carlo workshop at Fermilab in 2001[22]. Since then the list has gathered a great deal of notoriety and has appeared in numerous LHC-related theory talks. It is unlikely that $WWW + b\bar{b} + 3$ jets will be calculated at NLO soon, no matter the level of physics motivation, but there are a number of high priority calculations, primarily of backgrounds to new physics, that are accessible with the present technology. However, the manpower available before the LHC turns on is limited. Thus, it is necessary to prioritize the calculations, both in terms of the importance of the calculation and the effort expected to bring it to completion.

A prioritized list, determined at the Les Houches 2005 Workshop, is shown in table 2, along with a brief discussion of the physics motivation. Note that the list contains only $2 \rightarrow 3$ and $2 \rightarrow 4$ processes, as these are feasible to be completed by the turn-on of the LHC.

First, a few general statements: in general, signatures for new physics will involve high p_T leptons and jets (especially b jets) and missing transverse momentum. Thus, backgrounds to new physics will tend to involve (multiple) vector boson production (with jets) and $t\bar{t}$ pair production (with jets). The best manner in which to understand the normalization of a cross section is to measure it; however the rates for some of the complex final states listed here may be limited and (at least in the early days) must be calculated from NLO theory. As discussed

---

[21] All partons are treated as outgoing so this process corresponds to a Higgs+2 parton final state.
[22] http://vmsstreamer1.fnal.gov/Lectures/MonteCarlo2001/Index.htm

Table 2. The wishlist of processes for which a NLO calculation is both desired and feasible in the near future.

Process ($V \in \{Z, W, \gamma\}$)	Relevant for
1. $pp \to VV+$jet	$t\bar{t}H$, new physics
2. $pp \to H + 2$ jets	H production by vector boson fusion (VBF)
3. $pp \to t\bar{t}b\bar{b}$	$t\bar{t}H$
4. $pp \to t\bar{t} + 2$ jets	$t\bar{t}H$
5. $pp \to VVb\bar{b}$	VBF$\to H \to VV$, $t\bar{t}H$, new physics
6. $pp \to VV + 2$ jets	VBF$\to H \to VV$
7. $pp \to V + 3$ jets	Various new physics signatures
8. $pp \to VVV$	SUSY trilepton searches

at length previously, NLO is the first order at which both the normalization and shape can be calculated with any degree of confidence.

We now turn to a detailed look at each of these processes:

- $pp \to VV$ + jet: one of the most promising channels for Higgs boson production in the low mass range is through the $H \to WW^*$ channel, with the W's decaying semi-leptonically. It is useful to look both in the $H \to WW$ exclusive channel, along with the $H \to WW$+jet channel. The calculation of $pp \to WW$+jet will be especially important in understanding the background to the latter.
- $pp \to H + 2$ jets: a measurement of vector boson fusion (VBF) production of the Higgs boson will allow the determination of the Higgs coupling to vector bosons. One of the key signatures for this process is the presence of forward–backward tagging jets. Thus, QCD production of $H + 2$ jets must be understood, especially as the rates for the two are comparable in the kinematic regions of interest.
- $pp \to t\bar{t}b\bar{b}$ and $pp \to t\bar{t} + 2$ jets: both of these processes serve as background to $t\bar{t}H$, where the Higgs boson decays into a $b\bar{b}$ pair. The rate for $t\bar{t}jj$ is much greater than that for $t\bar{t}b\bar{b}$ and thus, even if 3 b-tags are required, there may be a significant chance for the heavy flavour mistag of a $t\bar{t}jj$ event to contribute to the background.
- $pp \to VVb\bar{b}$: Such a signature serves as a non-resonant background to $t\bar{t}$ production as well as to possible new physics.
- $pp \to VV + 2$ jets: the process serves as a background to VBF production of a Higgs boson.
- $pp \to V + 3$ jets: the process serves as background to $t\bar{t}$ production where one of the jets may not be reconstructed, as well as for various new physics signatures involving leptons, jets and missing transverse momentum.
- $pp \to VVV$: the process serves as a background to various new physics subprocesses such as SUSY trilepton production.

Work on (at least) the processes 1–4 of table 2 is already in progress by several groups, and clearly all of them aim at a setup which allows for a straightforward application to other processes[23].

From an experimentalist's point-of-view, the NLO calculations discussed thus far may be used to understand changes in normalization and/or shape that occur for a given process when going from LO to NLO [139]. As discussed previously, direct comparisons to the data require

[23] Process 2 has been calculated since the first version of this list was formulated [138].
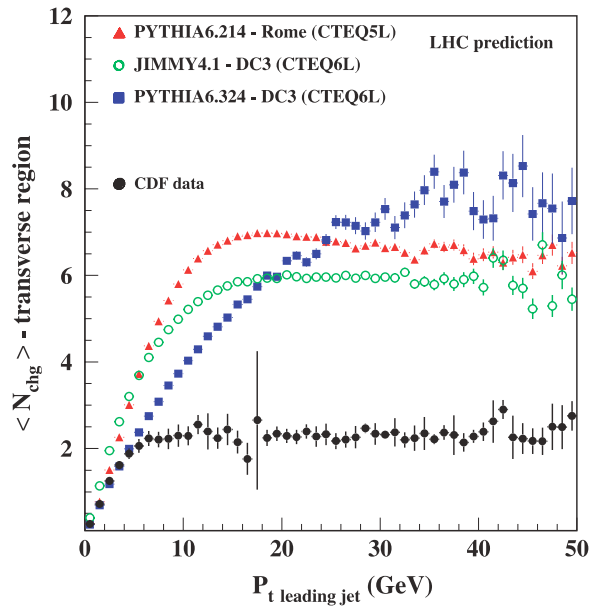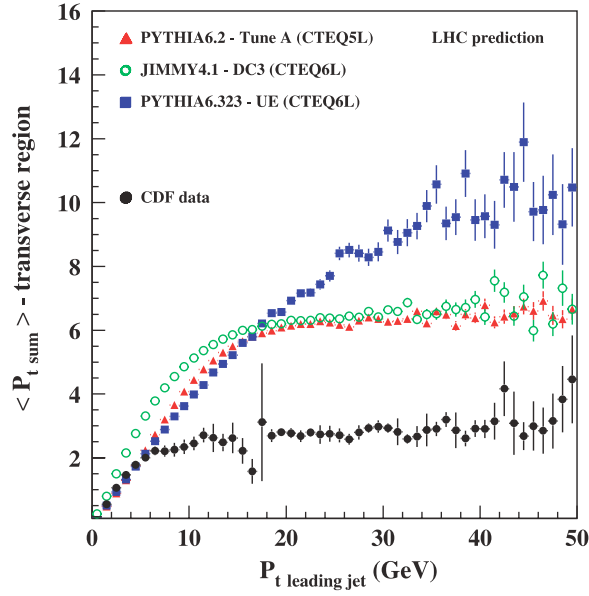
Figure 83. PYTHIA6.2 - Tune A, Jimmy4.1 - UE and PYTHIA6.323 - UE predictions for the average charged multiplicity in the transverse region in the underlying event for LHC *pp* collisions.

either a determination of parton-to-hadron corrections for the theory or hadron-to-parton corrections for the data [170]. Furthermore, for multi-parton final states it is also necessary to model the effects of jet algorithms, when two or more partons may be combined into one jet.

6.6. Some Standard Model cross sections for the LHC

Here we discuss some of the Standard Model benchmark cross sections at the LHC. A lack of space will keep the discussion short, but a more complete treatment can be found at the benchmark website and also in the CMS [147] and ATLAS [148] Physics Technical Design Reports.

6.6.1. Underlying event at the LHC. As discussed in section 2, hard interactions at hadron–hadron colliders consist of a hard collision of two incoming partons along with softer interactions from the remaining partons in the colliding hadrons ('the underlying event energy'). The underlying event will affect almost all measurements of physics processes at the LHC. Some predictions for the underlying event charged multiplicities and charged momentum sum (defined in section 5) at the LHC are shown in figures 83 and 84. It is clear that (1) all predictions lead to a substantially larger charged particle multiplicity and charged particle momentum sum at the LHC than at the Tevatron and (2) there are large differences among the predictions from the various models. Investigations are continuing, trying to reduce the energy extrapolation uncertainty of these models. This measurement will be one of the first to be performed at the LHC during the commissioning run in 2008 and will be used for subsequent Monte Carlo tunings for the LHC.

Figure 84. PYTHIA6.2 - Tune A, Jimmy4.1 - UE and PYTHIA6.323 - UE predictions for the average sum of the transverse momenta of charged particles in the transverse region in the underlying event for LHC *pp* collisions.

6.6.2. W/Z production. The stability and pdf uncertainties for NLO *W* production at the LHC have been previously discussed. It is interesting to examine the pdf uncertainties of other processes at the LHC in relation to the pdf uncertainty for *W* production. The understanding gained may help to reduce the theoretical uncertainties for these processes.

In figure 85, we present cross section predictions for *Z* production at the LHC, calculated using the 41 CTEQ6.1 pdfs. The cross section for *Z* production at the LHC is highly correlated with the cross section for *W* production. Both are sensitive to the low *x* quark pdfs, at a similar *x* value, which are driven by the gluon distribution at a slightly higher *x* value.
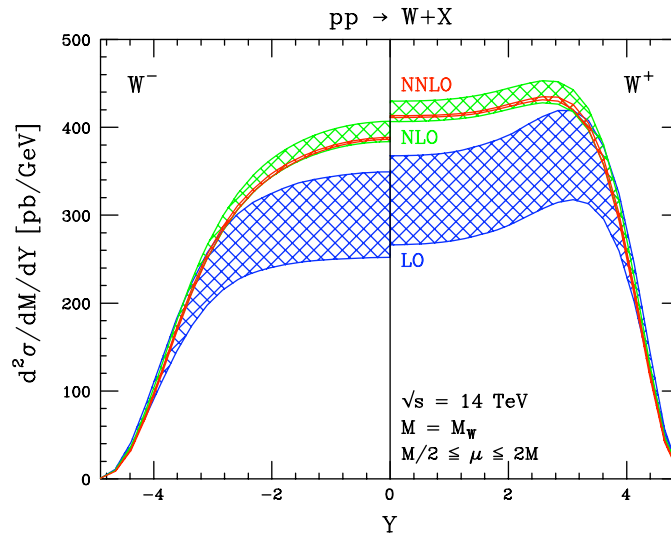
The rapidity distributions for W^+ and W^- production at LO, NLO and NNLO are shown in figure 86, while similar distributions for the *Z* are shown in figure 87. The widths of the curves indicate the scale uncertainty for the cross section predictions. As for the inclusive *W* and *Z* cross sections, the scale dependence greatly decreases from LO to NLO to NNLO. There is a sizeable increase in the cross sections from LO to NLO, and a slight decrease (and basically no change in shape) in the cross sections from NLO to NNLO. The change from NLO to NNLO is within the NLO scale uncertainty band. As discussed in section 4, the NNLO pdfs are still somewhat incomplete due to the lack of inclusion of inclusive jet production in the global fits. Although this is formally mixing orders, the result of using the NNLO matrix element with NLO pdfs for calculation of the *Z* rapidity distribution is shown in figure 88. The predictions are similar as expected, but the prediction using the NLO pdfs is outside the (very precise) NNLO error band[24].

The transverse momentum distributions for *W* and *Z* production at the LHC are also important to understand. *Z* production will be one of the Standard Model benchmark processes during the early running of the LHC. At low transverse momenta, the distributions are dominated by the effects of multiple soft gluon emission, while at higher p_T, hard gluon

[24] We would like to thank Lance Dixon for providing these curves.
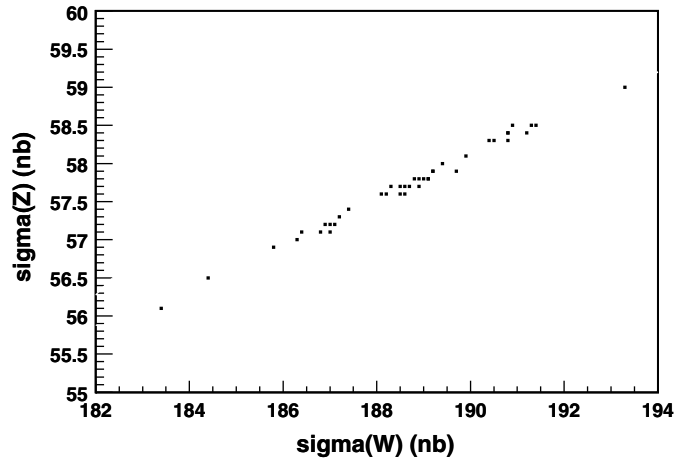
Figure 85. The cross section predictions for *Z* production versus the cross section predictions for *W* production at the LHC plotted using the 41 CTEQ6.1 pdfs.
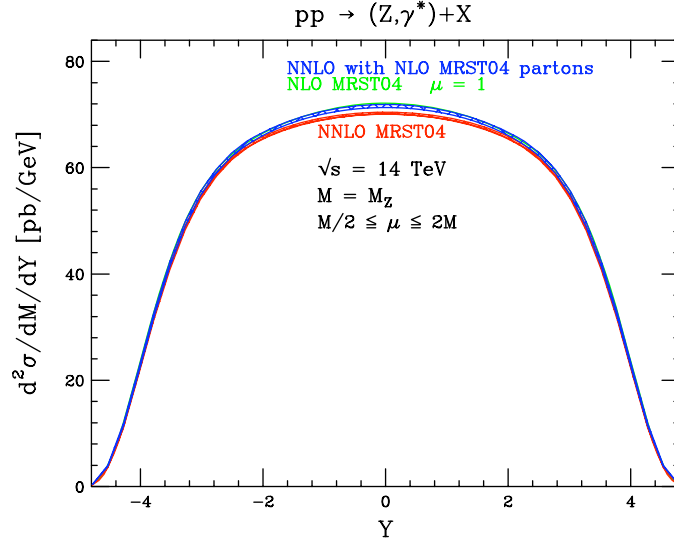

Figure 86. The rapidity distributions for W^+ and W^- production at the LHC at LO, NLO and NNLO.

emission is the major contribution. In figure 89, the *Z* p_T distributions at the Tevatron and LHC are shown using predictions from ResBos. The transverse momentum distribution at the LHC is similar to that at the Tevatron, although somewhat enhanced at moderate transverse momentum values. There is a larger phase space for gluon emission of incident quarks at $x = 0.007$ (*Z* production at the LHC) than for incident quarks at $x = 0.05$ (*Z* production at the Tevatron) and the enhancement at moderate transverse momentum is a result of this. There is still substantial influence of the non-perturbative component of the parton transverse momentum near the peak region of the *Z* transverse momentum distribution [171].

An analysis of semi-inclusive deep-inelastic scattering hadroproduction suggests a broadening of transverse momentum distributions for *x* values below 10^{-3}–10^{-2} [173].
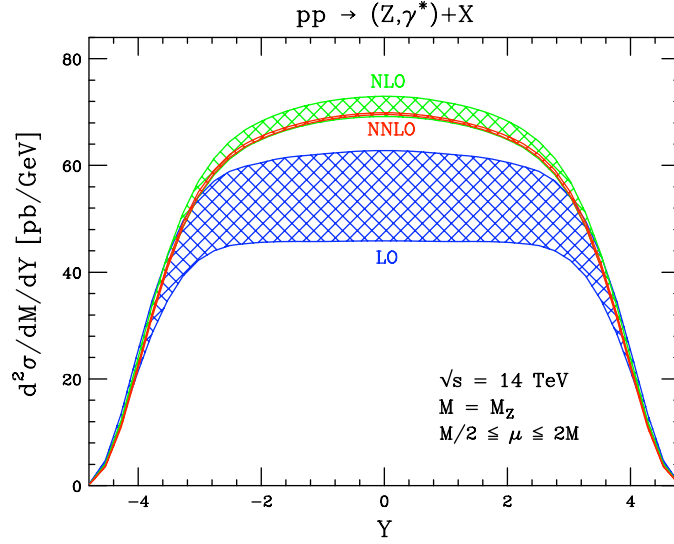
**Figure 87.** The rapidity distributions for Z production at the LHC at LO, NLO and NNLO.

Figure 88. The rapidity distributions for Z production at the LHC at NNLO calculated with NNLO and with NLO pdfs.

(See also the discussion in section 6.6.3.) The p_T broadening at small x may be due to x-dependent higher-order contributions (like BFKL [174–177]) not included in current resummation formalisms. Such contributions are important when $\log Q^2 \ll \log(1/x)$. The BFKL formalism resums terms proportional to $\alpha_S \log(1/x)$, retaining the full Q^2 dependence. The BFKL corrections would have a small impact at the Tevatron (except perhaps for W/Z production in the forward region) but may affect the predictions for W/Z/Higgs p_T distributions for all rapidity regions at the LHC. The p_T broadening can be modelled in the Collins–Soper–Sterman formalism [172] by a modification of the impact parameter-dependent parton densities.
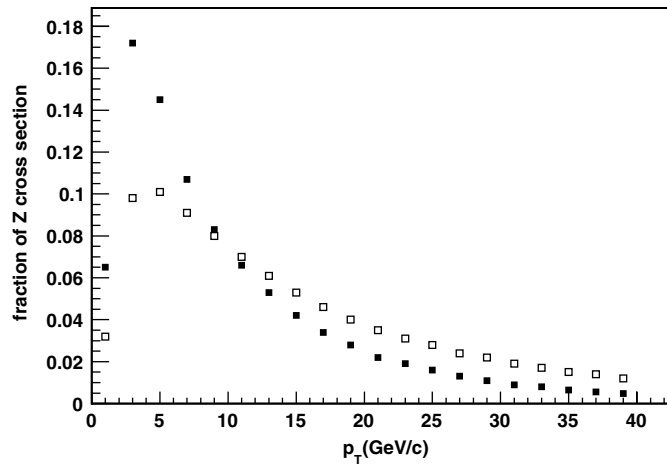
Figure 89. Predictions for the transverse momentum distributions for Z production at the Tevatron (solid squares) and LHC (open squares).
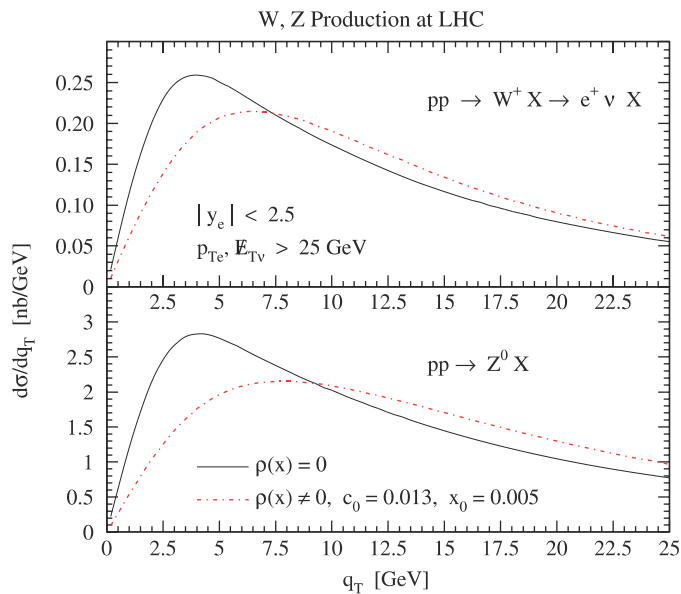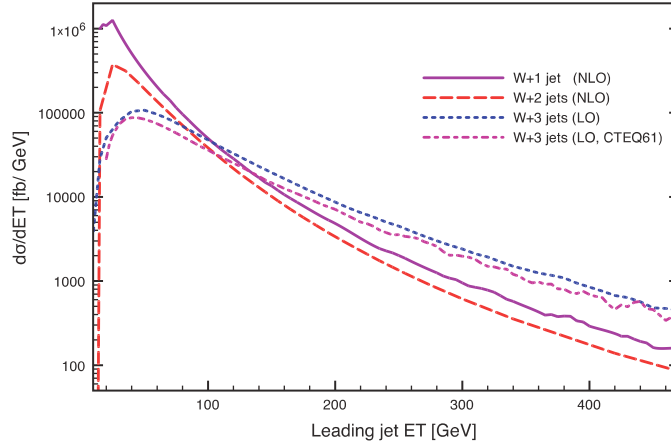

Figure 90. The predictions for the transverse momentum distributions for W and Z production with and without the p_T-broadening effects.

The p_T shifts for the W and Z transverse momentum distributions at the LHC are shown in figure 90 [178]. The observed shifts would have important implications for the measurement of the W boson mass and a measurement of the W/Z p_T distributions will be one of the important early benchmarks to be established at the LHC.

6.6.3. W/Z+ jets. Next we consider the production of W/Z+ jets at the LHC. In figure 91, the rate of production of $W+ \geqslant 1, 2, 3$ jets at the LHC is shown as a function of the transverse
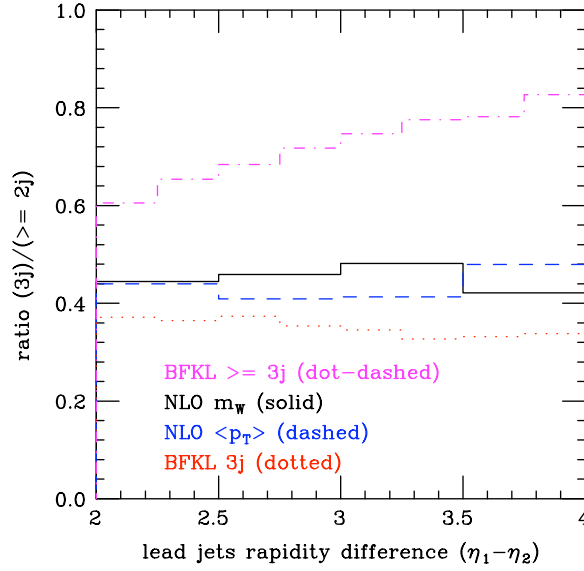
Figure 91. Predictions for the production of $W+ \geqslant 1, 2, 3$ jets at the LHC shown as a function of the transverse energy of the lead jet. A cut of 20 GeV has been placed on the other jets in the prediction.

energy of the lead jet (calculated using the MCFM programme). The rate for 3 jet production is actually larger than the rate for 1 or 2 jet production for large lead jet transverse energy due to the Sudakov effects discussed throughout this paper. We also show the rate for $W + 3$ jet production (a LO calculation in MCFM) using both CTEQ6L1 (a leading-order pdf) and CTEQ6.1 (a NLO pdf). The rate using the LO pdf is larger due to (1) the importance of the gluon distribution for production of $W + 3$ jet final states and (2) the larger small x gluon present in the LO pdf compared with the NLO pdf.

In figure 92, we show the rate for production of a third jet given a $W+ \geqslant 2$ jet event, as a function of the rapidity separation of the two leading jets. (As a reminder, the production of Z plus two jets widely separated in rapidity serves as a background to VBF production of a Higgs.) In section 5.4, the corresponding measurement at the Tevatron was compared to predictions from MCFM and found to be bounded by the two predictions at scales of m_W and the average jet p_T. At the LHC, we note that the rate for emission of a third jet is considerably enhanced compared with the Tevatron (even though the p_T cut is larger, 20 GeV compared with 15 GeV at the Tevatron) and is reasonably flat as a function of the two lead jets rapidity separation. The scale dependence is also observed to be smaller than at the Tevatron. Predictions for this rate are also available using the BFKL formalism. The BFKL formalism has potentially large logarithms proportional to the rapidity separation of the two lead jets. The resultant ratio in figure 92 for exactly 3 jets is also flat, slightly below the prediction from MCFM but the ratio for greater than or equal to 3 jets in the BFKL formalism is appreciably larger and rises with the rapidity separation of the lead jets [145, 146][25]. There is a sizeable production of 4, 5 and larger number of jets in the final state. It is expected that next-to-leading logarithmic (NLL) corrections may somewhat dampen the growth in the jet multiplicity predicted by the BFKL formalism as the tagging jet separation increases. As discussed in the previous section, early measurements such as these will establish in what kinematic regions BFKL effects are important at the LHC, and what kinematic regions can be well described by the DGLAP formalism alone.

[25] We thank Jeppe Andersen for providing us with the BFKL predictions.

Figure 92. The rate for production of a third (or more) jet in $W+ \geqslant 2$ jet events as a function of the rapidity separation of the two leading jets. A cut of 20 GeV has been placed on all jets. Predictions are shown from MCFM using two values for the renormalization and factorization scale, and using the BFKL formalism, requiring either that there be exactly 3 jets or 3 or more jets.

6.6.4. Top quark production. As at the Tevatron, $t\bar{t}$ production at the LHC proceeds through both $q\bar{q}$ and gg initial-states. Consider a specific value of $\sqrt{\hat{s}}$ of 0.4 TeV (near $t\bar{t}$ threshold); from figure 79, the $q\bar{q}$ annihilation component is only a factor of 10 larger at the LHC than at the Tevatron. The gg component, on the other hand, is over a factor of 500 larger, leading to (1) the large dominance of gg scattering for top pair production at the LHC, in contrast to the situation at the Tevatron and (2) a total $t\bar{t}$ cross section a factor of 100 larger than at the Tevatron. Interestingly, as shown in figure 93, the cross section for $t\bar{t}$ production is anti-correlated with the W cross section. An increase in the W cross section is correlated with a decrease in the $t\bar{t}$ cross section and vice versa. This is due to the dominance of the gg fusion subprocess for $t\bar{t}$ production, while W production is still predominantly quark–antiquark. An increase in the gluon distribution in the x range relevant for $t\bar{t}$ production leads to a decrease in the quark distributions in the (lower) x range relevant for W production. In fact, the extremes for both cross sections are produced by CTEQ6.1 eigenvector 5 (pdfs 9 and 10) which is most sensitive to the low x behaviour of the gluon distribution.

The ratio of the NLO to LO predictions for $t\bar{t}$ production at the LHC is shown in figure 94. In contrast to the Tevatron, the NLO cross section is larger than the LO one by an approximately constant factor of 1.5. We also plot the NLO/LO ratio specifically for the $q\bar{q}$ initial-state where we observe a behaviour similar to that observed at the Tevatron, but not as pronounced.

It is also evident that because of the higher percentage of gg production and the lower average x of the incident partons, the jet multiplicity will be significantly higher for $t\bar{t}$ production at the LHC than at the Tevatron. Consider the production of a pair of top quarks in association with an additional jet at the LHC. Defining the cross section for this process to only include events with a jet of transverse momentum greater than some minimum value, $p_{T,\mathrm{min}}$, yields the dependence on $p_{T,\mathrm{min}}$ shown in figure 95. The reason for this behaviour is discussed at length in section 3.2. Overlaid on this figure is the cross section for top pair production at
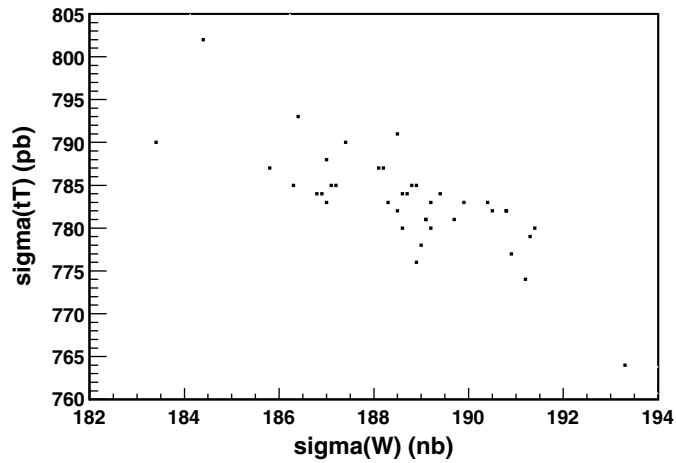
Figure 93. The cross section predictions for $t\bar{t}$ production versus the cross section predictions for W production at the LHC plotted using the 41 CTEQ6.1 pdfs.
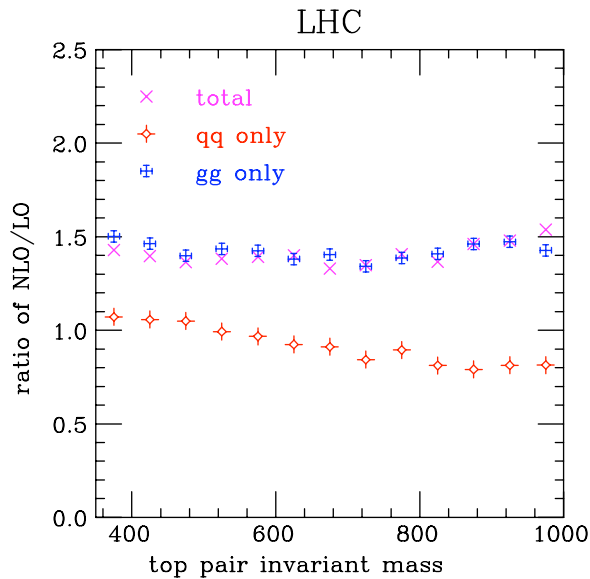

Figure 94. The ratio of the NLO to LO predictions for the $t\bar{t}$ mass at the LHC. The predictions include the ratio for the total cross section and for the specific $q\bar{q}$ and gg initial-states. Note that the total also includes a gq contribution (not present at LO).

LO and NLO, which clearly has no dependence on the parameter $p_{T,\min}$. As the minimum jet transverse momentum is decreased the cross section for $t\bar{t}$+jet production increases rapidly and in fact saturates the total LO $t\bar{t}$ cross section at around 28 GeV. On the one hand, this appears to be a failing of the leading-order predictions. When the $t\bar{t}$ rate is calculated at NLO the cross section increases and the saturation does not occur until around 18 GeV (and presumably higher orders still would relax it further). On the other hand transverse momenta of this size, around 20 GeV, are typical values used to define jets in the LHC experiments. Based on these
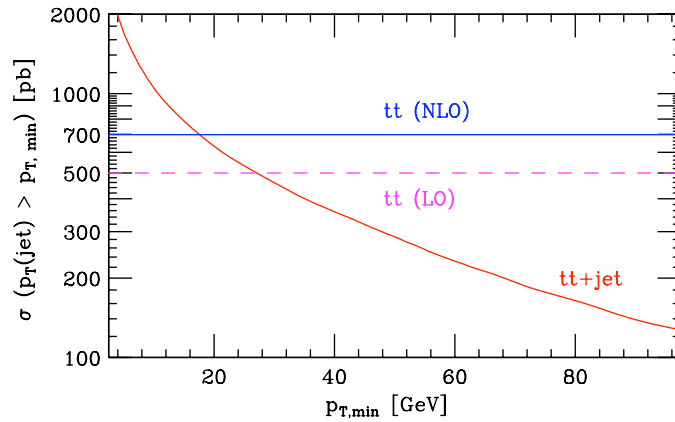
Figure 95. The dependence of the LO $t\bar{t}$+jet cross section on the jet-defining parameter $p_{T,\min}$, together with the top pair production cross sections at LO and NLO.
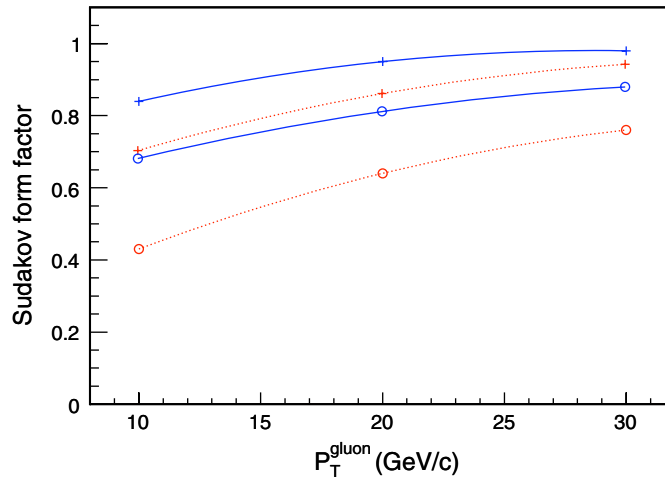
Figure 96. The Sudakov form factors for initial-state quarks and gluons at a hard scale of 200 GeV as a function of the transverse momentum of the emitted gluon. The form factors are for quarks (blue-solid) and gluons (red-dashed) at parton x values of 0.3 (crosses) and 0.03 (open circles).

results, one might certainly expect that jets of these energies might often be found in events containing top quark pairs at the LHC.

Another way of estimating the probability for extra jets is to look at the Sudakov form factors for the initial-state partons. It is interesting to compare the Sudakov form factors for $t\bar{t}$ production at the Tevatron and LHC. At the Tevatron, $t\bar{t}$ production proceeds primarily (85%) through $q\bar{q}$ with gg being responsible for 15%, with the partons evaluated near an average x value of 0.3. At the LHC, the percentages are roughly reversed (or more precisely 90% for gg) and the scattering takes place at an average x value of a factor of 7 lower (which we approximate here as $x = 0.03$). The relevant Sudakov form factors are shown in figure 96, as a function of the minimum transverse momentum of the emitted gluon, at a hard scale of 200 GeV (roughly appropriate for $t\bar{t}$ production). We can make some rough estimates from these plots. The probability for no gluon of 10 GeV or greater to be radiated from an initial

quark leg with $x = 0.3$ is 0.85. The probability for no such gluon to be radiated from either quark leg at the Tevatron is $0.85 \times 0.85 = 0.72$, i.e. a 0.28 chance of radiating such a gluon. A similar exercise for two incident gluons of $x = 0.3$ gives a chance of radiating a 10 GeV gluon of 0.51. As the $q\bar{q}$ initial-state makes up 85% of the Tevatron cross section, with gg only 15%, the total probability of emitting at least one 10 GeV gluon is 0.3. Using 90% for gg at the LHC and 10% for $q\bar{q}$, gives a 0.8 probability of radiating such a hard gluon.

The W+jets background to $t\bar{t}$ production proceeds primarily through the gq channel and so receives a factor of 500 enhancement. Thus, the signal-to-background ratio for $t\bar{t}$ production in a lepton + jets final state is significantly worse at the LHC than at the Tevatron, if the same cuts on the jet transverse momenta as at the Tevatron are used. Thus, the jet cuts applied to $t\bar{t}$ analyses at the LHC need to be set larger than at the Tevatron in order, (1) to reduce the backgrounds from $W + 4$ jet production relative to the lepton + 4 jets final state from $t\bar{t}$ decay, (2) to reduce the number of jets produced by ISR in $t\bar{t}$ events, and (3) to reduce the likelihood of additional jets produced by fluctuations in the underlying event. The signal-to-background for $t\bar{t}$ is substantially improved at the LHC by increasing the minimum transverse momentum cut for each jet from 15 GeV (Tevatron) to 30 GeV (CMS) or 40 GeV (ATLAS). The cross section for the production of the lowest p_T jet in $W + 4$ jet events falls roughly as $1/p_T^n$ (where n is in the range 2.5–3) while the distribution for the 4th jet transverse momentum is essentially flat from 15 to 40 GeV. The background is reduced by a factor of 15 while the signal is reduced by a factor of 5. This reduction in signal is acceptable because of the large $t\bar{t}$ cross section available at the LHC. There are 2.5 million $t\bar{t}$ pairs produced with a lepton + jets final state for a 10fb^{-1} data sample. The requirement for two of the jets to be tagged as b-jets (and the kinematic cuts on the jets (40 GeV) and on the lepton and missing transverse momentum) reduces the event sample to 87 000, but with a signal-to-background ratio of 78. A requirement of only one b-tag reduces the signal-to-background ratio to 28 but with a data sample a factor of 3 larger.

6.6.5. Higgs boson production.   As discussed in section 2, the Higgs boson is the cornerstone of the Standard Model and its supersymmetric extensions, and its discovery will be one of the primary physics goals at the LHC. The Standard Model Higgs cross sections for various production mechanisms are shown in figure 97 (left) as a function of the Higgs mass [147]. The branching ratios of the dominant decay modes for the Standard Model Higgs boson are shown on the right side of the figure. The primary production mechanism is through gg fusion and the primary decay mode is $b\bar{b}$ (low mass) and WW (high mass).

Inclusive Higgs production through gg scattering is one of the few processes known to NNLO. The rapidity distribution for Higgs boson production at the LHC is shown in figure 98 at LO, NLO and NNLO [69]. The NLO cross section is a factor of 2 larger than the leading-order cross section and the NNLO cross section is a factor of 20% larger than the NLO one. The scale dependence at NNLO is of the order of 15%, so the cross section uncertainties are under reasonable control. As observed in figure 75, the gg parton luminosity uncertainty is less than 10% over the expected Higgs mass range.

The NLO predictions from the 41 CTEQ6.1 pdfs for the production of a 125 GeV Higgs boson through gluon fusion at the LHC are plotted versus similar predictions for the W cross section in figure 99. The low cross section point comes from error pdf 30, which is responsible for the high jet cross section predictions at high p_T; the flow of momentum to high x removes it from the kinematic region responsible for producing a Higgs boson of this mass.

Consider the rate of production (through gg fusion) of a Higgs boson in association with an additional jet at the LHC. Defining the cross section for this process to only include events with a jet of transverse momentum greater than some minimum value, $p_{T,\mathrm{min}}$, yields the dependence on $p_{T,\mathrm{min}}$ shown in figure 100. Overlaid on this figure is the cross section for
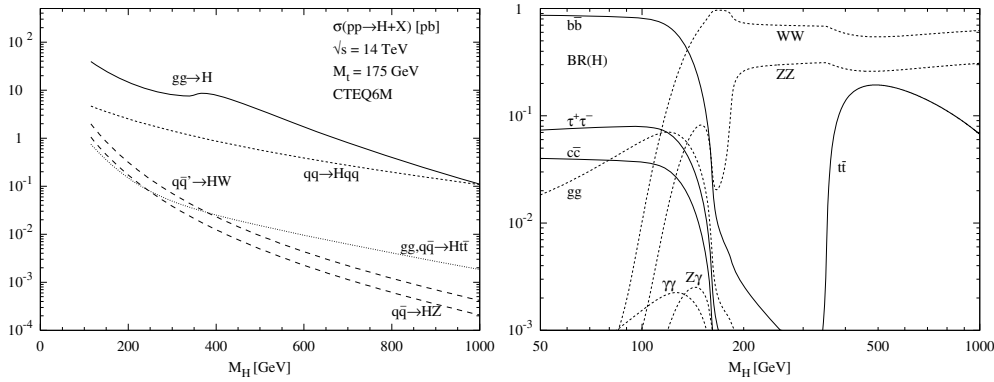
Figure 97. The production subprocess cross sections for the Standard Model Higgs at the LHC, as a function of the Higgs boson mass(left); the branching ratios for the Standard Model Higgs as a function of the Higgs boson mass(right).
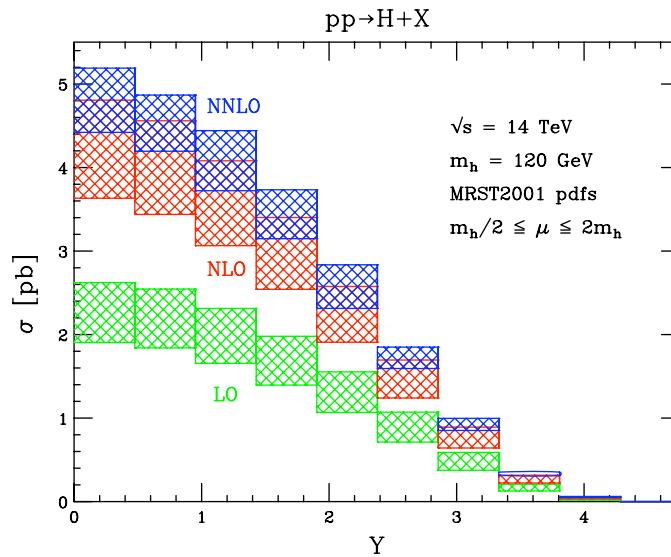

Figure 98. The rapidity distributions, at LO, NLO and NNLO, for the production of a 120 GeV mass Higgs at the LHC.

Higgs boson production at LO, NLO and NNLO. Similar to the case for $t\bar{t}$ production at the LHC, as the minimum jet transverse momentum is decreased, the cross section for Higgs + jet production increases rapidly and in fact saturates the total LO Higgs boson cross section at around 28 GeV. When the Higgs boson rate is calculated at NLO, the cross section increases and the saturation does not occur until around 15 GeV and at NNLO, the saturation occurs at around 12 GeV.

As for the case of $t\bar{t}$ production at the LHC, the combination of a gg initial-state, the high mass of the final state, and the relatively low x values of the initial-state parton results in (1) a large probability for the Higgs to be produced with extra jets and (2) for the Higgs to be produced with relatively high transverse momentum. In figure 101 (un-normalized)
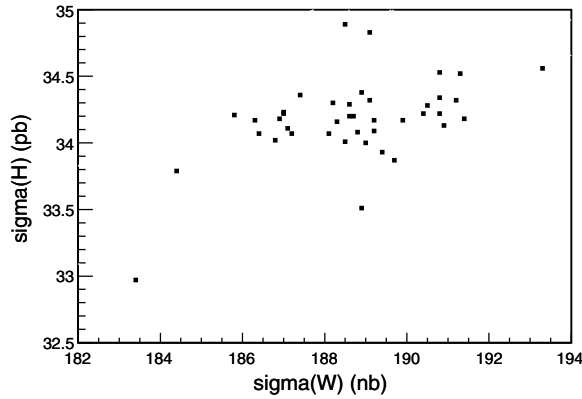
Figure 99. The cross section predictions for Higgs production versus the cross section predictions for W production at the LHC plotted using the 41 CTEQ6.1 pdfs.
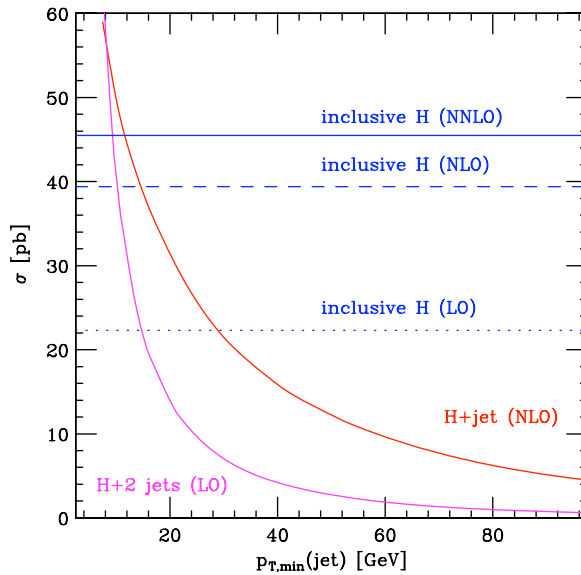
Figure 100. The dependence of the LO $t\bar{t}$+jet cross section on the jet-defining parameter $p_{T,\text{min}}$, together with the top pair production cross sections at LO and NLO.

and figure 102 (normalized) are shown a large number of predictions for the transverse momentum distributions for the production of a 125 GeV mass Higgs boson at the LHC, through the gg fusion process. The impact of higher-order corrections (both NLO and NNLO) on the normalization of the Higgs cross section is evident in figure 101. But in figure 102, it can be observed that the shapes for the p_T distributions are basically the same. In particular, parton shower Monte Carlos provide a reasonable approximation to the more rigorous predictions shown. Two PYTHIA predictions are indicated: PYTHIA 6.215 is a virtuality-ordered parton shower while PYTHIA 6.3 is a p_T-ordered shower (and as different from PYTHIA 6.215 as HERWIG is from PYTHIA). The peak of the PYTHIA 6.3 prediction is more in line with the other theoretical predictions.
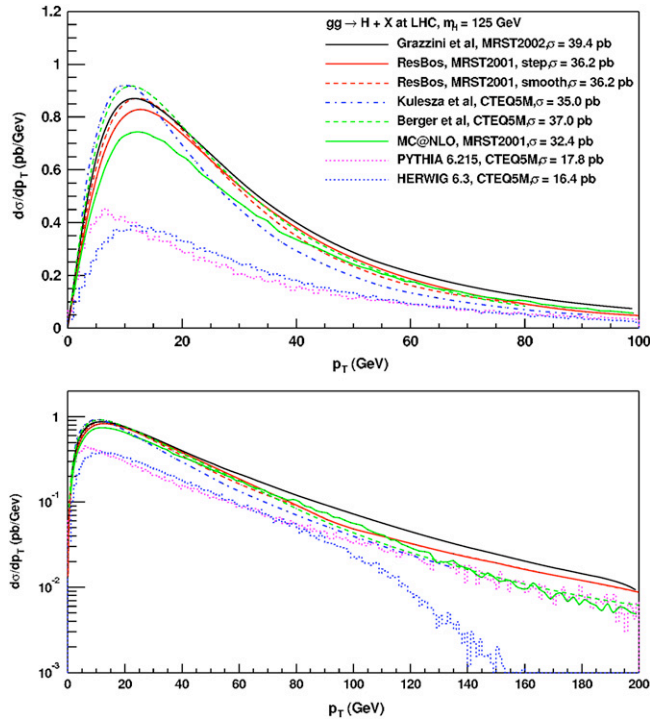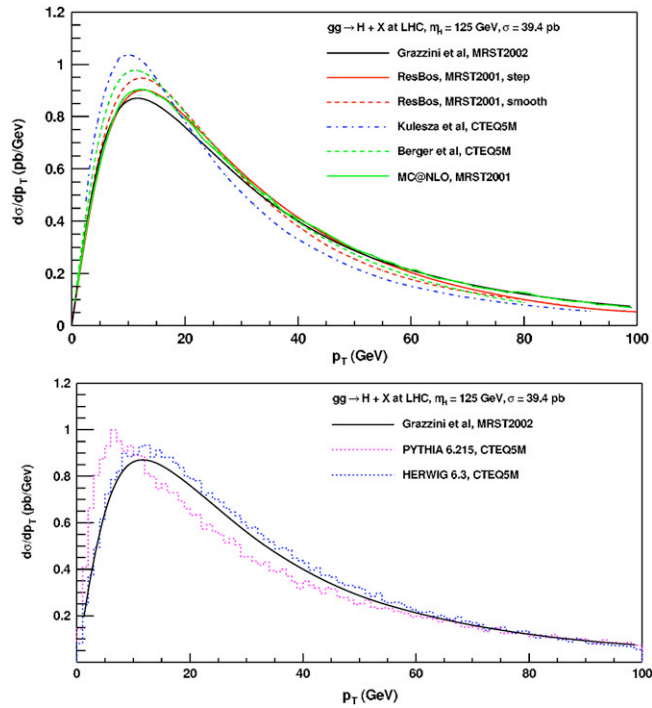
Figure 101. The predictions for the transverse momentum distribution for a 125 GeV mass Higgs boson at the LHC from a number of theoretical predictions. The predictions are shown with an absolute normalization. This figure can also be viewed in colour on the benchmark website.

Note that the p_T distribution of the Higgs boson peaks at approximately 12 GeV while the p_T distribution for the Z peaks at 3 GeV. The peak is slightly higher because of the higher mass (125 GeV compared with 90 GeV) but the major shift is due to the different production mechanisms. The colour factor for the gluon is greater than that for the quark and the phase space available for gluon radiation for $x = 0.01$ gluons is much larger due to the $z \rightarrow 0$ pole in the splitting function.

The production of a Higgs boson through the vector boson fusion (VBF) process is important, first of all, as a discovery channel and second, as a way of measuring the Higgs couplings to W and Z bosons. There are backgrounds to this process from (1) Higgs+2 jet production through gg fusion and (2) $Z + 2$ jet production, where the Z decays into τ pairs (one of the primary search modes for Higgs production from VBF) [179]. VBF production of a Higgs boson proceeds through the diagrams shown in figure 7. The emission of vector bosons from the initial-state quark lines results in the quarks acquiring a transverse momentum of the order of half of the W mass (as the weak boson mass provides a natural cutoff for the weak boson propagator) with a rapidity distribution peaked in the forward direction (the quarks still retain an appreciable fraction of their original longitudinal momentum, corresponding to x values of 0.1–0.2). The two leading jets in Higgs+2 jets (from gg fusion) are peaked at central rapidities as shown in figure 103 and have a softer jet transverse momentum. Thus, a relatively hard cut on the tagging jet transverse momenta of 40 GeV and a requirement that the tagging jets have large rapidity is effective at reducing the background without a large impact on the VBF signal. The recent calculation of the Higgs+2 jet rate at NLO [138] (one

Figure 102. The predictions for the transverse momentum distribution for a 125 GeV mass Higgs boson at the LHC from a number of theoretical predictions. The predictions have all been normalized to the same cross section for shape comparisons. This figure can also be viewed in colour on the benchmark website.

of the calculations on the wishlist) has somewhat[26] reduced the scale dependence, and thus the uncertainty, on the prediction[27]. The rate for additional jets to be produced between the two tagging jets is high for the background processes [180]. The colourless exchange in the hard scattering in VBF leads to a suppression of extra jets in the central rapidity region. Thus, as discussed earlier, a veto on extra jets in the central region is effective at decreasing the background to VBF production of the Higgs boson.

6.6.6. Inclusive jet production. The increase in the centre-of-mass energy to 14 TeV at the LHC will result in a dramatically larger accessible kinematic range. Inclusive jet cross sections can be measured out to transverse momentum values of order 4 TeV in the central region and 1.5 TeV in the forward region. The predictions with the CTEQ6.1 central pdfs and the 40 error pdfs are shown in figures 104 and 105 for three different rapidity regions [11]. The cross sections were generated with a renormalization and factorization scale equal to $p_T^{\text{jet}}/2$. The cross section predictions have a similar sensitivity to the error pdfs as do the jet cross sections at the Tevatron for similar x_T values, and the uncertainties on the predicted cross sections remain up to a factor of 2 at the highest p_T values. Measurements of the jet cross section over the full

---

[26] The reduction of the scale dependence is not dramatic since there is a large contribution from the (LO) Higgs+3 jet final state.

[27] It is interesting that the NLO corrections for Higgs+2 jets are relatively small, on the order of 20%. This follows the pattern of the NLO corrections decreasing in size as the jet multiplicity increases; the corrections are 80% for inclusive Higgs boson production (through *gg* fusion) and 50% for Higgs+1 jet.
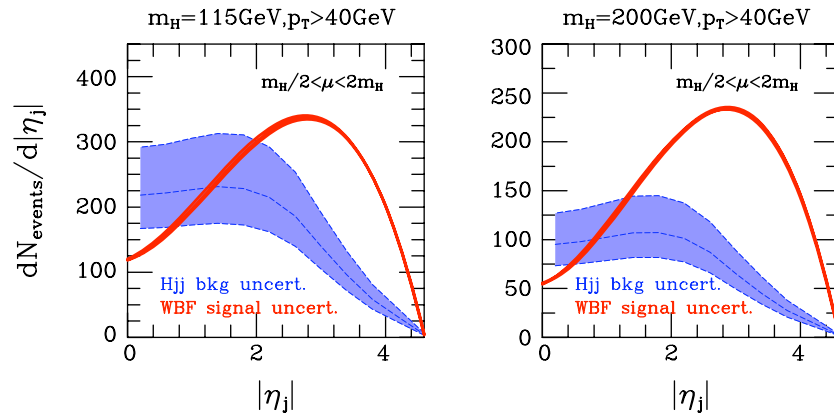
Figure 103. The tagging jet η distributions in QCD Hjj and VBF events. The band indicates the range of predictions corresponding to variation of renormalization and factorization scales by a factor of 2 about the central value of m_H.
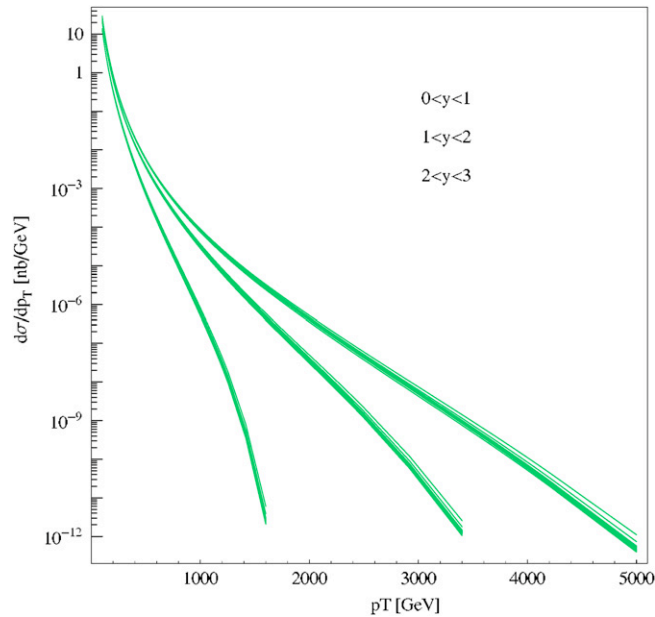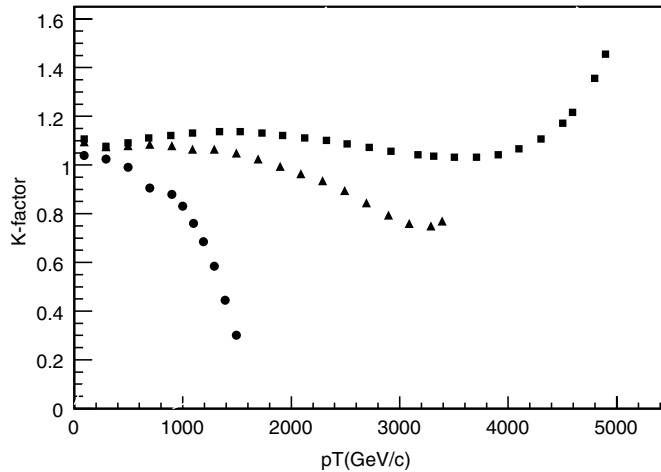

Figure 104. Inclusive jet cross section predictions for the LHC using the CTEQ6.1 central pdf and the 40 error pdfs.

rapidity range at the LHC will serve to further constrain the high x gluon pdf and distinguish between possible new physics and uncertainties in pdfs.

It is useful to plot the K-factors (the ratio of the NLO to LO cross sections) for the three different rapidity intervals shown above. As discussed previously in section 3.3.3, the value of the K-factor is a scale-dependent quantity; the K-factors shown in figure 106 are calculated with the nominal scale of $p_T^{\rm jet}/2$. The K-factors have a somewhat complicated shape due to the interplay between the different subprocesses comprising inclusive jet production and the
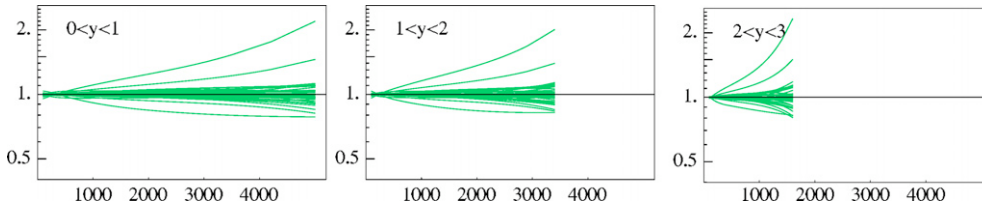
Figure 105. The ratios of the jet cross section predictions for the LHC using the CTEQ6.1 error pdfs to the prediction using the central pdf. The extremes are produced by eigenvector 15.

Figure 106. The ratios of the NLO to LO jet cross section predictions for the LHC using the CTEQ6.1 pdfs for the three different rapidity regions (0–1 (squares), 1–2 (triangles), 2–3 (circles)).

behaviours of the relevant pdfs in the different regions of parton momentum fraction x. In the central region, the K-factor is within 10% of unity for the observable range. There are no new parton–parton subprocesses that contribute at NLO but not at LO. Thus a LO prediction, using the NLO CTEQ6.1 pdfs, will reproduce fairly closely the NLO calculation. For rapidities between 1 and 2, the K-factor is within 20% of unity, dropping below one at higher transverse momentum. For forward rapidities, the K-factor drops almost immediately below one, due to the behaviour of the high-x pdfs that contribute to the cross section in this region. There is nothing wrong with the NLO prediction in this region; its relationship to the LO cross section has just changed due to the kinematics. LO predictions in this region will provide an overestimate of the NLO cross section.

We saw in section 5.3.1 that jets in the upper range of transverse momentum values at the Tevatron were very collimated. This will be even more the case at the LHC, where in the multi-TeV range, a large fraction of the jet's momentum will be contained in a single calorimeter tower. Jet events at the LHC will be much more active than events in a similar p_T range at the Tevatron. The majority of the dijet production for the transverse momentum range less than 1 TeV will be with a gg initial state. As discussed previously, the larger colour factor associated with the gluon and the greater phase space available at the LHC for gluon
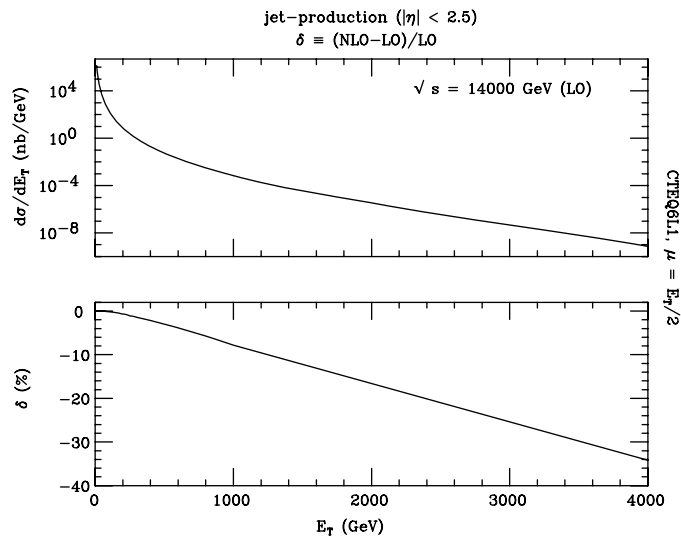
Figure 107. The effect of electroweak logarithms on jet cross sections at the LHC.

emission will result in an increased production of additional soft jets. In addition, there is an increased probability for the production of 'mini-jets' from multiple-parton scattering among the spectator partons. At full design luminosity, on the order of 25 additional minimum bias interactions will be present at each crossing. Such events, either singly or in combination, may create additional jets. As a result, the minimum jet transverse momentum requirement may need to be increased for most analyses; in addition, it may be advantageous to use smaller cone sizes than used for similar analyses at the Tevatron.

As discussed above, the LHC will produce jets at transverse momenta far larger than the W mass. Thus, virtual electroweak corrections of the form $\alpha_W \log^2(p_T^2/M_W^2)$, where $\alpha_W = \alpha_{\rm EM} \sin^2 \theta_W$, may become important. For example, at $p_T = 3 \, {\rm TeV}, \log^2(p_T^2/m_W^2) = 10$. These double logs are a result of the lack of cancellation between real and virtual W emission in higher-order calculations and may become competitive in size with NLO QCD corrections. The impact of a subset of the full EW corrections (i.e. those involving virtual electroweak boson emission only) reaches of the order of 40% at 4 TeV, as shown in figure 107 below [181, 182]. This is an indication that all Standard Model corrections, and not just those from higher-order QCD, need to be understood in order to correctly interpret any new physics that may be present at the LHC.

7. Summary

The LHC will present an unprecedented potential for the discovery of new physics. Thus, it is even more important to understand both the possible production mechanisms for the new physics and the Standard Model backgrounds for their signals. The experiences gained at the Tevatron, and the phenomenological tools developed in the last few years, will serve as a basis towards the establishment of the relevant Standard Model benchmarks at the LHC. In this paper, we have put together a primer to aid this establishment.

For convenience, we summarize below the rules-of-thumb and official recommendations discussed in our paper. First, the rules-of-thumb:

- In section 3.3.3, we present K-factors for some important processes at the Tevatron and the LHC.
- In section 3.5.1, we present some plots of Sudakov form factors useful for calculating the probability for producing jets from initial-state radiation.
- In section 6.2, we provide pdf luminosities and their uncertainties for the LHC.

  Next, our official recommendations:

- In section 4.4, we give our official recommendation for the form of the Master Equation to be used to calculate pdf uncertainties.
- In section 4.5, we recommend that NLO pdfs be used for Monte Carlo event generations.
- In section 5.3.1, we recommend that experimental cross section measurements be presented at the hadron level, and that corrections between the parton and hadron levels be clearly stated.
- In section 5.3.3, we present a revised version of the midpoint jet cone algorithm and recommend its use at the Tevatron and LHC. We also recommend the use of both cone and k_T jet algorithms for all analyses.

Acknowledgments

References

[1] Drell S D and Yan T M 1971 *Ann. Phys.* **66** 578
[2] Collins J C and Soper D E 1987 *Ann. Rev. Nucl. Part. Sci.* **37** 33
[3] Del Duca V, Kilgore W, Oleari C, Schmidt C and Zeppenfeld D 2001 *Nucl. Phys.* B **616** 367 *Preprint* hep-ph/0108030
[4] Harlander R V and Kilgore W B 2002 *Phys. Rev. Lett.* **88** 201801 *Preprint* hep-ph/0201206
[5] Anastasiou C and Melnikov K 2002 *Nucl. Phys.* B **646** 220 *Preprint* hep-ph/0207004
[6] Zeppenfeld D, Kinnunen R, Nikitenko A and Richter-Was E 2000 *Phys. Rev.* D **62** 013009 *Preprint* hep-ph/0002036
[7] Djouadi A 2005 *Preprint* hep-ph/0503172
[8] Ellis R K, Stirling W J and Webber B R 1996 *Camb. Monogr. Part. Phys. Nucl. Phys. Cosmol.* **8** 1
[9] Lipatov L N 1975 *Sov. J. Nucl. Phys.* **20** 95
    Gribov V N and Lipatov L N 1972 *Sov. J. Nucl. Phys.* **15** 438
    Altarelli G and Parisi G 1977 *Nucl. Phys.* B **126** 298
    Dokshitzer Yu L 1977 *Sov. Phys.—JETP* **46** 641
[10] Martin A D, Roberts R G, Stirling W J and Thorne R S 2004 *Phys. Lett.* B **604** 61 *Preprint* hep-ph/0410230
[11] Stump D, Huston J, Pumplin J, Tung W K, Lai H L, Kuhlmann S and Owens J F 2003 *J. High Energy Phys.* **0310** 046 *Preprint* hep-ph/0303013
[12] Acosta D *et al* (CDF II Collaboration) 2005 *Phys. Rev. Lett.* **94** 091803 *Preprint* hep-ex/0406078
[13] http://www-d0.fnal.gov/Run2Physics/WWW/results/prelim/EW/
[14] Ellis S D, Kunszt Z and Soper D E 1992 *Phys. Rev. Lett.* **69** 3615 *Preprint* hep-ph/9208249
[15] Corcella G *et al* 2001 *J. High Energy Phys.* **0101** 010 *Preprint* hep-ph/0011363
[16] Sjostrand T, Mrenna S and Skands P 2006 *J. High Energy Phys.* **0605** 026 *Preprint* hep-ph/0603175
[17] Mangano M L, Moretti M and Pittau R 2002 *Nucl. Phys.* B **632** 343 *Preprint* hep-ph/0108069
[18] Mangano M L, Moretti M, Piccinini F, Pittau R and Polosa A D 2003 *J. High Energy Phys.* **0307** 001 *Preprint* hep-ph/0206293

[19] Pukhov A *et al Preprint* hep-ph/9908288
[20] Boos E *et al* (CompHEP Collaboration) 2004 *Nucl. Instrum. Methods* A **534** 250 *Preprint* hep-ph/0403113
[21] Stelzer T and Long W F 1994 *Comput. Phys. Commun.* **81** 357 *Preprint* hep-ph/9401258
[22] Maltoni F and Stelzer T 2003 *J. High Energy Phys.* **0302** 027 *Preprint* hep-ph/0208156
[23] Caravaglios F, Mangano M L, Moretti M and Pittau R 1999 *Nucl. Phys.* B **539** 215 *Preprint* hep-ph/9807570
[24] Murayama H, Watanabe I and Hagiwara K, KEK-91-11
[25] Maltoni F, Paul K, Stelzer T and Willenbrock S 2003 *Phys. Rev.* D **67** 014026 *Preprint* hep-ph/0209271
[26] Witten E 2004 *Commun. Math. Phys.* **252** 189 *Preprint* hep-th/0312171
[27] Cachazo F, Svrcek P and Witten E 2004 *J. High Energy Phys.* **0409** 006 *Preprint* hep-th/0403047
[28] Georgiou G and Khoze V V 2004 *J. High Energy Phys.* **0405** 070 *Preprint* hep-th/0404072
[29] Wu J B and Zhu C J 2004 *J. High Energy Phys.* **0409** 063 *Preprint* hep-th/0406146
[30] Georgiou G, Glover E W N and Khoze V V 2004 *J. High Energy Phys.* **0407** 048 *Preprint* hep-th/0407027
[31] Dixon L J, Glover E W N and Khoze V V 2004 *J. High Energy Phys.* **0412** 015 *Preprint* hep-th/0411092
[32] Badger S D, Glover E W N and Khoze V V 2005 *J. High Energy Phys.* **0503** 023 *Preprint* hep-th/0412275
[33] Bern Z, Forde D, Kosower D A and Mastrolia P 2005 *Phys. Rev.* D **72** 025006 *Preprint* hep-ph/0412167
[34] Britto R, Cachazo F and Feng B 2005 *Nucl. Phys.* B **715** 499 *Preprint* hep-th/0412308
[35] Britto R, Cachazo F, Feng B and Witten E 2005 *Phys. Rev. Lett.* **94** 181602 *Preprint* hep-th/0501052
[36] Bloch F and Nordsieck A 1937 *Phys. Rev.* **52** 54
[37] Kinoshita T 1962 *J. Math. Phys.* **3** 650
[38] Lee T D and Nauenberg M 1964 *Phys. Rev.* **133** B1549
[39] Kajantie K, Lindfors J and Raitio R 1978 *Nucl. Phys.* B **144** 422
[40] Kunszt Z and Soper D E 1992 *Phys. Rev.* D **46** 192
[41] Ellis R K, Ross D A and Terrano A E 1981 *Nucl. Phys.* B **178** 421
[42] Frixione S, Kunszt Z and Signer A 1996 *Nucl. Phys.* B **467** 399 *Preprint* hep-ph/9512328
[43] Catani S and Seymour M H 1997 *Nucl. Phys.* B **485** 291
     Catani S and Seymour M H 1997 *Nucl. Phys.* B **510** 503, erratum *Preprint* hep-ph/9605323
[44] Nagy Z and Trocsanyi Z 1997 *Nucl. Phys.* B **486** 189 *Preprint* hep-ph/9610498
[45] Fabricius K, Schmitt I, Kramer G and Schierholz G 1981 *Z. Phys.* C **11** 315
[46] Giele W T and Glover E W N 1992 *Phys. Rev.* D **46** 1980
[47] Gehrmann-De Ridder A, Gehrmann T and Glover E W N 2005 *J. High Energy Phys.* **0509** 056 *Preprint* hep-ph/0505111
[48] Glover E W N and Miller D J 1997 *Phys. Lett.* B **396** 257 *Preprint* hep-ph/9609474
[49] Bern Z, Dixon L J, Kosower D A and Weinzierl S 1997 *Nucl. Phys.* B **489** 3 *Preprint* hep-ph/9610370
[50] Campbell J M, Glover E W N and Miller D J 1997 *Phys. Lett.* B **409** 503 *Preprint* hep-ph/9706297
[51] Glover E W N 2003 *Nucl. Phys. Proc. Suppl.* **116** 3 *Preprint* hep-ph/0211412
[52] Bern Z, Dixon L J and Kosower D A 1998 *Nucl. Phys.* B **513** 3 *Preprint* hep-ph/9708239
[53] Badger S D and Glover E W N 2004 *J. High Energy Phys.* **0407** 040 *Preprint* hep-ph/0405236
[54] H1 Collaboration: Adloff C *et al* 2000 *Eur. Phys. J.* C **13** 609 *Preprint* hep-ex/9908059
     H1 Collaboration: Adloff C *et al* 2001 *Eur. Phys. J.* C **19** 269 *Preprint* hep-ex/0012052
     H1 Collaboration: Adloff C *et al* 2001 *Eur. Phys. J.* C **21** 33 *Preprint* hep-ex/0012053
[55] ZEUS Collaboration: Chekanov S *et al* 2001 *Eur. Phys. J.* C **21** 443 *Preprint* hep-ex/0105090
     Cooper-Sarkar A M 2001 *Proc. Int. Europhysics Conf. on HEP* (Budapest, 2001) *Preprint* hep-ph/0110386
[56] E866 Collaboration: Towell R S *et al* 2001 *Phys. Rev.* D **64** 052002 *Preprint* hep-ex/0103030
[57] CCFR Collaboration: Yang U K *et al* 2001 *Phys. Rev. Lett.* **86** 2742 *Preprint* hep-ex/0009041
[58] BCDMS Collaboration: Benvenuti A C 1989 *et al Phys. Lett.* B **223** 485
[59] BCDMS Collaboration: Benvenuti A C 1989 *et al Phys. Lett.* B **236** 592
[60] New Muon Collaboration: Arneodo M *et al* 1997 *Nucl. Phys.* B **483** 3 *Preprint* hep-ph/9610231
     Arneodo M *et al* 1997 *Nucl. Phys.* B **487** 3 *Preprint* hep-ex/9611022
[61] CCFR Collaboration: Seligman W G *et al* 1997 *Phys. Rev. Lett.* **79** 1213 *Preprint* hep-ex/970107
[62] E605 Collaboration: Moreno G *et al* 1991 *Phys. Rev.* D **43** 2815
[63] CDF Collaboration: Affolder T *et al* 2001 *Phys. Rev.* D **64** 032001 *Preprint* hep-ph/0102074
[64] DØ Collaboration: Abbott B *et al* 2001 *Phys. Rev. Lett.* **86** 1707 *Preprint* hep-ex/0011036
     DØ Collaboration: Abbott B *et al* 2001 *Phys. Rev.* D **64** 032003 *Preprint* hep-ex/0012046
[65] Moch S, Vermaseren J A M and Vogt A 2004 *Nucl. Phys.* B **688** 101 *Preprint* hep-ph/0403192
[66] Vogt A, Moch S and Vermaseren J A M 2004 *Nucl. Phys.* B **691** 129 *Preprint* hep-ph/0404111
[67] Hamberg R, van Neerven W L and Matsuura T 1991 *Nucl. Phys.* B **359** 343
     Hamberg R, van Neerven W L and Matsuura T 2002 *Nucl. Phys.* B **644** 403 erratum
[68] Anastasiou C, Dixon L J, Melnikov K and Petriello F 2003 *Phys. Rev. Lett.* **91** 182002 *Preprint* hep-ph/0306192

[69] Anastasiou C, Melnikov K and Petriello F 2004 *Phys. Rev. Lett.* **93** 262002 *Preprint* hep-ph/0409088
[70] Sterman G 1987 *Nucl. Phys.* B **281** 310
[71] Catani S and Trentadue L 1989 *Nucl. Phys.* B **327** 323
[72] Catani S and Trentadue L 1991 *Nucl. Phys.* B **353** 183
[73] Parisi G and Petronzio R 1979 *Nucl. Phys.* B **154** 427
[74] Altarelli G, Ellis R K, Greco M and Martinelli G 1984 *Nucl. Phys.* B **246** 12
[75] Collins J C and Soper D E 1981 *Nucl. Phys.* B **193** 381
     Collins J C and Soper D E 1983 *Nucl. Phys.* B **213** 545 erratum
[76] Collins J C and Soper D E 1982 *Nucl. Phys.* B **197** 446
[77] Collins J C, Soper D E and Sterman G 1985 *Nucl. Phys.* B **250** 199
[78] Sterman G and Vogelsang W 2005 *Phys. Rev.* D **71** 014013 *Preprint* hep-ph/0409234
[79] Kulesza A, Sterman G and Vogelsang W 2004 *Phys. Rev.* D **69** 014012 *Preprint* hep-ph/0309264
[80] Kulesza A, Sterman G and Vogelsang W, *Preprint* hep-ph/0207148
[81] Balazs C and Yuan C P 1997 *Phys. Rev.* D **56** 5558 *Preprint* hep-ph/9704258
[82] Banfi A, Corcella G, Dasgupta M, Delenda Y, Salam G P and Zanderighi G *Preprint* hep-ph/0508096
[83] Gieseke S *et al Preprint* hep-ph/0609306
[84] Gleisberg T, Hoche S, Krauss F, Schalicke A, Schumann S and Winter J C 2004 *J. High Energy Phys.* **0402** 056 *Preprint* hep-ph/0311263
[85] Sjostrand T and Skands P Z 2005 *Eur. Phys. J.* C **39** 129 *Preprint* hep-ph/0408302
[86] Gieseke S 2005 *J. High Energy Phys.* **0501** 058 *Preprint* hep-ph/0412342
[87] Blazey G C *et al Preprint* hep-ex/0005012
[88] Giele W T, Glover E W N and Kosower D A 1994 *Phys. Rev. Lett.* **73** 2019 *Preprint* hep-ph/9403347
[89] Ellis S D, Huston J and Tonnesmann M 2001 *Proc. APS/DPF/DPB Summer Study on the Future of Particle Physics (Snowmass 2001)* ed N Graf, eConf **C010630** P513 *Preprint* hep-ph/0111434
[90] Boos E *et al Preprint* hep-ph/0109068
[91] Catani S, Krauss F, Kuhn R and Webber B R 2001 *J. High Energy Phys.* **0111** 063 *Preprint* hep-ph/0109231
[92] Gleisberg T, Hoeche S, Krauss F, Schaelicke A, Schumann S, Soff G and Winter J 2005 *Czech. J. Phys.* **55** B529 *Preprint* hep-ph/0409122
[93] Group T Q W *et al Preprint* hep-ph/0610012
[94] Mrenna S and Richardson P 2004 *J. High Energy Phys.* **0405** 040 *Preprint* hep-ph/0312274
[95] Chen Y J, Collins J and Zu X M 2002 *J. High Energy Phys.* **0204** 041 *Preprint* hep-ph/0110257
[96] Collins J C and Zu X 2005 *J. High Energy Phys.* **0503** 059 *Preprint* hep-ph/0411332
[97] Frixione S and Webber B R 2002 *J. High Energy Phys.* **0206** 029 *Preprint* hep-ph/0204244
[98] Frixione S, Nason P and Webber B R 2003 *J. High Energy Phys.* **0308** 007 *Preprint* hep-ph/0305252
[99] Frixione S and Webber B R *Preprint* hep-ph/0506182
[100] Kurihara Y, Fujimoto J, Ishikawa T, Kato K, Kawabata S, Munehisa T and Tanaka H 2003 *Nucl. Phys.* B **654** 301 *Preprint* hep-ph/0212216
[101] Kramer M and Soper D E 2004 *Phys. Rev.* D **69** 054019 *Preprint* hep-ph/0306222
[102] Soper D E 2004 *Phys. Rev.* D **69** 054020 *Preprint* hep-ph/0306268
[103] Kramer M, Mrenna S and Soper D E 2006 *Phys. Rev.* D **73** 014022 *Preprint* hep-ph/0509127
[104] Nagy Z and Soper D E 2005 *J. High Energy Phys.* **0510** 024 *Preprint* hep-ph/0503053
[105] Nagy Z and Soper D E 2006 *Preprint* hep-ph/0601021
[106] Frixione S, Laenen E, Motylinski P and Webber B R 2006 *J. High Energy Physics* **03** 092 *Preprint* hep-ph/0512250
[107] Alekhin S 2005 *JETP Lett.* **82** 628
      Alekhin S 2005 *Pisma Zh. Eksp. Teor. Fiz.* **82** 710 *Preprint* hep-ph/0508248
[108] Adloff C *et al* (H1 Collaboration) 2001 *Eur. Phys. J.* C **21** 33 *Preprint* hep-ex/0012053
[109] Adloff C *et al* (H1 Collaboration) 2003 *Eur. Phys. J.* C **30** 1 *Preprint* hep-ex/0304003
[110] Chekanov S *et al* (ZEUS Collaboration) 2003 *Phys. Rev.* D **67** 012007 *Preprint* hep-ex/0208023
[111] Chekanov S *et al* (ZEUS Collaboration) 2005 *Eur. Phys. J.* C **42** 1 *Preprint* hep-ph/0503274
[112] Moch S, Vermaseren J A M and Vogt A 2004 *Nucl. Phys. Proc. Suppl.* **135** 137 *Preprint* hep-ph/0408075
[113] Martin A D, Roberts R G, Stirling W J and Thorne R S 2002 *Phys. Lett.* B **531** 216 *Preprint* hep-ph/0201127
[114] Gluck M, Reya E and Vogt A 1998 *Eur. Phys. J.* C **5** 461 *Preprint* hep-ph/9806404
[115] Abe F *et al* (CDF Collaboration) 1998 *Phys. Rev. Lett.* **81** 5754 *Preprint* hep-ex/9809001
[116] Stump D *et al* 2002 *Phys. Rev.* D **65** 014012 *Preprint* hep-ph/0101051
[117] Pumplin J *et al* 2002 *Phys. Rev.* D **65** 014013 *Preprint* hep-ph/0101032
[118] Martin A D, Roberts R G, Stirling W J and Thorne R S 2003 *Eur. Phys. J.* C **28** 455 *Preprint* hep-ph/0211080

[119] Eidelman S *et al* (Particle Data Group) 2004 *Phys. Lett.* B **592** 1
[120] Pumplin J, Belyaev A, Huston J, Stump D and Tung W K 2006 *J. High Energy Phys.* **0602** 032 *Preprint* hep-ph/0512167
[121] Collins J C and Zu X m 2002 *J. High Energy Phys.* **0206** 018 *Preprint* hep-ph/0204127
[122] Plothow-Besch H 1995 *Int. J. Mod. Phys.* A **10** 2901
[123] Giele W T, Keller S A and Kosower D A 2001 *Preprint* hep-ph/0104052
[124] Giele W *et al* 2002 *Preprint* hep-ph/0204316
[125] Whalley M R, Bourilkov D and Group R C *Preprint* hep-ph/0508110
[126] Campbell J M and Ellis R K 2000 *Phys. Rev.* D **62** 114012 *Preprint* hep-ph/0006304
[127] Abulencia A *et al* (CDF Collaboration) 2006 *Phys. Rev.* D **73** 032003 *Preprint* hep-ex/0510048
[128] Alner G J *et al* (UA5 Collaboration) 1987 *Phys. Rep.* **154** 247
[129] Anastasiou C, Dixon L J, Melnikov K and Petriello F 2004 *Phys. Rev.* D **69** 094008 *Preprint* hep-ph/0312266
[130] See http://www-cdf.fnal.gov/physics/new/qcd/QCD.html
[131] Acosta D *et al* (CDF Collaboration) 2004 *Phys. Rev.* D **70** 072002 *Preprint* hep-ex/0404004
[132] Affolder A A *et al* (CDF Collaboration) 2002 *Phys. Rev.* D **65** 092002
[133] Ellis S D, Kunszt Z and Soper D E 1990 *Phys. Rev. Lett.* **64** 2121
[134] Acosta D *et al* (CDF Collaboration) 2005 *Preprint* hep-ex/0505013
[135] Abulencia A *et al* (CDF Run II Collaboration) 2005 *Preprint* hep-ex/0512020
[136] Abulencia A *et al* (CDF II Collaboration) 2006 *Phys. Rev. Lett.* **96** 122001 *Preprint* hep-ex/0512062
[137] Acosta D *et al* (CDF Collaboration) 2005 *Phys. Rev.* D **71** 052003 *Preprint* hep-ex/0410041
[138] Campbell J M, Keith Ellis R and Zanderighi G 2006 *J. High Energy Physics* **10** 028 *Preprint* hep-ph/0608194
[139] Campbell J and Huston J 2004 *Phys. Rev.* D **70** 094021
[140] Acosta D *et al* (CDF Collaboration) 2005 *Phys. Rev.* D **72** 052003 *Preprint* hep-ex/0504053
[141] http://www-cdf.fnal.gov/physics/new/top/2006/xs_ann/public.html
[142] http://www-cdf.fnal.gov/physics/new/top/2006/xs_ljetsvx/public.html
[143] http://tevewwg.fnal.gov/top/
[144] Hill C T and Simmons E H 2003 *Phys. Rep.* **381** 235
     Hill C T and Simmons E H 2004 *Phys. Rep.* **390** 553 *Preprint* hep-ph/0203079 erratum
[145] Andersen J R, Del Duca V, Maltoni F and Stirling W J 2001 *J. High Energy Phys.* **0105** 048 *Preprint* hep-ph/0105146
[146] Andersen J R 2006 *Phys. Lett.* B **639** 290 *Preprint* hep-ph/0602182
[147] http://cms.cern.ch/iCMS/
[148] http://atlas.web.cern.ch/Atlas/GROUPS/PHYSICS/TDR/access.html
[149] Buttar C *et al* 2006 *Preprint* hep-ph/0604120
[150] Pukhov A 2004 *Preprint* hep-ph/0412191
[151] Alekhin S *Preprint* hep-ph/0311184
     Alekhin S 2003 *Phys. Rev.* D **68** 014002 *Preprint* hep-ph/0211096
[152] Martin A D, Roberts R G, Stirling W J and Thorne R S 2004 *Eur. Phys. J.* C **35** 325 *Preprint* hep-ph/0308087
[153] Martin A D, Roberts R G, Stirling W J and Thorne R S 2002 *Phys. Lett.* B **531** 216 *Preprint* hep-ph/0201127
[154] Huston J, Pumplin J, Stump D and Tung W K 2005 *J. High Energy Phys.* **0506** 080 *Preprint* hep-ph/0502080
[155] Bern Z, Dixon L J and Kosower D A 1996 *Ann. Rev. Nucl. Part. Sci.* **46** 109 *Preprint* hep-ph/9602280
[156] Cachazo F, Svrcek P and Witten E 2004 *J. High Energy Phys.* **0410** 074 *Preprint* hep-th/0406177
[157] Brandhuber A, Spence B J and Travaglini G 2005 *Nucl. Phys.* B **706** 150 *Preprint* hep-th/0407214
[158] Brandhuber A, McNamara S, Spence B J and Travaglini G 2005 *J. High Energy Phys.* **0510** 011 *Preprint* hep-th/0506068
[159] Bern Z, Dixon L J and Kosower D A 2005 *Phys. Rev.* D **71** 105013 *Preprint* hep-th/0501240
[160] Forde D and Kosower D A 2006 *Phys. Rev.* D **73** 061701 *Preprint* hep-ph/0509358
[161] Ferroglia A, Passera M, Passarino G and Uccirati S 2003 *Nucl. Phys.* B **650** 162 *Preprint* hep-ph/0209219
[162] Anastasiou C and Daleo A 2006 *J. High Energy Physics* **10** 031 *Preprint* hep-ph/0511176
[163] Giele W T and Glover E W N 2004 *J. High Energy Phys.* **0404** 029 *Preprint* hep-ph/0402152
[164] Giele W, Glover E W N and Zanderighi G 2004 *Nucl. Phys. Proc. Suppl.* **135** 275 *Preprint* hep-ph/0407016
[165] F. del Aguila and Pittau R 2004 *J. High Energy Phys.* **0407** 017 *Preprint* hep-ph/0404120
[166] A. van Hameren, Vollinga J and Weinzierl S 2005 *Eur. Phys. J.* C **41** 361 *Preprint* hep-ph/0502165
[167] Binoth T, Guillet J P, Heinrich G, Pilon E and Schubert C 2005 *J. High Energy Phys.* **0510** 015 *Preprint* hep-ph/0504267
[168] Ellis R K, Giele W T and Zanderighi G, *Preprint* hep-ph/0508308
[169] Ellis R K, Giele W T and Zanderighi G 2005 *Phys. Rev.* D **72** 054018 *Preprint* hep-ph/0506196
[170] Flanagan G U, FERMILAB-THESIS-2005-58

[171] Balazs C, Huston J and Puljak I 2001 *Phys. Rev. D* **63** 014021 *Preprint* hep-ph/0002032
[172] Collins J C, Soper D E and Sterman G 1986 *Nucl. Phys. B* **263** 37
[173] Berge S, Nadolsky P, Olness F and Yuan C P 2005 *Phys. Rev. D* **72** 033015 *Preprint* hep-ph/0410375
[174] Fadin V S, Kuraev E A and Lipatov L N 1975 *Phys. Lett.* B **60** 50
[175] Kuraev E A, Lipatov L N and Fadin V S 1976 *Sov. Phys. JETP* **44** 443
       Kuraev E A, Lipatov L N and Fadin V S 1976 *Zh. Eksp. Teor. Fiz.* **71** 840
[176] Kuraev E A, Lipatov L N and Fadin V S 1977 *Sov. Phys. JETP* **45** 199
       Kuraev E A, Lipatov L N and Fadin V S 1977 *Zh. Eksp. Teor. Fiz.* **72** 377
[177] Balitsky I I and Lipatov L N 1978 *Sov. J. Nucl. Phys.* **28** 822
       Balitsky I I and Lipatov L N 1978 *Yad. Fiz.* **28** 1597
[178] Berge S, Nadolsky P M, Olness F I and Yuan C P 2005 *AIP Conf. Proc.* **792** 722 *Preprint* hep-ph/0508215
[179] Berger E L and Campbell J 2004 *Phys. Rev. D* **70** 073011 *Preprint* hep-ph/0403194
[180] Del V Duca, Frizzo A and Maltoni F 2004 *J. High Energy Phys.* **0405** 064 *Preprint* hep-ph/0404013
[181] Moretti S, Nolten M R and Ross D A *Preprint* hep-ph/0503152
[182] Baur U 2006 *Preprint* hep-ph/0611241